Multi-physical Characterization of Micro- and Nanomaterials

by

Juntian Qu

Department of Mechanical Engineering
McGill University

Montreal, Quebec, Canada

April 2019

A thesis submitted to McGill University in partial fulfillment of the requirements for a doctoral degree

DEDICATION

To my parents who gave me life, my wife and my newborn princess.

TABLE OF CONTENTS

LIST OF FIGURES

LIST OF TABLES

ABSTRACT

Functional micro- and nanomaterials possess exceptional mechanical, electrical and optical properties compared with their bulk counterparts, and these multi-physical properties have significantly benefited their diverse applications to a variety of scientific and engineering problems. The multi-physical properties of these micro- and nanomaterials need to be characterized accurately and efficiently to facilitate both material synthesis and device application.

Among various experimental tools for micro- and nanomaterial characterization, micro-electro-mechanical systems (MEMS) were often employed for mechanical characterization due to its advantages such as high sensing resolution, small footprint, and precise sample alignment. However, most of them are limited to one-axis actuation or sensing and thus can only be applied to perform single-axis compression or tensile testing. Besides, for nanomaterial characterization, the emerging technique of nanomanipulation under scanning electron microscopy (SEM) has enabled various multi-physical characterization experiments of nanomaterials such as electrical and mechanical measurements, thanks to its merits such as high positioning and imaging resolution and well-controlled stable testing conditions. However, the existence of contact resistance during SEM *in-situ* electrical nanoprobing could affect the measurement accuracy; therefore, it is highly desired to minimize the contact resistance during electrical characterization of nanomaterials.

Moreover, multi-physical properties of nanomaterials not only exist in their independent states, but also often coupled with each other and closed correlated. For instance, the coupling optoelectronic characterization of nanostructures is becoming more and more popular with the rapid advance of optoelectronic nanodevices. However, SEM was not often utilized for optical or optoelectronic characterization of nanomaterials, which is attributed to the challenge of integrating optical components inside a limited-space SEM chamber, as well as the limited light collection

efficiency. Therefore, it is a clear demand for the development of a SEM-based *in-situ* nanomanipulation system capable of characterizing the mechanical, electrical, optical, and multi-field-coupled properties of nanomaterials.

In this thesis, in order to solve abovementioned challenge for mechanical characterization of micromaterials, a MEMS microgripper was developed to achieve, for the first time, microscale elastic and viscoelastic characterization of soft materials in both compressive and shear directions. A systematic investigation of the contact resistance in SEM *in-situ* electrical characterization of nanomaterials was carried out employing the two-point *in-situ* nanoprobing technique, and experimental strategies have been identified to minimize the sample-probe contact resistance. The optimized SEM *in-situ* electrical nanoprobing system was subsequently applied to electrical characterization of single n-i-n-n^+ GaN nanowires (NWs), which revealed superior electrical breakdown properties of the GaN NWs. Finally, by integrating techniques for mechanical, electrical and optical characterization of nanomaterials, the first SEM-based nanomanipulation system for *in-situ* multi-physical characterization of nanomateirals was developed, which allows *in-situ* comprehensive opto-electro-mechanical characterization of individual nanostructures with high accuracy and efficiency. Using this system, the effect of mechanical stress/strain on the optoelectronic properties of single InGaN/GaN NWs was systematically investigated for the first time, providing valuable experimental data for better understanding the material's complex coupling-field properties with significant implication in group III nitride NW-based nanoelectronics and optoelectronics. The developed characterization system will greatly facilitate the experimental investigation of multi-field-coupled properties of semiconductor nanomaterials and nanostructures.

RÉSUMÉ

Les micro- et nanomatériaux fonctionnels possèdent des propriétés mécaniques, électriques et optiques exceptionnelles par rapport à leurs homologues volumineux. Ces propriétés multi-physiques ont largement profité à leurs diverses applications pour résoudre divers problèmes scientifiques et techniques. Les propriétés multi-physiques de ces micro- et nanomatériaux doivent tre caractérisées avec précision et efficacité afin de faciliter la synthèse du matériau et l'application de lappareil.

Parmi divers outils expérimentaux de caractérisation des micro- et nanomatériaux, les systémes micro-électro-mécaniques (MEMS) ont souvent été utilisés pour la caractérisation mécanique en raison de ses avantages tels que la haute résolution de détection, le faible encombrement et l'alignement précis des échantillons. Cependant, la plupart d'entre eux sont limités á l'activation ou á la détection sur un axe et ne peuvent donc tre appliqués que pour effectuer des tests de compression ou de traction sur un axe. En outre, pour la caractérisation des nanomatériaux, la technique émergente de la nano-manipulation en microscopie électronique á balayage (MEB) a permis diverses expériences de caractérisation multi-physique de nanomatériaux, telles que des mesures électriques et mécaniques, bénéficiant de ses avantages tels que conditions de test stables controlées. Cependant, l'existence d'une résistance de contact pendant le nano-sondage électrique in situ au MEB pourrait affecter la précision de la mesure; par conséquent, il est hautement souhaitable de minimiser la résistance de contact lors de la caractérisation électrique des nanomatériaux.

De plus, les propriétés multi-physiques des nanomatériaux existent non seulement dans leurs états indépendants, mais aussi souvent couplées les unes aux autres et en corrélation fermée. Par exemple, le couplage des caractérisations optoélectroniques de nanostructures est de plus en plus populaire avec le progrès rapide des nanodispositifs optoélectroniques. Cependant, la MEB n'a pas été souvent utilisé pour la caractérisation optique ou optoélectronique des nanomatériaux, ce

qui est attribué au défi consistant à intégrer des composants optiques à l'intérieur d'une chambre MEB avec espace limité, ainsi qu'à l'efficacité de la collecte de lumière limitée. Par conséquent, il est hautement souhaitable de développer un système de nano-manipulation in situ à base de la MEB capable de caractériser les propriétés mécaniques, électriques, optiques et couplées à plusieurs champs des nanomatériaux.

Dans cette thèse, afin de résoudre le problème susmentionné de la caractérisation mécanique des micromatériaux, une micro-pince MEMS a été développé pour réaliser pour la première fois la caractérisation élastique et viscoélastique à l'échelle microscopique de matériaux mous dans des directions de compression et de cisaillement. Une étude systématique du problème de la résistance au contact dans la caractérisation électrique in situ au MEB de nanomatériaux a été réalisée à l'aide d'une technique de nano-sondage *in-situ* en deux points et a permis une amélioration très poussée de la résistance au contact. Le système optimisé de nanoprocesseurs électriques *in-situ* SEM a ensuite été appliqué à une caractérisation électrique de nanofils n-i-n-n^+ GaN simples (NF) et des propriétés de rupture électriques supérieures ont été obtenues. Enfin, en intégrant différents types deffecteurs mécaniques, électriques et optiques, le premier système de nanomanipulation à base de SEM pour la caractérisation multi-physique in-situ de nanomatériaux a été développé, ce qui permet une caractérisation opto-électro-mécanique complète in situ nanostructures indépendamment ou simultanément. De plus, pour la première fois, les effets mécaniques (contraintes / contraintes) sur les propriétés optoélectroniques de réacteurs NF simples InGaN / GaN ont été systématiquement étudiés, afin de mieux comprendre et doptimiser le processus de conditionnement des DEL blanches InGaN / GaN NF. Le système de caractérisation multi-physique développé facilitera grandement la mise en évidence des propriétés de champ de couplage sous-jacentes complexes de nanomatériaux et nanostructures uniques, pour des applications potentielles de prototypes de construction et de sélection de nanostructures appropriées pour la construction de dispositifs optoélectroniques.

ACKNOWLEDGEMENT

I would not be able to complete my thesis without the help from a group of people including Professors, staff, colleagues, friends and my family. First, I would like to thank my supervisor Professor Xinyu Liu who lead me into the gate of research, guided me tirelessly, showed me how to be a professional researcher and moreover, encouraged me getting through the tough times. His enthusiasm for research and high standard for research quality set the bar for me and will be my example in future. I truly appreciate for his offer to let me pursue my doctoral degree at McGill University.

I appreciate the financial supports from the Faculty of Engineering at McGill University and Fonds de recherche Nature et technologies of Quebec Province.

I would like to express my great appreciation to my colleagues in Biomedical Microsystem Laboratory and other friends who are always ready to help: Longyan Chen, Xiao Li, Weize Zhang, Pengfei Song, Xianke Dong, Chen Zhao, Qiyang Wu, Binbin Ying, Hao Fu, Peng Pan, Sina Kheiri, Zhen Qin, Yueyue Pan, Linghao Du, Yu-Hsuan Wang, Tyler Clancy and Dylan Caverly.

Last but not least, I owe the deepest thanks to my father Haibo Qu, my mother Yiying Guo and my wife Jiyun Zhang. They stand with me and support me through the difficult times.

CONTRIBUTION OF AUTHORS

This is a manuscript-based thesis consisting of five journal articles that have been published, or completed for submission. The titles of the articles, names of the authors, and their contributions are listed below.

- **Multi-physical Characterization of Micro and Nanomaterials: A Review**

  Juntian Qu and Xinyu Liu

  Juntian Qu is with the Department of Mechanical Engineering, McGill University, Montreal, Quebec H3A 0C3, Canada.

  Xinyu Liu and Juntian Qu are with the Department of Mechanical Industrial Engineering, University of Toronto, Toronto, ON M5S 3G8, Canada.

  To be submitted.

  Author contributions:

  Juntian Qu organized the literature information, collected the presentation items, and wrote the manuscript.

  Xinyu Liu supervised the project and wrote the manuscript.

- **Microscale Compression and Shear Testing of Soft Materials Using A MEMS Microgripper with Two-Axis Actuators and Force Sensors**

  Juntian Qu, Weize Zhang, Andrew Jung, Simon Silva-Da Cruz, and Xinyu Liu

  The authors are with the Department of Mechanical Engineering, McGill University, Montreal, Quebec H3A 0C3, Canada.

  Published on: IEEE Transactions on Automation Science and Engineering, vol. 14, no. 2, pp. 834–843, 2016. DOI 10.1109/TASE.2016.2613684.

  Author contributions:

Juntian Qu designed and conducted the experiments, collected and analyzed the data, and wrote the manuscript. Weize Zhang designed and conducted the experiments. Juntian Qu and Weize Zhang contributed equally to the work. Andrew Jung prepared the samples, Simon Silva-Da Cruz developed the force sensing algorithm.

Xinyu Liu supervised the project, designed the experiments, analyzed the data, and wrote the manuscript.

- **Investigating the Impact of SEM Chamber Conditions and Imaging Parameters on the Contact Resistance of *In-Situ* Nanoprobing**

  Juntian Qu, Martin Lee, Michael Hilke and Xinyu Liu

  Juntian Qu and Xinyu Liu are with the Department of Mechanical Engineering, McGill University, Montreal, Quebec H3A 0C3, Canada.

  Martin Lee and Michael Hilke are with the Department of Physics, McGill University, Montreal, Quebec H3A 0C3, Canada

  Published on: Nanotechnology, vol. 28, no. 34, 345702 (11pp), 2017. DOI 10.1088/1361-6528/aa79ea.

  Author contributions:

  Juntian Qu designed and conducted the experiments, collected and analyzed the data, and wrote the manuscript. Martin Lee and Michael Hilke participated in sample fabrication.

  Xinyu Liu supervised the project, designed the experiments, analyzed the data, and wrote the manuscript.

- **Characterizing the Electrical Breakdown Properties of Single n-i-n-n$^+$:GaN Nanowires**

  Juntian Qu, Renjie Wang, Yu Sun, Ishiang Shih, Zetian Mi and Xinyu Liu

  Juntian Qu and Xinyu Liu are with the Department of Mechanical Engineering, McGill University, Montreal, Quebec H3A 0C3, Canada.

  Juntian Qu, Yu Sun and Xinyu Liu are with the Department of Mechanical and Industrial Engineering, University of Toronto, Toronto, Ontario, Canada, M5S 3G8.

Renjie Wang and Ishiang Shih are with the Department of Electrical and Computer Engineering, McGill University, Montreal, Quebec, Canada, H3A 0E9.

Zetian Mi is with the Department of Electrical Engineering and Computer Science, University of Michigan, Ann Arbor, MI, United States, 48109.

Published on: Applied Physics Letters (APL), vol. 113, no. 19, 193103, 2018. DOI 10.1063/1.5050511.

Author contributions:

Juntian Qu designed and conducted the experiments, collected and analyzed the data, and wrote the manuscript. Renjie Wang, Ishiang Shih and Zetian Mi synthesized the sample, and analyzed the data. Juntian Qu and Renjie Wang contributed equally to the work. Yu Sun provided the SEM and revised the manuscript.

Xinyu Liu supervised the project, designed the experiments, analyzed the data, and wrote the manuscript.

- **Multi-physical Characterization of Single InGaN/GaN NWs in SEM**

  Juntian Qu, Renjie Wang, Peng Pan, Yu Sun, Ishiang Shih, Zetian Mi and Xinyu Liu

  Juntian Qu, Peng Pan and Xinyu Liu are with the Department of Mechanical Engineering, McGill University, Montreal, Quebec H3A 0C3, Canada.

  Juntian Qu, Peng Pan, Yu Sun and Xinyu Liu are with the Department of Mechanical and Industrial Engineering, University of Toronto, Toronto, Ontario, Canada, M5S 3G8.

  Renjie Wang and Ishiang Shih are with the Department of Electrical and Computer Engineering, McGill University, Montreal, Quebec, Canada, H3A 0E9.

  Zetian Mi is with the Department of Electrical Engineering and Computer Science, University of Michigan, Ann Arbor, MI, United States, 48109.

  To be submitted.

  Author contributions:

  Juntian Qu designed and conducted the experiments, collected and analyzed the data, and wrote the manuscript. Renjie Wang, Ishiang Shih and Zetian Mi synthesized the sample and

analyzed the data. Peng Pan assisted in the optical fiber holder design. Yu Sun provided the SEM and revised the manuscript.

Xinyu Liu supervised the project, designed the experiments, analyzed the data, and wrote the manuscript.

CHAPTER 1
Introduction

1.1 Multi-physical Characterization of Micro- and Nanomaterials

The last two decades have witnessed extensive research on micro- and nanomaterials due to their exceptional promise in science and technology. Thanks to their superior physical/chemical properties and unique morphologies, functional micro- and nanomaterials possess exceptional mechanical, electrical and optical properties compared with their bulk counterparts, and these multi-physical properties have significantly benefited their diverse applications to a variety of scientific and engineering problems, such as next-generation electronics [1], sustainable energy [2], and biosensing [3]. For the experimental determination of these multi-physical properties, multi-physical characterization is thus of major concern from the perspective of both nanomaterial synthesis and device applications.

There are various traditional experimental tools and techniques for mechanical characterization of micromaterials , such as micropipette aspiration [4, 5], atomic force microscopy [6], microindentation/nanoindentation [7, 8], and magnetic bead measurement [9]. However, these techniques are limited to quantification of only local mechanical properties of a material. Compared with the aforementioned techniques, microelectromechanical systems (MEMS)-based methods possess many advantages, such as high sensing resolution, small footprint, and excellent cost-effectiveness [10]. A variety of MEMS-based platforms [11, 12, 13, 14, 15, 16] have been developed for mechanical testing of different types of materials at the microscale. Despite the effectiveness of these MEMS platforms, most of them are limited to one-axis actuation or sensing and thus can only be applied to perform single-axis compression or tensile testing.

In the aspect of nanomaterial characterization, the emerging technique of nanomanipulation under scanning electron microscopy (SEM) has enabled various multi-physical characterization experiments of nanomaterials such as electrical and mechanical measurements [17, 18], which benefit from its merits such as high positioning [19] and imaging resolution [17], along with well-controlled stable testing conditions. Among various electrical characterization methods in SEM, the *in-situ* electrical nanoprobing technique is usually preferred by certain type of study that requires accurate electrical characterization of as-grown, unaltered nanomaterials [20]. This method

uses conductive nanoprobes with nanometer-sized tips to directly probe a sample and establish electrical contacts [21]. However, the contact resistance between the nanoprobe and sample has been a challenging issue and could significantly affect the measured data. Therefore, it is highly desired to minimize the contact resistance during *in-situ* electrical nanoprobing characterization of nanomaterials.

Moreover, except for single-field mechanical or electrical characterization, the multi-physical properties of functional nanomaterials not only exist in independent states, but also often coupled with each other and closed correlated (e.g., piezoelectric and optoelectronic properties). With the rapid advance of optical and optoelectronic nanodevices, the optical and optoelectronic characterization of nanostructures is becoming more and more popular, for the purpose of both device's performance improvement and revealing complicated underlying coupling-field properties. For instance, III-nitride NWs (e.g., InN, GaN, AlN) have been pivotal for optoelectronic applications such as ultrahigh-speed nanoscale lasers [22], photodetectors [23], and high-efficiency white light-emitting diodes (LEDs) [24]. These applications usually require accurate optoelectronic characterization of the III-nitride NWs. However, as an important characterization technique, nanomaterial characterization involving optical property measurements in SEM has not been studies extensively. For single-field optical characterization, only a few cathodoluminescence (CL) characterization [25, 26, 27, 28] were carried out in SEM. While for coupling-field optoelectronic characterization, SEM was only utilized for focused ion beam (FIB)-assisted metal contacts deposition [29], the major characterization processes were all performed in ambient environment. The lack of SEM-based optical characterization is mainly attributed to the limited space of SEM chamber, which leads to the challenge of integrating optical components such as sizeable paraboloidal mirror for effective light collection [30].

Therefore, based on above discussions, it is highly desired to develop an SEM-based *in-situ* multi-physical characterization system capable of characterizing the mechanical, electrical, optical, and multi-field-coupled properties of nanomaterials.

1.2 Thesis Objective

The overall objective of my Ph.D. research is to develop the first SEM-based nanomanipulation system for opto-electro-mechanical characterization of nanomaterials. In the meanwhile, I also aim at solving the one-axis actuation/sensing limitation in MEMS-based mechanical characterization of micromaterials. The detailed objectives are listed as follows:

1. To develop a MEMS-based microgripper that integrates two-axis actuators and force sensors, for microscale elastic and viscoelastic characterization of soft materials in both compressive and shear directions.
2. To carry out a systematic investigation of the probe-sample contact resistance in SEM-based *in-situ* electrical characterization of nanomaterials, aiming at minimizing the contact resistance level during SEM-based *in-situ* nanoprobing.
3. To apply the optimized SEM-based *in-situ* electrical nanoprobing system to electrical characterization of single n-i-n-n^+ GaN nanowires (NWs) and obtain superior electrical breakdown properties.
4. To develop the first SEM-based nanomanipulation system for *in-situ* multi-physical characterization of nanomateirals, which allows *in-situ* comprehensive opto-electro-mechanical characterization of individual nanostructures.
5. To perform the first demonstration of opto-electro-mechanical characterization of single InGaN/GaN NWs and investigate the effect of mechanical stress/strain on the optoelectronic properties of single InGaN/GaN NWs.

1.3 Thesis Organization

This thesis is organized as follow:

Chapter 1 describes the objective of this research. Chapter 2 reviews the current research and common issues of SEM-based multi-physical characterization of nanomateirals. Chapter 3 describes the development of the first MEMS-based microgripper that integrates two-axis actuators and force sensors for elastic and viscoelastic characterization in both compressive and shear directions. Chapter 4 presents the experimental investigation of probe-sample contact resistance in SEM-based

in-situ electrical characterization of nanomaterials. Chapter 5 reports the systematic electrical characterization of novel single n-i-n-n^+ GaN nanowires (NWs) to quantify its superior electrical breakdown properties. Chapter 6 presents the the first SEM-based nanomanipulation system for *in-situ* multi-physical characterization of nanomateirals, and demonstrates, for the first time, effect of mechanical strain/stress on the optoelectronic properties of single InGaN/GaN NWs. Chapter 7 provides the thesis conclusion and future work.

References

[1] S. Choi, H. Lee, R. Ghaffari, T. Hyeon, and D.-H. Kim, "Recent advances in flexible and stretchable bio-electronic devices integrated with nanomaterials," *Advanced Materials*, vol. 28, no. 22, pp. 4203–4218, 2016.

[2] M. Casini, *Smart buildings: Advanced materials and nanotechnology to improve energy-efficiency and environmental performance*. Woodhead Publishing, 2016.

[3] M. You, Z. Li, P. Zhang, D. Bai, M. Lin, and F. Xu, "Nanomaterial- and micromaterial-based immunoassays," in *Handbook of Immunoassay Technologies*, S. K. Vashist and J. H. Luong, Eds., Academic Press, 2018, pp. 273 –304.

[4] R. M. Hochmuth, "Micropipette aspiration of living cells," *J. Biomech.*, vol. 33, pp. 15–22, 2000.

[5] X. Liu, Y. Wang, and Y. Sun, "Cell contour tracking and data synchronization for real-time, high-accuracy micropipette aspiration," *IEEE Trans. Autom. Sci. Eng.*, vol. 6, no. 3, pp. 536–543, 2009.

[6] R. Roy, W. Chen, L. Cong, L. A. Goodell, D. J. Foran, and J. P. Desai, "A semi-automated positioning system for contact-mode atomic force microscopy (afm)," *IEEE Trans. Autom. Sci. Eng.*, vol. 10, no. 2, pp. 462–465, 2013.

[7] J. Tan, Y. J. Chao, X. Li, and J. W. Van Zee, "Microindentation test for assessing the mechanical properties of silicone rubber exposed to a simulated polymer electrolyte membrane fuel cell environment," *J. Fuel Cell Sci. Tech.*, vol. 6, p. 041 017, 2009.

[8] Y. Zhang and C. Pan, "Measurements of mechanical properties and number of layers of graphene from nano-indentation," *Diamond Relat. Mater.*, vol. 24, pp. 1–5, 2012.

[9] R Bausch, W Möller, and E Sackmann, "Measurement of local viscoelasticity and forces in living cells by magnetic tweezers," *Biophys. J.*, vol. 76, pp. 573–579, 1999.

[10] K. Kim, J. Cheng, Q. Liu, X. Y. Wu, and Y. Sun, "Investigation of mechanical properties of soft hydrogel microcapsules in relation to protein delivery using a mems force sensor," *J. Biomed. Mater. Res., Part A*, vol. 92, no. 1, pp. 103–113, 2010.

[11] X. Liu, R. Fernandes, A. Jurisicova, R. F. Casper, and Y. Sun, "In situ mechanical characterization of mouse oocytes using a cell holding device," *Lab. Chip*, vol. 10, no. 16, pp. 2154–2161, 2010.

[12] M. Gnerlich, S. F. Perry, and S. Tatic-Lucic, "A submersible piezoresistive mems lateral force sensor for a diagnostic biomechanics platform," *Sensor. Actuat. A-Phys.*, vol. 188, pp. 111–119, 2012.

[13] X. Liu, J. Shi, Z. Zong, K.-T. Wan, and Y. Sun, "Elastic and viscoelastic characterization of mouse oocytes using micropipette indentation," *Ann. Biomed. Eng.*, vol. 40, no. 10, pp. 2122–2130, 2012.

[14] K. Kim, X. Liu, Y. Zhang, J. Cheng, X. Y. Wu, and Y. Sun, "Elastic and viscoelastic characterization of microcapsules for drug delivery using a force-feedback mems microgripper," *Biomed. Microdevices*, vol. 11, no. 2, pp. 421–427, 2009.

[15] K Kim, X Liu, Y Zhang, and Y Sun, "Nanonewton force-controlled manipulation of biological cells using a monolithic MEMS microgripper with two-axis force feedback," *J. Micromech. Microeng.*, vol. 18, p. 055 013, 2008.

[16] Q. Xu, "Design, Fabrication, and Testing of an MEMS Microgripper With Dual-Axis Force Sensor," *IEEE Sensors Journal*, vol. 15, no. 10, pp. 6017–6026, 2015.

[17] C. Shi, D. K. Luu, Q. Yang, J. Liu, J. Chen, C. Ru, S. Xie, J. Luo, J. Ge, and Y. Sun, "Recent advances in nanorobotic manipulation inside scanning electron microscopes," *Microsystems & Nanoengineering*, vol. 2, no. February, p. 16 024, 2016.

[18] X. L. Wei, Q. Chen, L. M. Peng, R. Cui, and Y. Li, "In situ measurements on individual thin carbon nanotubes using nanomanipulators inside a scanning electron microscope," *Ultramicroscopy*, vol. 110, no. 3, pp. 182–189, 2010.

[19] T. Fukuda, M. Nakajima, P. Liu, and M. R. Ahmad, "Bringing the Nanolaboratory Inside Electron Microscopes," *IEEE Nanotechnology Magazine*, vol. 2, no. 2, pp. 18–31, 2008.

[20] A. S. Walton, C. S. Allen, K Critchley, M. L. Gorzny, J. E. M. c Kendry, R. M. D. Brydson, B. J. Hickey, and S. D. Evans, "Four-probe electrical transport measurements on individual metallic nanowires," *Nanotechnology*, vol. 18, no. 6, p. 065 204, 2007.

[21] A. Bietsch, M. A. Schneider, M. E. Welland, and B. Michel, "Electrical testing of gold nanostructures by conducting atomic force microscopy," *J. Vac. Sci. Technol., B*, vol. 18, no. 3, pp. 1160–1170, 2000.

[22] N. N. Ledentsov, D. Bimberg, and Z. I. Alferov, "Progress in epitaxial growth and performance of quantum dot and quantum wire lasers," *J. Lightwave Technol.*, vol. 26, no. 11, pp. 1540–1555, 2008.

[23] A. D. L. Bugallo, L. Rigutti, G. Jacopin, F. H. Julien, C. Durand, X. J. Chen, D. Salomon, J. Eymery, and M. Tchernycheva, "Single-wire photodetectors based on ingan/gan radial quantum wells in gan wires grown by catalyst-free metal-organic vapor phase epitaxy," *Applied Physics Letters*, vol. 98, no. 23, p. 233 107, 2011.

[24] W. Guo, M. Zhang, A. Banerjee, and P. Bhattacharya, "Catalyst-free ingan/gan nanowire light emitting diodes grown on (001) silicon by molecular beam epitaxy," *Nano Letters*, vol. 10, no. 9, pp. 3355–3359, 2010.

[25] L. J. Brillson, "Nanoscale luminescence spectroscopy of defects at buried interfaces and ultrathin films," *Journal of Vacuum Science & Technology B: Microelectronics and Nanometer Structures Processing, Measurement, and Phenomena*, vol. 19, no. 5, pp. 1762–1768, 2001.

[26] J. H. Choi, H. Y. Ahn, Y. S. Lee, K. Park, T.-H. Kim, K. S. Cho, C. W. Baik, S. I. Kim, H. Yoo, E. H. Lee, B. L. Choi, S.-D. Kim, Y.-W. Kim, M. Kim, and S. Hwang, "Gan light-emitting diodes on glass substrates with enhanced electroluminescence," *J. Mater. Chem.*, vol. 22, pp. 22 942–22 948, 2012.

[27] J. B. Baxter, F. Wu, and E. S. Aydil, "Growth mechanism and characterization of zinc oxide hexagonal columns," *Applied Physics Letters*, vol. 83, no. 18, pp. 3797–3799, 2003.

[28] C. Li, M. Gao, C. Ding, X. Zhang, L. Zhang, Q. Chen, and L.-M. Peng, "In situ comprehensive characterization of optoelectronic nanomaterials for device purposes," *Nanotechnology*, vol. 20, no. 17, p. 175 703, 2009.

[29] J. H. He, P. H. Chang, C. Y. Chen, and K. T. Tsai, "Electrical and optoelectronic characterization of a zno nanowire contacted by focused-ion-beam-deposited pt," *Nanotechnology*, vol. 20, no. 13, p. 135 701, 2009.

[30] B. G. Yacobi and D. B. Holt, "Cathodoluminescence scanning electron microscopy of semiconductors," *Journal of Applied Physics*, vol. 59, no. 4, R1–R24, 1986.

CHAPTER 2
Multi-physical Characterization of Micro- and Nanomaterials: A Review

Multi-physical Characterization of Micro- and Nanomaterials: A Review

Juntian Qu and Xinyu Liu*

Department of Mechanical Engineering, McGill University, 817 Sherbrooke Street West, Montreal, Quebec H3A 0C3, Canada

*Corresponding author: xinyu.liu@mcgill.ca.

To be submitted.

ABSTRACT: Functional micro- and nanomaterials possess exceptional mechanical, electrical and optical properties which have significantly benefited their diverse applications to a variety of scientific and engineering problems. In order to fully understand their characteristics and further guide their synthesis and device application, the multi-physical properties of these micro- and nanomaterials need to be characterized accurately and efficiently. Microelectromechanical systems (MEMS) were often employed for mechanical characterization of micro- and nanomaterials due to its advantages such as high sensing resolution, small footprint, and precise sample alignment. Moreover, among various experimental tools for nanomaterial characterization, scanning electron microscopy (SEM) based platforms provide merits of high imaging resolution, accuracy and stability, well-controlled testing conditions, and the compatibility with other high-resolution material characterization techniques (e.g., atomic force microscopy); thus, various SEM-enabled techniques have been well developed for characterizing the multi-physical properties of nanomaterials. In this review, we summarize existing MEMS-based platforms for mechanical characterization of micro/nano materials and SEM-based platforms for nanomaterial multi-physical (mechanical and electrical) characterization, outline critical experimental challenges for nanomaterial optical characterization in SEM, and discuss potential demands of the SEM-based platforms to characterizing multi-physical properties of the nanomaterials.

Index Terms - Microelectromechanical systems (MEMS), mechanical characterization, scanning electron micscopy (SEM), nanomaterial, multi-physical characterization

2.1 Introduction

The last two decades have witnessed the extensive research on micro- and nanomaterials because of their exceptional promise in science and technology. Based on structural dimension, existing micro- and nanomaterials fall into four categories of nanostructures: zero-dimensional structures (e.g., nanoparticles, nanospheres, and isolated molecules) [1], one-dimensional structures (e.g., micro/nanowires, nanobelts, micro/nanotubes, and nanoribbons) [2, 3, 4], two-dimensional structures (e.g., micro/nano-films, grapheme, and molybdenum disulfide) [5, 6], and three-dimensional structures (e.g., 3D microstructures, nanocombs, nanoflowers and nanocups) [7, 8, 9]. Due to their superior physical properties and unique micro/nanoscale morphologies, these micro- and nanomaterials have been widely used for a variety of applications such as next-generation electronics, nanocomposite synthesis, sustainable energy, biosensing [10, 11, 12] and (opto)electronics [13]. The mechanical, electrical, and optical properties of these micro- and nanomaterials play critical roles in their practical uses, and the experimental determination of these properties is thus of major concern from the perspective of both nanomaterial synthesis and applications.

The explosive growth of micro-electro-mechanical systems (MEMS) provides new methods to characterize nanoscale materials, as described in several review articles [14]. The broad displacement and load ranges offered by the MEMS platforms can be easily applied to strain-stress tests of most nanomaterials [15, 16, 17]. The MEMS platforms possess high load and displacement resolutions and thus can achieve precise sample alignment and manipulation [18, 19, 20]. Moreover, the MEMS platforms have the potential to package the testing setup into a monolithic chip.

Among various experimental techniques employed for nanomaterial characterization, emerging technique of nanorobotic manipulation in scanning electron microscopy (SEM) has enabled various multi-terminal characterization of nanomaterials and nanostructures, such as electrical and mechanical measurements [21, 22]. On one hand, nanoanipulation has filled the gap between top-down and bottom-up approaches and realized position control at the nanometer scale [23], and provides effective strategy for the property characterization of individual nanoscale materials and the construction of nanoscale devices [23]. On the other hand, SEM can provide real-time imaging

with nanometer resolution and a large scanning area, which enables the development and integration of robotic nanomanipulation systems inside large vacuum chamber to realize simultaneous imaging and direct interactions with objects at the sub-micrometer and nanometer scales [21]. In addition, SEM can also be integrated with the latest technology (e.g., electron beam lithography (EBL) and focused ion beam (FIB)) to perform *in-situ* nanomaterial engineering and fabrication [24].

Benefiting from above merits, the combination of nanomanipulation technique and SEM has extended both our eyes and hands simultaneously to nanoscale providing an intuitionistic, real-time and *in-situ* way to study nanomaterials and perform nanomaterial characterization in SEM [22]. However, due to existing challenges in the optics integration into SEM, most nanomaterial *in-situ* characterization techniques in SEM are limited in mechanical, electrical and electro-mechanical measurements, few work has been reported for optical characterization of nanomaterials.

This review presents a survey of recent advances in MEMS-based mechanical characterization of micro- and nanomaterials, and in multi-physical characterization of nanomaterials in SEM, including mechanical, electrical and electro-mechanical characterization. Challenges and limitations of the optical characterization in SEM are analyzed, and prospects for multi-physical nanomaterial characterization are also discussed.

2.2 MEMS-based Mechanical Characterization

2.2.1 MEMS-based Tensile Testing

The MEMS-based tensile testing has been applied to characterizing 1D nanostructures (e.g., nanowires, nanotubes, and nanoribbons), and can measure the sample's mechanical properties such as Youngs modulus, failure strain, and fracture strength [25]. In a tensile test, a 1D nano-sample is mounted across a micrometer-sized gap on a MEMS device, and an on-chip micro-actuator stretches the sample from one side of the gap and a micro force sensor measures the tension force of the sample on the other side of the gap. The elongation (thus tension strain) of the sample can be quantified via high-resolution imaging (using an optical or electron microscope) [20, 26, 27] or on-chip measurement of the sample-mounting gap size [28].

Various typical MEMS platforms were developed for tensile test in SEM, taking advantage of its high-resolution real-time imaging capability for *in-situ* observation of materials behaviors. Tracing back to the year of 2001, M. A. Haque and M. T. A. Saif [29] have proposed the potential application of MEMS actuators on micromechanical testing in an SEM chamber, based on a demonstration of uniaxial tensile test on freestanding thin films in the micro-submicrometer-scale using MEMS devices. The fact of very small overall setup size facilitates the *in-situ* observation of materials behavior in SEM chamber [29]. Zhu et al. [26] reported the development of a material testing system for *in-situ* electron microscopy (EM) mechanical testing of nanostructures, and demonstrated *in-situ* EM testing of free-standing polysilicon films, metallic nanowires, and carbon nanotubes. Espinosa et al. [30] developed the first MEMS-based material testing scheme that can continuously observe specimen deformation with subnanometer resolution and simultaneously measure tension force with nano-newton resolution. B. Pant et al. [20] proposed a versatile MEMS material testing setup that supports both *in-situ* and *ex-situ* testing of nanomaterial with high accuracy and precision. Except for abovementioned work, there are also MEMS material testing systems for characterizing 2D nanoscale films [31, 32] and 1D nanomaterials [18, 33].

Among various types of nanomaterials *in-situ* characterized by MEMS-based tensile platforms, carbon nanotubes (CNT) is the reprensentative one. The mechanical properties of CNT were characterized by various *in-situ* MEMS platforms in SEM: as shown in Figure 2–1(a), *in-situ* tensile loading of a templated carbon nanotube (T-CNT) was reported in [34], where the load was derived from the bending of the direct force-sensing beam and the elongation of the specimen can be obtained from SEM images. Peng et al. [35] employed *in-situ* MEMS tensile tester and exploited the excellent mechanical properties of CNTs with extreme high fracture strength. As shown in Figure 2–1(b), a multiwalled nanotube was bridged between the gap of the actuator (left) and the load sensor. Also, the *in-situ* mechanical characterization of free-standing cofabricated polysilicon films and multiwalled carbon nanotubes (MCNTs) in SEM was employed as a validation MEMS-based material tensile testing system, which for the first time achieved continuous observation of the specimen deformation and load measurement electronically with nano-Newton resolution [30].

Zhu et al. [26, 36] designed a MEMS device for the tensile testing of CNTs with two types of actuators: thermal and electrostatic actuators. The device with a thermal actuator [26] was used for displacement-controlled testing, and the one with a comb-drive electrostatic actuator [36] for force-controlled testing.

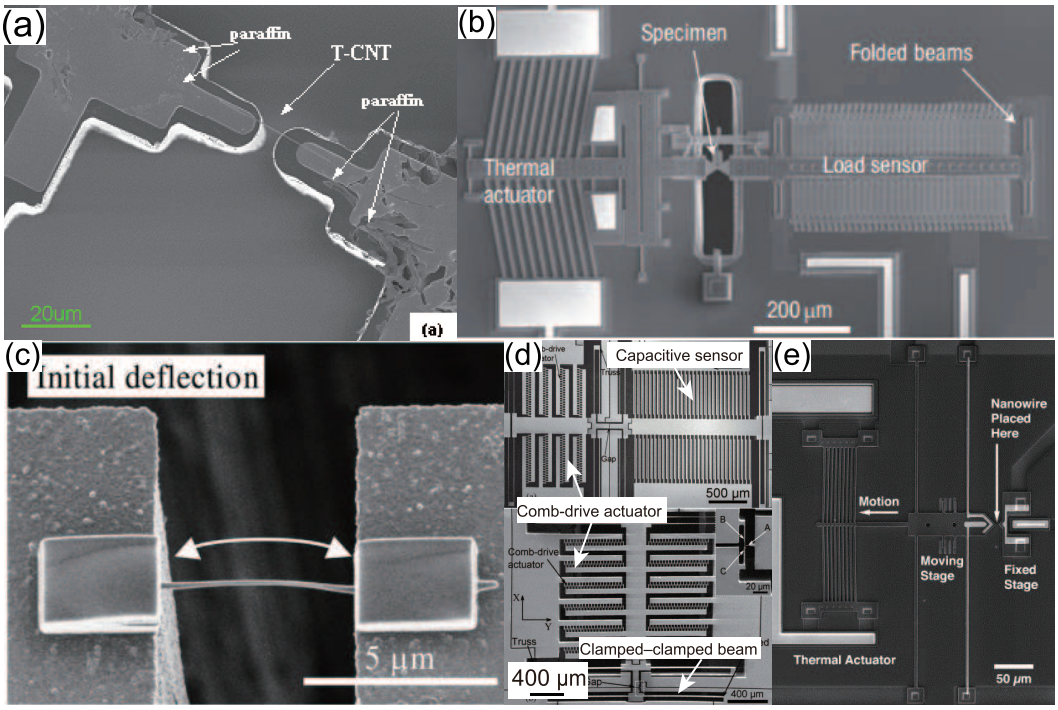

Figure 2–1: MEMS-based *in-situ* mechanical tensile characterization of nanomaterials. (a) *In-situ* tensile loading of a templated carbon nanotube (T-CNT). (b) *In-situ* MEMS tensile tester for mechanical characterization of multiwalled nanotubes (MCNTs). (c) FE-SEM micrograph of a carbon nanowire with initial deflection. (d) Two types of nanotensile stages: top picture shows stage with capacitive sensor and bottom one with a clamped-clamped beam force sensor. (e) Microfabricated tensile test structure consisting of electrically isolated moving and fixed stages.

Except for CNTs, the mechanical properties of a series of nanowires have also been characterized by *in-situ* MEMS platforms in SEM: Kiuchi et al. [33] employed electrostatic actuated nano tensile testing devices (EANATs) to measure the mechanical properties of single carbon nanowire which is suspended between actuation beams (Figure 2–1(c)), and the Young's modulus modulus and fracture stress-strain of the nanowires were accurately obtained. Zhang et al. [37] performed uniaxial quasi-static tensile testing on individual nanocrystalline Co NWs in SEM using on-chip MEMS tensile testing system consisting of a comb drive actuator and a clamped-clamped beam

force sensor. As an extended work, Zhang et al. [38] further developed two types of electrostatically actuated tensile stages with either a differential capacitive sensor or a clamped-clamped beam force sensor for mechanical characterization of individual Si NWs, as shown in Figure 2–1(d). Besides, the fracture mechanism of zinc oxide nanowires was investigated under uniaxial tensile loading utilizing a MEMS-based nanoscale material testing stage [39]. Employing thermal actuator, Brown et al. [40] reported direct tensile tests on n-type (Si-doped) gallium nitride single crystal nanowires (GaN NWs), as shown in Figure 2–1(e), where tensile strength of NWs were characterized and the failure modes were analyzed.

Table 2–1: MEMS-based Mechanical Characterization of Micro- and Nanomaterials.

Testing Types	Materials	End effectors	References
Tensile	**2D Thin Films & Beams**		
	Pt films	thermal actuator	[15]
	freestanding Al films	electrostatic actuator	[29, 31]
		bent-beam thermal actuators	[32]
	freestanding polySi film	thermal actuator	[26]
	nanocrystalline Ni nanobeam	thermal actuator	[20]
	CNTs		
	MCNTs	thermal actuator	[35, 26]
		electrostatic actuator	[30, 36]
	T-CNT	thermal expansion beams	[34]
	1D Nanowires		
	Ni nanowires	nanoindenter head	[18]
	Carbon nanowires	electrostatic actuator	[33]
	Co nanowires	electrostatic actuator	[37]
	Si nanowires	electrostatic actuator	[38]
	ZnO nanowires	electrostatic actuator	[39]
	GaN nanowires	thermal actuator	[40]
Bending	polyacrylonitrile nanofibers	folded-beam loadcell	[17]
	microcantilever aluminum beam	comb drive probe	[29]
	thin-film polysilicon micro-structures	rotary comb-drive actuator	[41]

2.2.2 MEMS-based Bending Testing

Similar to tensile tests, mechanical properties of nanomaterials can also be evaluated via MEMS-based bend testing, which represents another type of widely used experimental technique [42]. A typical MEMS-based bend testing setup [42] is shown in Figure 2–2(a), where a cantilever

beam (co-fabricated with the MEMS device) is moved by a comb-drive electrostatic actuator and bent against a fixed block. Haque and Saif [29] proposed a MEMS-based setup, as shown in Figure 2–2(b), which employs a comb-drive electrostatic actuator to bend test a 100 nm thick aluminum cantilever beam. The applied force was calculated using the pre-calibrated loading equation of the actuator, and the beam deformation was measured via high-resolution imaging. Corigliano et al. [41] proposed a rotary comb-drive actuator (Figure 2–2(c)) and a parallel-plate electrostatic actuator (Figure 2–2(d)) for in-plane and out-of-plane bend testing of thin-film (700 nm) polysilicon micro-structures, respectively. The micro-structures were co-fabricated via a commercial surface micromachining process, which allows for nanometer-thick polysilicon structures to be attached to the bottom of micrometer-think polysilicon MEMS structures. This co-fabrication process eliminates the need for nano-sample addition after MEMS device fabrication (which could be technically challenging).

Based on above descriptions and discussions, the MEMS-based mechanical characterization techniques of micro- and nanomaterials are summarized in Table 2–1, classified by different testing types and different categories of materials.

2.3 Multi-physical Characterization in SEM

Regarding the topic of SEM-based nanomaterial characterization, there are some several reviews in the literature: Fukuda et al. [43] reviewed the assembly of nanodevice and the *in-situ* property characterization of carbon nanotubes through nanorobotic manipulation. Shi et al. [21] also reviewed the applications of nanorobotic manipulation in the characterization of nanomaterials and nanostructures. Haque et al. [44] and Zhu et al. [45] reviewed the recent advances in MEMS-based devices for nanomechanical characterization. Besides, Fukuda et al. [46] and Shen et al. [47] reviewed the advanced applications of micro-nanorobotic manipulation on single-cell analysis and characterization in E-SEM.

In the following sections we will focus our review on the topic of multi-physical characterization of nanomaterials in SEM, including mechanical, electrical and electro/mechanical fields-coupled characterization. Different from the previous review [21] focusing on nanorobotic manipulation

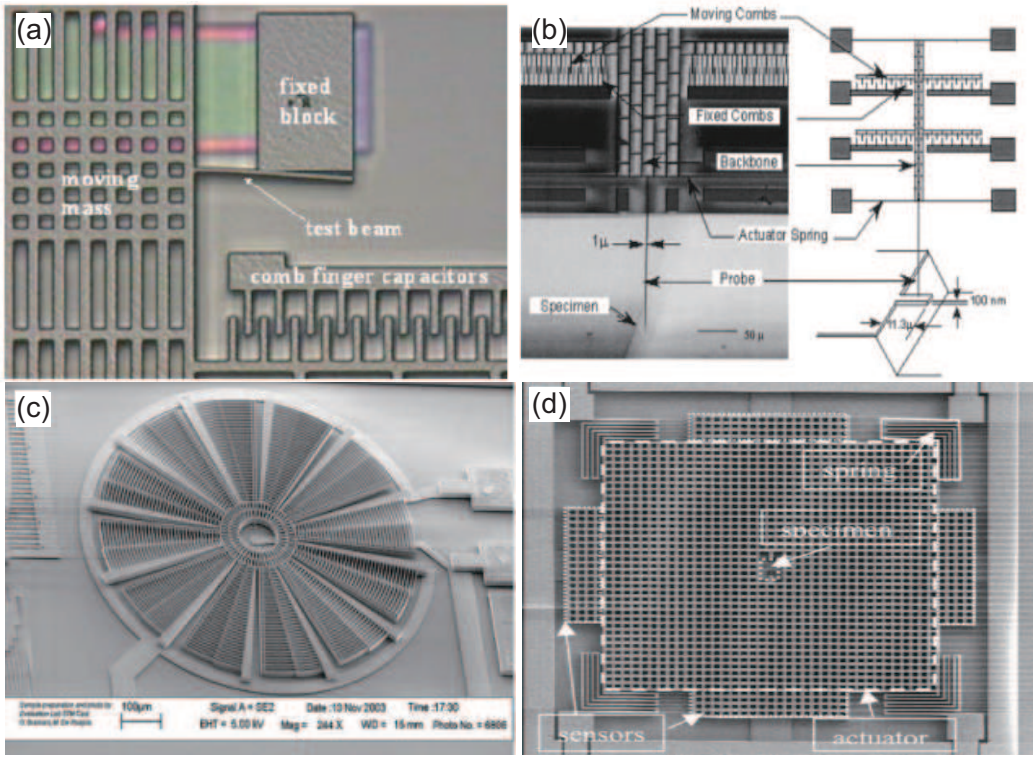

Figure 2–2: MEMS-based mechanical bending testing platforms.

systems, we will mainly discuss the characterization methodologies based on different testing types (experimental setups) in each field. In the meanwhile, we will analyze the current status of optical-measurement-related nanomaterial characterization in SEM.

2.3.1 Mechanical Characterization in SEM

The understanding of mechanical properties of nanomaterials plays important roles in miniaturized electronic, optical, thermal, and electromechanical systems. However, due to the scaling effects and geometric differences, when the surface-to-volume ratio increases along with the decreased size of structures, nanostructures such as nanowires (NWs), carbon nanotubes (CNTs), and ultrathin films tend to exhibit significantly different mechanical properties compared with their bulk counterparts [48, 49, 50], which means that we cannot easily deduce nanomaterial mechanical properties from bulk properties. Besides, the well-established techniques for mechanical characterization at macro-scale cannot be totally transplanted to nanoscale in the respect of equipment and resolution limitations [51]. SEM-based nanomanipulation deals with above challenges for

mechanical characterization of nanomaterials in various ways, which are summarized and classified by the testing type (Table 2–2).

In-situ bending test was performed on individual multi-walled carbon nanotubes (MCNTs) to characterize its Young's modulus, where the bending force was detected by a piezo-resistive atomic force microscope (AFM) probe [52], as shown in Figure 2–3(a). Also the individual MCNTs Young's modulus can be determined by *in-situ* buckling test [53, 43], as shown in Figure 2–3(b). An individual MCNT was EBID-fixed with AFM cantilever probe via nanomanipulation and the buckling force was measured by the deflection of cantilever beam [43].

In-situ tensile test [54] was employed to study the strength and breaking mechanism of MCNTs, as shown in Figure 2–3(c). An individual MCNT was EBID-mounted between two opposing AFM tips with different cantilever stiffness, the upper rigid cantilever was driven upward to apply tensile load to the MCNT, and the tensile force was determined by tracking the deflection of the lower soft cantilever [54]. With a similar principle, mechanical characterization of InGaAs/GaAs nanosprings [55], Si nanowires [56, 57] and Ag nanowires [58] were also performed by *in-situ* tensile tests, as shown in Figure 2–3(d). Accurate strain measurements based on high-resolution SEM imaging of Ag NWs facilitated the acquisition of full spectrum of mechanical properties including Young's modulus, yield strength, and ultimate tensile strength [58].

Besides above testing methods, for fragile two-dimensional materials, as a nondestructive assessment method, *in-situ* nanoindentation measurements have been employed to examine the mechanical properties of a few-layer graphene membrane [59], individual graphene flakes [60] (Figure 2–3(e)) and nanopaper made of microfibrillated cellulose [61] (Figure 2–3(f)), where characteristic force-displacement curves were recorded during the indentation process to extract the Young's modulus. Also, local stiffness of InP suspended micromembrane was first-time measured by a tuning-fork-based dynamic force sensor inside SEM [62].

2.3.1.1 ESEM-based Mechanical Characterization of Biological Cells

For cell mechanical characterization in Environmental SEM (ESEM), standard AFM cantilevers were modified using FIB etching and deposition to produce different types of functional

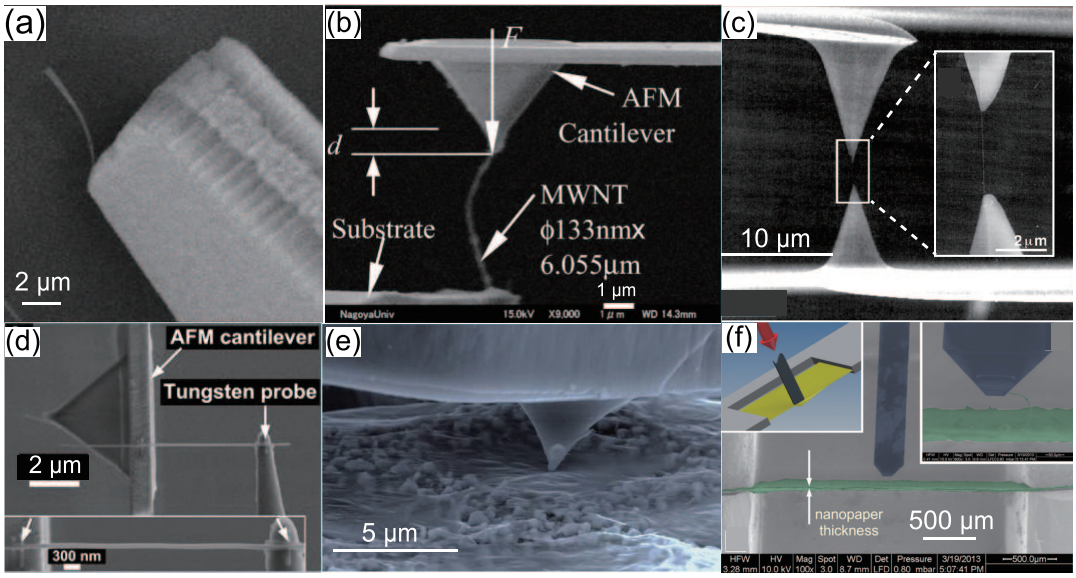

Figure 2–3: SEM-based *in-situ* mechanical characterization of nanomaterials. (a) Deflection of an individual multiwalled carbon nanotube (MWCNT) using a piezo-resistive atomic force microscope (AFM). (b) *In-situ* mechanical characterization of a nanotube by buckling test. (c) Tensile test of individual MCNT, inset of (c) shows the enlarged view of MCNT under tensile force. (d) Tensile test of a single Ag NW, inset of (d) shows a high-resolution SEM image of the NW for strain measurement. (e) The AFM probe is deflecting the graphene flake while measuring the acting forces. (f) Measurement scene of nanopaper inside SEM: the top left inset shows the streched nanopaper, the top right inset shows the nanopaper thickness measurement.

Table 2–2: Mechanical Characterization of Nanomaterials in SEM.

Testing Types	Nanomaterials	Properties	References
Bending	MCNTs	Young's modulus	[52]
Buckling	MCNTs	Young's modulus	[53, 43]
Tensile	MCNTs	strength and breaking mechanism	[54]
	InGaAs/GaAs nanosprings	stiffness	[55]
	Si nanowires	yield strength	[56, 57]
	Ag nanowires	yield, ultimate tensile strength	[58]
Nanoindentation	graphene membrane	elastic stiffness and Young's modulus	[59]
	graphene flakes	Young's modulus	[60]
	nanopaper	Young's modulus	[61]
	InP membranes	local stiffness	[62]
E-SEM for Biological Cells			
Nanomaterials	Properties	End-effectors	References
Wild type yeast cells	single cells adhesion force	nanofork	[63, 64]
	cell-cell adhesion force	nano-picker	[65]
	cell-surface adhesion force	flat AFM cantilever tips	[66, 67]
	stiffness, viscoelastic properties	soft buckling nanoneedles	[68, 69, 70, 71, 72]
Microbead and biological cell	cell detachment force	FIB etched AFM cantilever	[73]

tools [21], such as nanofork [63], nano-picker [65], soft buckling nanoneedles [68, 69, 70, 71, 72] and flat AFM cantilever tips [66, 67], as shown in Figure 2–4(a)-(c). These customized end-effectors were mounted onto the nanomanipulation system in ESEM for indentation to *in-situ* characterize the stiffness [68, 69, 72] and viscoelastic properties [70] of single cells (Figure 2–4(d)), as well as the mechanical properties of individual yeast cells [66] and cell nucleus [71].

Besides, cell-surface adhesion force is important for cell activities and the development of bio materials, and an *in-situ* cell force measurement system was developed based on nanorobotic manipulation inside an ESEM (Figure 2–4(e)) to characterize the single cell adhesion force [63, 64], cell-surface adhesion force [67], and cell-cell adhesion force [65]. Shen et al. [73] also developed a dynamic force characterization system to investigate the cell detachment process at small scales.

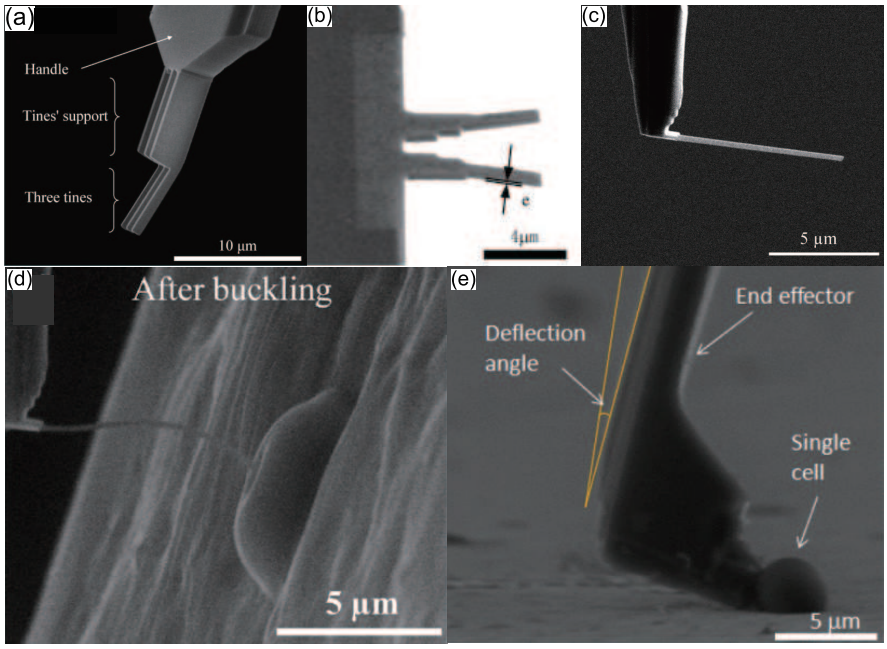

Figure 2–4: E-SEM-based mechanical characterization of biological cells. SEM images of (a) nanofork, (b) nanopicker tip, (c) soft buckling nanoneedle. (d) Single cell global stiffness measurement using Si nanoneedle in buckling condition. (e) Cell adhesion force measurement.

2.3.2 Electrical Characterization in SEM

Better understanding of the electrical properties of nanomaterials will contribute to the development of next-generation nanoelectronics and nano-sensors which promise ultrahigh performance

[74]. Typically there are three kinds of methods adopted during *in-situ* electrical characterization of nanomaterials: four-point, two-point and three-point probing.

2.3.2.1 Four-point Probing

Four-point measurement is a widely adopted technique to eliminate the effect of contact resistance, and has been used for quantifying electrical properties of various nanomaterials such as metallic nanowires [75] and carbon nanotubes [76].

Similar with *in-situ* mechanical characterization, CNTs were also frequently adopted as the testing material in the SEM-based *in-situ* electrical characterization. Four-point electrical transport study of single CNT [77] was performed by a combinatory low temperature four-probe scanning tunneling microscope (STM) and SEM, as shown in Figure 2–5(a). A reliable nanorobotic system consisting of electrothermal microgrippers and mobile microrobots for automated handling and electrical characterization of CNTs was reported in [78].

Except for CNTs, a series of 2D nanomaterials and nanowires were also electrically characterized using four-point probing technique. To achieve rapid prototyping of graphene-based devices, a nanorobotics platform was developed for time-saving electrical characterization of graphene [79], where four-point probing of graphene flake was shown in Figure 2–5(b). Similarly, a four-point probe measurement of individual SnO_2 nanowires was achieved by visual servo automated nanomanipulation inside SEM [80], as shown in Figure 2–5(c).

2.3.2.2 Two-point Probing

Compared with four-point probing, there are still experimental scenarios in which four-point probing is less feasible for electrical characterization of nanomaterials. For instance, certain types of nanomaterials (e.g., III-nitride nanorods) have relatively low aspect ratios, making it difficult to establish four-point contacts along the sample length. Additionally, to characterize as-grown nanowires vertically attached to their growth substrate, it is more convenient to conduct *in-situ* two-point nanoprobing, with one probe on top of a nanowire and the other on the growth substrate [81].

For CNTs-related two-point electrical characterization, back to 2004, Peng et al. [82] reported a four nanoprobe system in SEM for two-point current-voltage (I-V) measurement of carbon nanotube, as shown in Figure 2–5(d). Chen et al. [83] obtained linear I-V measurement curves on MCNTs by establishing two-point Ohmic contacts on a CNT using the Joule heating effect.

Table 2–3: Electrical Characterization of Nanomaterials in SEM.

Testing Types	Nanomaterials	Properties	References
Four-point Probing	Boron nanowires	conductivity	[75]
	CNTs	current-voltage characteristics	[76, 77, 78]
	graphene flake	conductance	[79]
	SnO_2 nanowires	current-voltage characteristics	[80]
Two-point Probing	InN nanowires	electrical transport properties	[81]
	MCNTs	current-voltage characteristics	[82, 83]
	$GdSi_2$ nanowires	electrical transport properties	[84]
	Bi_2S_3 nanowires	current-voltage characteristics	[85]
Three-point Probing	$GdSi_2$ nanowires	field effect measurements	[83]
	Si nanowires	electrical conductance property	[86]
E-SEM for Biological Cells			
Nanomaterials	Properties	End-effectors	References
W303 Yeast Cells	single cells electrical conductivity	dual nanoprobes	[87]
W303 Yeast Cells	single pulses current measurement	ESEM nanomanipulator system	[88]
Human embryonic kidney cell	current response to indentation force	robot-assisted AFM manipulation system	[89]

A bottom-up technique for nanomanipulation combining STM and SEM was proposed in [84], the author fabricated two nanocontacts at the end of the $GdSi_2$ nanowire and performed direct electrical transport measurement. A metal-semiconductor-metal (M-S-M) model for quantitative analysis of current-voltage characteristics of semiconducting nanowires is proposed in [85] and two-terminal probing was employed for experimental I-V characterization of Bi_2S_3 nanowire transistor.

2.3.2.3 Three-point Probing

Three-point field effect measurements were carried out on CNT by Chen et al. [83] using three-point probing technique where a third probe employed as the gate pole, illustrated in Figure 2–5(e). *In-situ* three-point electrical nanotransport measurements of individual $GdSi_2$ nanowires were carried out to investigate the electrical conductance property, where Au-coated STM tip was employed as the third probe [86], as shown in Figure 2–5(f).

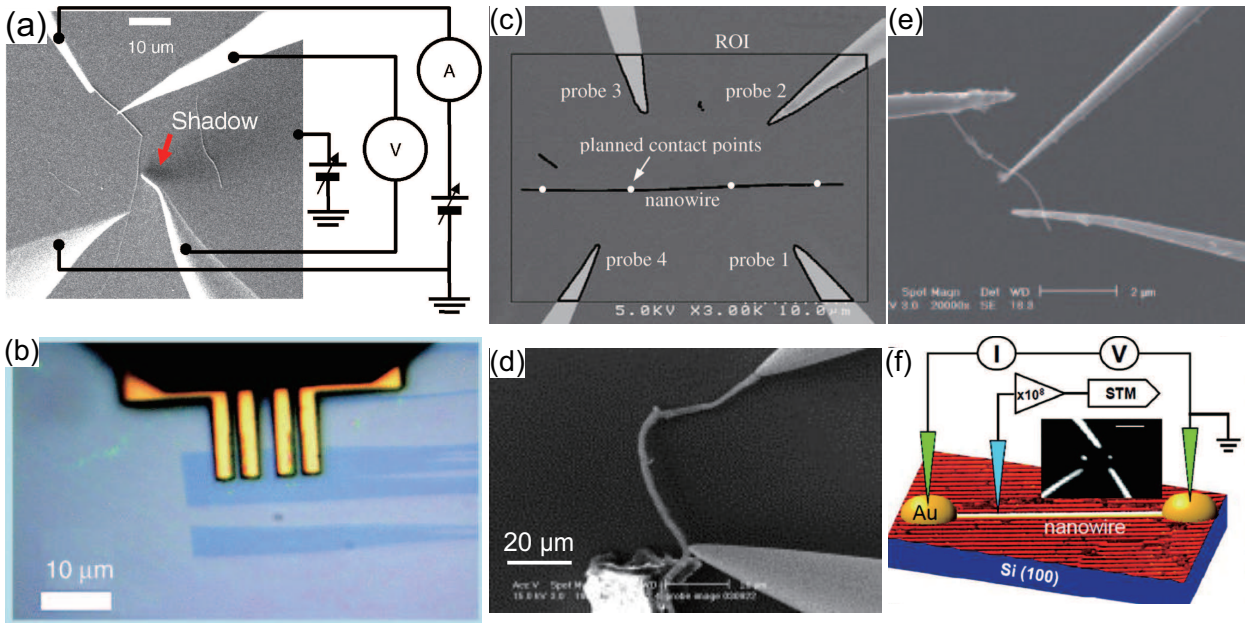

Figure 2–5: SEM-based *in-situ* electrical characterization of nanomaterials. (a) Four-point electrical transport measurement of single CNT. (b) Four-point probing of graphene flake. (c) Visual servo automated four-point probing of single nanowire. (d) Two-point electrical measurement of single nanotube by using two nanoprobes. (e) Three-point measurement configurations for *in-situ* electrical transport and local density of states on a single $GdSi_2$ nanowire.

2.3.2.4 E-SEM-based Electrical Characterization of Biological Cells

The electrical characterization of single cells is challenging cause deep penetration of nanoprobe into the cells will burst it with high stress level risk [46], this issue was solved by performing short penetration of dual nanoprobe and the single cells electrical conductivity was measured [87] . Besides, for the first time, the electrical property of single cells under native condition was reported in [88], where single pulses current measurement was carried out on single cells using dual nanoprobe via a ESEM nanomanipulator system. Also, the electrical response of the human embryonic kidney cell corresponding to external mechanic stimulation was studied by Zhang [89] based on a robot-assisted AFM manipulation system. However, there are still some challenges for electrical characterization of the single cell electrical conductivity, such as limited throughput and sensing ability of robotic manipulation system [47].

Based on above reviews and discussions, the electrical characterization of nanomaterials in SEM are summarized in Table 2–3, classified by different testing types, categories of nanomaterials and different kinds of end-effectors.

2.3.3 Electro-mechanical Characterization in SEM

In addition, the intrinsically coupled electromechanical properties of nanomaterials such as piezo-electrical [90] and piezo-resistive [91, 92] properties have provided special routes of detecting mechanical loading from the electrical change of the nanomaterial and controlling mechanical deformation of nanomaterials via electrical excitation. In the meanwhile, the electromechanical characterization of thin films, nanowires, and nanobelts benefit their potential applications in biosensor development [90, 93] actuators, and motion-controllers [42]. Therefore, it is of great interest to carry out dual-field electro-mechanical characterization of nanomaterials [94, 95].

2.3.3.1 Electro-mechanical Characterization

Tracking back to the year of 1999, there has been reported work [96] exploring the correlation between mechanical and electrical properties of carbon nanotubes, where carbon nanotubes were stressed while monitoring their conductivity under real-time SEM inspection. Subsequently, the electro-mechanical characterization of carbon nanotubes [22, 97, 98] was carried out to investigate the coupling effect between its mechanical and electrical properties, such as the resistance SEM *in-situ* measurement of CNT versus the stress/strain property [97], the electrical properties of various types of suspended single-walled CNTs under the influence of tensile stretching [98], as well as the effects of axial strain on electrical transport properties of individual thin CNTs [22].

2.3.3.2 Piezo-resistive Characterization

The piezoresistance effect of silicon nanowires has also been widely investigated [99] in order to improve the performance of silicon transistors. For the first time, the giant piezoresistance effect in Si nanowires (as shown in Figure 2–6(a)) was discovered in [99], which predicted significant perspective in nanowire-based flexible electronics and NEMS. The phenomenon of giant piezoresistance in silicon NWs was further well controlled in [100] for potential application of stress-gated field-effect transistor with a high gauge factor. Anomalous piezoresistance effect [101] was discovered

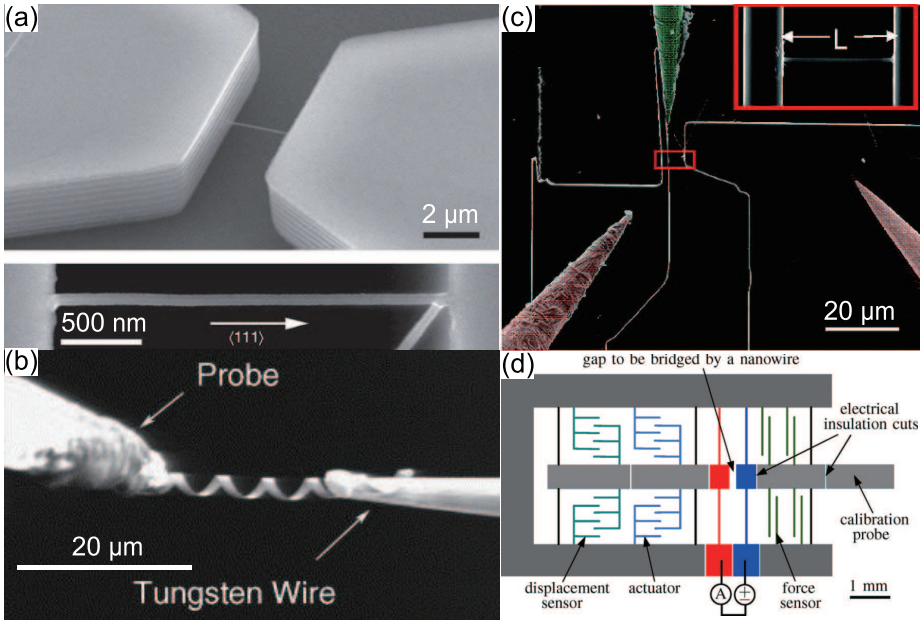

Figure 2–6: Electro-mechanical characterization of nanomaterials. (a) Giant piezoresistance effect: single Si nanowires bridged in the trench of SOI substrate. (b) MEMS loading system for tensile testing of a suspended Si nanowire and measuring the resistance change simultaneously. (c) Conductivity measurement of deformed InGaAs/GaAs nanosprings as electromechanical sensor. (d) MEMS device for electromechanical characterization of nanowires.

for p-type single crystal silicon nanowires under ultrahigh strain, as illustrated in the SEM image in Figure 2–6(c). A Si nanowire was suspended in the microelectromechanical testing module. To avoid the effect of electron beam (e-beam) irradiation during nanomaterial testing, Zhang et al. [102] developed a MEMS device for piezoresistivity characterization of synthetic silicon nanowires, where simultaneous electrical and mechanical characterization of individual Si nanowires could be carried out.

The coupled piezoresistive characterization of some other types of nanostructures has also been carried out through nanomanipulation and electron-beam-induced deposition (EBID) inside SEM. For instance, as shown in Figure 2–6(b), the conductivity of the deformed nanospring [103] was investigated experimentally, the electromechanical properties of InGaAs/GaAs Nanosprings were also characterized in [104], illustrating a potential way to realize electromechanical sensors.

2.3.3.3 MEMS-based Piezo-resistive Characterization

The capability of simultaneous electrical and mechanical measurements of individual nanostructure has demonstrated MEMS devices as a popular platform for piezoresistivity characterization of single nanowires [105, 106, 102] and nanofiber [93] for the development of novel nanomechanical sensors. As shown in Figure 2–6(d), a MEMS device was developed for electromechanical characterization of nanowires [106]. Typically, individual nanowires are grown directly between actuators of MEMS device, so that the uniaxial tensile load can be applied to single NWs; for instance, carbon nanowires (CNWs) were fabricated on electrostatically-actuated nano tensile tester by FIB-CVD [105].

2.4 Challenges and Future Work

2.4.1 Limitations of One-axis Actuation/Sensing in MEMS-based Platforms

In certain scenarios, it is necessary to characterize both compressive and shear properties of the micro- and nanomaterials, which could better reveal the material's mechanical properties under different loading conditions. For instance, in drug delivery, the drug-carrying microcapsules undergo stresses in both compressive and shear directions as they circulate in the body [107], and the characterization of both compressive and shear properties of these microcapsules could lead to tailored synthesis recipes for desired drug-release profiles.

Despite the effectiveness of reported MEMS platforms for mechanical characterization, most of them are limited to one-axis actuation or sensing and thus can only be applied to perform single-axis compression or tensile testing. The only exception existing in the literature is an MEMS-based material microtester that integrates electrostatic actuators and capacitive position and force sensors along two orthogonal axes [108]. The device is operated with an actuation voltage up to 120 V, and the output force of the electrostatic actuators is limited to the micronewton level (up to hundreds of micronewtons). These operation parameters could limit the use of the device in certain applications where low actuation voltages and large output forces are desired. Despite its two-axis actuation and sensing capabilities, this device was only applied to single-axis compression testing of plant cells [108].

2.4.2 Few Optical-Related Characterization in SEM

With the rapid advance of optoelectronic devices, the optical and optoelectronic characterization of nanostructures is becoming more and more popular, which benefits the improvement of optoelectronic device as well as the determination of the correlation between properties and the geometrical parameters of nanostructures. However, as an important characterization platform, SEM was not often utilized for pure optical or optoelectronic characterization of nanomaterials. In the following texts we will give a short review of optical-measurement-related characterization of nanomaterials in SEM and analyze the existing challenges for performing this type of characterization in SEM.

For optical characterization of individual nanostructures, techniques of micro-photoluminescence (micro-PL) [109] and scanning near field optical microscopy [109] were often employed in ambient environment. While in SEM, only the cathodoluminescence (CL) characterization of GaN film [110], GaN crystal [111] and ZnO columns [112] were reported previously. Also, the photoluminescence (PL) and CL characteristics of ZnO nanorod [113] were obtained by customized *in-situ* optical characterization system in SEM. Some optoelectronic characterization were assisted by focused ion beam (FIB) for deposition of metal contacts in an SEM chamber. For instance, the photoconductivity of ZnO NW-based UV photodetectors [114] was characterized with FIB-Pt deposition for electrical contacts.

2.4.3 Challenges for Optoelectronic Characterization in SEM

2.4.3.1 Contact Resistance

In optoelectronic characterization of nanomaterials, the contact resistance between an electrode/nanoprobe and a sample could significantly affect the measured current-voltage (I-V) data; therefore, it is highly desired to minimize the contact resistance during electrical characterization of nanomaterials. Several studies have been reported for reducing the contact resistance of metal electrodes (formed by EBL or EBID) through rapid thermal annealing [115], electric current flowing [116], and e-beam irradiation [117].

2.4.3.2 Efficient Light Detection in Limited-size SEM Chamber

To perform optical characterization in SEM, efficient light collection and detection are necessary. A sizeable paraboloidal mirror was employed in a typical modern setup [118] for light collection in CL test; however, due to the limited space in the SEM chamber, the mirror blocked most other detectors and the electrical nanoprobe integration, thus hindered the simultaneous measurement of electrical and optical properties of nanodevices and nanomaterials. To address this issue, space-saving optical fibers [113] were integrated into the SEM chamber for *in-situ* comprehensive optical characterization of individual optoelectronic nanostructures, providing inspiration for our strategy of optical fiber integration in SEM for optoelectronic characterization.

2.4.4 Demand of Multi-physical Characterization System in SEM

Functional nanomaterials usually have unique multi-physical properties (mechanical, electrical and optical properties) compared with their bulk counterparts. These multi-physical properties not only exist in independent states, but also often coupled with each other and closed correlated as piezoelectric, photoplastic and optoelectronic properties. For instance, widely-studied multifunctional ZnO NWs possess unique physical characteristics such as semiconductivity and piezoelectricity, and have found novel applications in sensors and biomedical science [119]. The observed remarkable photo-induced elastic effect in 1D semiconducting ZnO nanobelt [11] has demonstrating the significance of mechanical, optical, and electronic coupling in 1D nanostructures. Besides, III-nitride NWs (e.g., InN, GaN, AlN) have been pivotal for optoelectronic applications such as ultrahigh-speed nanoscale lasers and photodetectors, full solar spectrum photovoltaic devices, and high-efficiency white light-emitting diodes (LEDs) [120]. These applications usually require optoelectronic characterization of the III-nitride NWs.

Therefore, for abovementioned nanomaterials, a system capable of characterizing the mechanical, electrical or optical property of nanomaterials independently or simultaneously is in highly demanded. SEM-based *in-situ* nanomanipulation technique owns several merits such as high accurate positioning resolution, accurately quantified mechanical excitation and measurement, nondestructive electrical nanoprobing of nanomateirals. These features satisfy all the requirements for

multi-physical characterization of nanomaterials. However, based on the review in Section 2.4.2 and challenges analysis in Section 2.4.3, there are few optical-measurement-related characterization of nanomaterials ever carried out in SEM. This unmet need will be one of my research focuses in this thesis work.

2.5 Conclusion

In the aspect of MEMS-based mechanical characterization, a MEMS-based platform consisting of two-axis actuators and force sensors is highly desired to achieve elastic and viscoelastic characterization of micro- or nanomaterials in both compressive and shear directions. Besides, an *in-situ* multi-physical characterization system in SEM capable of characterizing the mechanical, electrical or optical property of nanomaterials is also in urgent need, which allows *in-situ* assembly and comprehensive optical, electrical and mechanical characterization of individual micro- and nanomaterials. Such a system will enable the investigation of mechanical effects (stress/strain) on the optoelectronic properties of nanomaterials and lead to potential applications of selecting suitable nanostructures and building high-performance nanoelectronic prototype devices.

References

[1] E.-K. Jeon, C.-H. Park, J. A. Lee, M.-S. Kim, K.-C. Lee, H.-M. So, C. Ahn, H. Chang, K. jeong Kong, J.-J. Kim, and J.-O. Lee, "Electromechanical properties of single-walled carbon nanotube devices on micromachined cantilevers," *Journal of Micromechanics and Microengineering*, vol. 22, no. 11, p. 115 010, 2012.

[2] M. F. L. De Volder, S. H. Tawfick, R. H. Baughman, and A. J. Hart, "Carbon nanotubes: present and future commercial applications," *Science*, vol. 339, no. 6119, pp. 535–539, 2013.

[3] Y. Li, F. Qian, J. Xiang, and C. M. Lieber, "Nanowire electronic and optoelectronic devices," *Materials Today*, vol. 9, no. 10, pp. 18 –27, 2006.

[4] Z. L. Wang, "Zno nanowire and nanobelt platform for nanotechnology," *Materials Science and Engineering: R: Reports*, vol. 64, no. 3, pp. 33 –71, 2009.

[5] C. L. Freeman, F. Claeyssens, N. L. Allan, and J. H. Harding, "Graphitic nanofilms as precursors to wurtzite films: theory," *Phys. Rev. Lett.*, vol. 96, p. 066 102, 2006.

[6] W. Zhao, J.-J. Xu, C.-G. Shi, and H.-Y. Chen, "Fabrication, characterization and application of gold nano-structured film," *Electrochemistry Communications*, vol. 8, no. 5, pp. 773 –778, 2006.

[7] Y. Zhang, N. K. Grady, C. Ayala-Orozco, and N. J. Halas, "Three-dimensional nanostructures as highly efficient generators of second harmonic light," *Nano Letters*, vol. 11, no. 12, pp. 5519–5523, 2011.

[8] C. S. Lao, P. X. Gao, R. S. Yang, Y. Zhang, Y. Dai, and Z. L. Wang, "Formation of double-side teethed nanocombs of zno and self-catalysis of zn-terminated polar surface," *Chemical Physics Letters*, vol. 417, no. 4, pp. 358 –362, 2006.

[9] X. Yang, C. Jin, C. Liang, D. Chen, M. Wu, and J. C. Yu, "Nanoflower arrays of rutile tio2," *Chem. Commun.*, vol. 47, pp. 1184–1186, 2011.

[10] J. Homola, *Springer series on chemical sensors and biosensors*. Sl, 2006.

[11] A. San-Miguel, "Nanomaterials under high-pressure," *Chem. Soc. Rev.*, vol. 35, pp. 876–889, 2006.

[12] Z. Y. Sheng, H. Ronan, Y. Ya, A. Gustavo, S. Rudeesun, Z. Fang, Z. Yan, H. Weihua, P. Ken, M. Laurent, M. Mireille, and W. Z. Lin, "Nanonewton transverse force sensor using a vertical gan nanowire based on the piezotronic effect," *Advanced Materials*, vol. 25, no. 6, pp. 883–888,

[13] R. K. Debnath, R. Meijers, T. Richter, T. Stoica, R. Calarco, and H. Luth, "Mechanism of molecular beam epitaxy growth of gan nanowires on si(111)," *Appl. Phys. Lett.*, vol. 90(12), no. 12, p. 123 117, 2007.

[14] V. T. Srikar and S. M. Spearing, "A critical review of microscale mechanical testing methods used in the design of microelectromechanical systems," *Experimental Mechanics*, vol. 43, no. 3, pp. 238–247, 2003.

[15] K. Abbas, S. Alaie, and Z. C. Leseman, "Design and characterization of a low temperature gradient and large displacement thermal actuators for in situ mechanical testing of nanoscale

materials," *Journal of Micromechanics and Microengineering*, vol. 22, no. 12, p. 125 027, 2012.

[16] S. S. Hazra, M. S. Baker, J. L. Beuth, and M. P. de Boer, "Compact on-chip microtensile tester with prehensile grip mechanism," *Journal of Microelectromechanical Systems*, vol. 20, no. 4, pp. 1043–1053, 2011.

[17] M Naraghi, T Ozkan, I Chasiotis, S. S. Hazra, and M. P. de Boer, "Mems platform for on-chip nanomechanical experiments with strong and highly ductile nanofibers," *Journal of Micromechanics and Microengineering*, vol. 20, no. 12, p. 125 022, 2010.

[18] Y. Ganesan, Y. Lu, C. Peng, H. Lu, R. Ballarini, and J. Lou, "Development and application of a novel microfabricated device for the in situ tensile testing of 1-d nanomaterials," *Journal of Microelectromechanical Systems*, vol. 19, no. 3, pp. 675–682, 2010.

[19] D. Zhang, W. Drissen, J.-M. Breguet, R. Clavel, and J. Michler, "A high-sensitivity and quasi-linear capacitive sensor for nanomechanical testing applications," *Journal of Micromechanics and Microengineering*, vol. 19, no. 7, p. 075 003, 2009.

[20] B. Pant, B. L. Allen, T. Zhu, K. Gall, and O. N. Pierron, "A versatile microelectromechanical system for nanomechanical testing," *Applied Physics Letters*, vol. 98, no. 5, p. 053 506, 2011.

[21] C. Shi, D. K. Luu, Q. Yang, J. Liu, J. Chen, C. Ru, S. Xie, J. Luo, J. Ge, and Y. Sun, "Recent advances in nanorobotic manipulation inside scanning electron microscopes," *Microsystems & Nanoengineering*, vol. 2, no. February, p. 16 024, 2016.

[22] X. L. Wei, Q. Chen, L. M. Peng, R. Cui, and Y. Li, "In situ measurements on individual thin carbon nanotubes using nanomanipulators inside a scanning electron microscope," *Ultramicroscopy*, vol. 110, no. 3, pp. 182–189, 2010.

[23] T. Fukuda, M. Nakajima, P. Liu, and M. R. Ahmad, "Bringing the Nanolaboratory Inside Electron Microscopes," *IEEE Nanotechnology Magazine*, vol. 2, no. 2, pp. 18–31, 2008.

[24] M. F. Chisholm, *Scanning Microscopy for Nanotechnology*. 2006.

[25] G. E. Dieter and D. J. Bacon, *Mechanical metallurgy*. McGraw-hill New York, 1986, vol. 3.

[26] Y. Zhu and H. D. Espinosa, "An electromechanical material testing system for in situ electron microscopy and applications," *Proc. Natl. Acad. Sci. U.S.A.*, vol. 102, no. 41, pp. 14 503–14 508, 2005.

[27] Y. Isono, "Micro/nano materials testing for reliable design of mems/nems," in *The Fourth Symposium Micro-Nanomechatronics for Information-Based Society, 2004.*, 2004, pp. 33–38.

[28] Y. Zhang, C. Ru, X. Liu, Y. Zhong, X. Sun, D. Hoyle, I. Cotton, and Y. Sun, "A mems tensile testing device for mechanical characterization of individual nanowires," in *SENSORS, 2010 IEEE*, 2010, pp. 2581–2584.

[29] M. Haque and M. Saif, "Microscale materials testing using MEMS actuators," *J. Microelectromech. Syst.*, vol. 10, no. 1, pp. 146–152, 2001.

[30] H. D. Espinosa, Y. Zhu, and N. Moldovan, "Design and operation of a MEMS-based material testing system for nanomechanical characterization," *Journal of Microelectromechanical Systems*, vol. 16, no. 5, pp. 1219–1231, 2007.

[31] M. A. Haque and M. T. A. Saif, "Deformation mechanisms in free-standing nanoscale thin films: a quantitative in situ transmission electron microscope study," *Proceedings of the National Academy of Sciences*, vol. 101, no. 17, pp. 6335–6340, 2004.

[32] S. Kumar, M. A. Haque, and H. Gao, "Notch insensitive fracture in nanoscale thin films," *Applied Physics Letters*, vol. 94, no. 25, p. 253 104, 2009.

[33] M. Kiuchi, S. Matsui, and Y. Isono, "Mechanical characteristics of FIB deposited carbon nanowires using an electrostatic actuated Nano Tensile testing device," *Journal of Microelectromechanical Systems*, vol. 16, no. 2, pp. 191–201, 2007.

[34] S. Lu, Z. Guo, W. Ding, D. A. Dikin, J. Lee, and R. S. Ruoff, "In situ mechanical testing of templated carbon nanotubes," *Review of Scientific Instruments*, vol. 77, no. 12, 2006.

[35] B. Peng, M. Locascio, P. Zapol, S. Li, S. L. Mielke, G. C. Schatz, and H. D. Espinosa, "Measurements of near-ultimate strength for multiwalled carbon nanotubes and irradiation-induced crosslinking improvements," *Nat Nano*, vol. 3, no. 10, pp. 626–631, 2008.

[36] Y. Zhu, N. Moldovan, and H. D. Espinosa, "A microelectromechanical load sensor for in situ electron and x-ray microscopy tensile testing of nanostructures," *Applied Physics Letters*, vol. 86, no. 1, p. 013 506, 2005.

[37] D. Zhang, J. M. Breguet, R. Clavel, L. Phillippe, I. Utke, and J. Michler, "In situ tensile testing of individual Co nanowires inside a scanning electron microscope," *Nanotechnology*, vol. 20, no. 36, 2009.

[38] D. Zhang, J. M. Breguet, R. Clavel, V. Sivakov, S. Christiansen, and J. Michler, "In situ electron microscopy mechanical testing of silicon nanowires using electrostatically actuated tensile stages," *Journal of Microelectromechanical Systems*, vol. 19, no. 3, pp. 663–674, 2010.

[39] R. Agrawal, B. Peng, and H. D. Espinosa, "Experimental-Computational Investigation of ZnO nanowires Strength and Fracture," *Nano*, vol. 9, no. 12, pp. 4177–4183, 2009.

[40] J. J. Brown, A. I. Baca, K. A. Bertness, D. A. Dikin, R. S. Ruoff, and V. M. Bright, "Tensile measurement of single crystal gallium nitride nanowires on MEMS test stages," *Sensors and Actuators, A: Physical*, vol. 166, no. 2, pp. 177–186, 2011.

[41] A. Corigliano, F. Cacchione, B. De Masi, and C. Riva, "On-chip electrostatically actuated bending tests for the mechanical characterization of polysilicon at the micro scale," *Meccanica*, vol. 40, no. 4-6, pp. 485–503, 2005.

[42] F. Yang and J. C.-M. Li, *Micro and nano mechanical testing of materials and devices*. Springer, 2008.

[43] T. Fukuda, F. Arai, and L. Dong, "Assembly of nanodevices with carbon nanotubes through nanorobotic manipulations," *Proceedings of the IEEE*, vol. 91, no. 11, pp. 1803–1818, 2003.

[44] M. A. Haque, H. D. Espinosa, and H. J. Lee, "MEMS for in situ testing - Handling, actuation, loading, and displacement measurements," *MRS Bulletin*, vol. 35, no. 5, pp. 375–381, 2010.

[45] Y. Zhu and T. H. Chang, "A review of microelectromechanical systems for nanoscale mechanical characterization," *Journal of Micromechanics and Microengineering*, vol. 25, no. 9, 2015.

[46] T. Fukuda, M. Nakajima, M. R. Ahmad, Y. Shen, and M. Kojima, "A glimpse of current and future technologies Micro- and nanomechatronics," *IEEE Industrial Electronics Megazine*, no. December, pp. 13–22, 2010.

[47] Y. Shen and T. Fukuda, "State of the art: micro-nanorobotic manipulation in single cell analysis," *Robotics and Biomimetics*, vol. 1, no. 1, p. 21, 2014.

[48] D. Maharaj and B. Bhushan, "Scale effects of nanomechanical properties and deformation behavior of au nanoparticle and thin film using depth sensing nanoindentation," *Beilstein journal of nanotechnology*, vol. 5, p. 822, 2014.

[49] R. Agrawal, B. Peng, E. E. Gdoutos, and H. D. Espinosa, "Elasticity size effects in zno nanowires a combined experimental-computational approach," *Nano Letters*, vol. 8, no. 11, pp. 3668–3674, 2008.

[50] T. Namazu, Y. Isono, and T. Tanaka, "Evaluation of size effect on mechanical properties of single crystal silicon by nanoscale bending test using afm," *Journal of Microelectromechanical Systems*, vol. 9, no. 4, pp. 450–459, 2000.

[51] M. F. Pantano, H. D. Espinosa, and L. Pagnotta, "Mechanical characterization of materials at small length scales," *Journal of Mechanical Science and Technology*, vol. 26, no. 2, pp. 545–561, 2012.

[52] S. Fatikow, V. Eichhorn, F. Krohs, I. Mircea, C. Stolle, and S. Hagemann, "Development of automated microrobot-based nanohandling stations for nanocharacterization," *Microsystem Technologies*, vol. 14, no. 4-5, pp. 463–474, 2008.

[53] M. Nakajima, F. Arai, and T. Fukuda, "In situ measurement of young's modulus of carbon nanotubes inside a TEM through a hybrid nanorobotic manipulation system," *IEEE Transactions on Nanotechnology*, vol. 5, no. 3, pp. 243–248, 2006.

[54] R. S. Min-Feng, Oleg Lourie, Mark J.Dyer, Katerina Moloni, Thomas F.Kelly, "Strenght and Breaking Mechanism of Multiwalled Carbon Nanotubes Under Tensile Load," vol. 287, no. January, pp. 1–4, 2013.

[55] D. Bell, L. Dong, B. Nelson, M. Golling, L. Zhang, and D. Gr"utzmacher, "Fabrication and characterization of three-dimensional InGaAs/GaAs nanosprings.," *Nano letters*, vol. 6, no. 4, pp. 725–729, 2006.

[56] Y. Zhu, F. Xu, Q. Qin, W. Y. Fung, and W. Lu, "Mechanical Properties of Vapor-liquid-solid Synthesized Silicon Nanowires," *Nano Letters*, vol. 9, no. 11, pp. 3934–3939, 2009.

[57] S. T. Boles, A. Sedlmayr, O. Kraft, and R. Mönig, "In situ cycling and mechanical testing of silicon nanowire anodes for lithium-ion battery applications," *Applied Physics Letters*, vol. 100, no. 24, 2012.

[58] Y. Zhu, Q. Qin, F. Xu, F. Fan, Y. Ding, T. Zhang, B. J. Wiley, and Z. L. Wang, "Size effects on elasticity, yielding, and fracture of silver nanowires: In situ experiments," *Physical Review B - Condensed Matter and Materials Physics*, vol. 85, no. 4, pp. 1–7, 2012.

[59] S. Zimmermann, T. Tiemerding, T. Li, W. Wang, Y. Wang, and S. Fatikow, "Automated Mechanical Characterization of 2-D Materials using SEM based Visual Servoing," *International Journal of Optomechatronics*, vol. 7, no. 4, pp. 283–295, 2013.

[60] S. Zimmermann, V. Eichhorn, and S. Fatikow, "Nanorobotic transfer and characterization of graphene flakes," *IEEE International Conference on Intelligent Robots and Systems*, pp. 640–645, 2012.

[61] M. R. Mikczinski, G. Josefsson, G. Chinga-carrasco, E. K. Gamstedt, and S. Fatikow, "Nanorobotic Testing to Assess the Stiffness Properties of Nanopaper," vol. 30, no. 1, pp. 115–119, 2014.

[62] J. O. Abrahamians, B. Sauvet, J. Polesel-Maris, R. Braive, and S. Régnier, "A nanorobotic system for in situ stiffness measurements on membranes," *IEEE Transactions on Robotics*, vol. 30, no. 1, pp. 119–124, 2014.

[63] M. R. Ahmad, M. Nakajima, M. Kojima, S. Kojima, M. Homma, and T. Fukuda, "Nanofork for single cells adhesion measurement via ESEM-nanomanipulator system," *IEEE Transactions on Nanobioscience*, vol. 11, no. 1, pp. 70–78, 2012.

[64] Y. Shen, M. Nakajima, S. Kojima, M. Homma, M. Kojima, and T. Fukuda, "Single cell adhesion force measurement for cell viability identification using an AFM cantilever-based micro putter," *Measurement Science and Technology*, vol. 22, no. 11, 2011.

[65] Y. Shen, M. Nakajima, S. Kojima, M. Homma, and T. Fukuda, "Study of the time effect on the strength of cell-cell adhesion force by a novel nano-picker," *Biochemical and Biophysical Research Communications*, vol. 409, no. 2, pp. 160–165, 2011.

[66] M. R. Ahmad, M. Nakajima, S. Kojima, M. Homma, and T. Fukuda, "The effects of cell sizes, environmental conditions, and growth phases on the strength of individual W303 yeast cells inside ESEM," *IEEE Transactions on Nanobioscience*, vol. 7, no. 3, pp. 185–193, 2008.

[67] Y. Shen, M. R. Ahmad, M. Nakajima, S. Kojima, M. Homma, and T. Fukuda, "Evaluation of the single yeast cell's adhesion to ITO substrates with various surface energies via ESEM nanorobotic manipulation system," *IEEE Transactions on Nanobioscience*, vol. 10, no. 4, pp. 217–224, 2011.

[68] M. R. Ahmad, M. Nakajima, S. Kojima, M. Homma, and T. Fukuda, "In situ single cell mechanics characterization of yeast cells using nanoneedles inside environmental sem," *IEEE Transactions on Nanotechnology*, vol. 7, no. 5, pp. 607–616, 2008.

[69] N. M. K. S. H. M. Ahmad M. R. and T. Fukuda, "Buckling nanoneedle for characterizing single cells mechanics inside environmental SEM," *IEEE Transactions on Nanotechnology*, vol. 10, no. 2, pp. 226–236, 2011.

[70] M. R. A. . M. N. . S. K. . M. Homma and T. Fukuda, "Nanoindentation methods to measure viscoelastic properties of single cells using sharp, flat, and buckling tips inside ESEM," *IEEE Transactions on Nanobioscience*, vol. 9, no. 1, pp. 12–23, 2010.

[71] H. Liu, J. Wen, Y. Xiao, J. Liu, S. Hopyan, M. Radisic, C. A. Simmons, and Y. Sun, "In situ mechanical characterization of the cell nucleus by atomic force microscopy," *ACS Nano*, vol. 8, no. 4, pp. 3821–3828, 2014.

[72] Y. Shen, M. Nakajima, Z. Yang, H. Tajima, Z. Najdovski, M. Homma, and T. Fukuda, "Single cell stiffness measurement at various humidity conditions by nanomanipulation of a nano-needle," *Nanotechnology*, vol. 24, no. 14, 2013.

[73] Y. Shen, M. Nakajima, Z. Zhang, and T. Fukuda, "Dynamic Force Characterization Microscopy Based on Integrated Nanorobotic AFM and SEM System for Detachment Process Study," *IEEE/ASME Transactions on Mechatronics*, vol. 20, no. 6, pp. 3009–3017, 2015.

[74] Y. Zhang, X. Liu, C. Ru, Y. L. Zhang, L. Dong, and Y. Sun, "Piezoresistivity characterization of synthetic silicon nanowires using a mems device," *Journal of Microelectromechanical Systems*, vol. 20, no. 4, pp. 959–967, 2011.

[75] L. Xiao, H. Xiao-Bo, L. Jun-Ling, G. Li, H. Qing, S. Dong-Xia, and G. Hong-Jun, "Four-probe scanning tunnelling microscope with atomic resolution for electrical and electro-optical property measurements of nanosystems," *Chinese Phys.*, vol. 14, no. 8, p. 1536, 2005.

[76] Q. Chen, S. Wang, and L.-M. Peng, "Establishing ohmic contacts for in situ current-voltage characteristic measurements on a carbon nanotube inside the scanning electron microscope," *Nanotechnology*, vol. 17, no. 4, p. 1087, 2006.

[77] T. H. Kim, Z. Wang, J. F. Wendelken, H. H. Weitering, W. Li, and A. P. Li, "A cryogenic Quadraprobe scanning tunneling microscope system with fabrication capability for nanotransport research," *Review of Scientific Instruments*, vol. 78, no. 12, 2007.

[78] V. Eichhorn, S. Fatikow, T. Wortmann, C. Stolle, C. Edeler, D. Jasper, O. Sardan, P. Bggild, G. Boetsch, C. Canales, and R. Clavel, "NanoLab: A nanorobotic system for automated pick-and-place handling and characterization of CNTs," *Proceedings - IEEE International Conference on Robotics and Automation*, pp. 1826–1831, 2009.

[79] G. Devices, "Nanorobotic Processing of Graphene," no. July, 2014.

[80] C. Ru, Y. Zhang, Y. Sun, Y. Zhong, X. Sun, D. Hoyle, and I. Cotton, "Automated four-point probe measurement of nanowires inside a scanning electron microscope," *IEEE Transactions on Nanotechnology*, vol. 10, no. 4, pp. 674–681, 2011.

[81] S. Zhao, O. Salehzadeh, S. Alagha, K. L. Kavanagh, S. P. Watkins, and Z. Mi, "Probing the electrical transport properties of intrinsic inn nanowires," *Applied Physics Letters*, vol. 102, no. 7, p. 073 102, 2013.

[82] L. M. Peng, Q. Chen, X. L. Liang, S. Gao, J. Y. Wang, S. Kleindiek, and S. W. Tai, "Performing probe experiments in the SEM," *Micron*, vol. 35, no. 6, pp. 495–502, 2004.

[83] Q. Chen, S. Wang, and L. M. Peng, "Establishing Ohmic contacts for in situ current-voltage characteristic measurements on a carbon nanotube inside the scanning electron microscope," *Nanotechnology*, vol. 17, no. 4, pp. 1087–1098, 2006.

[84] S. Qin, T. H. Kim, Z. Wang, and A. P. Li, "Nanomanipulation and nanofabrication with multi-probe scanning tunneling microscope: From individual atoms to nanowires," *Review of Scientific Instruments*, vol. 83, no. 6, 2012.

[85] Z. Zhang, K. Yao, Y. Liu, C. Jin, X. Liang, Q. Chen, and L.-M. Peng, "Quantitative analysis of current-voltage characteristics of semiconducting nanowires: decoupling of contact effects," *Adv. Funct. Mater.*, vol. 17, no. 14, pp. 2478–2489, 2007.

[86] S. Qin, T.-H. Kim, Y. Zhang, W. Ouyang, H. H. Weitering, C.-K. Shih, A. P. Baddorf, R. Wu, and A.-P. Li, "Correlating Electronic Transport to Atomic Structures in Self-Assembled Quantum Wires," *Nano Letters*, vol. 12, no. 2, pp. 938–942, 2012.

[87] M. R. Ahmad, M. Nakajima, T. Fukuda, S. Kojima, and M. Homma, "Single cells electrical characterizations using nanoprobe via esem-nanomanipulator system," in *2009 9th IEEE Conference on Nanotechnology (IEEE-NANO)*, 2009, pp. 589–592.

[88] M. R. Ahmad, M. Nakajima, M. Kojima, S. Kojima, M. Homma, and T. Fukuda, "Instantaneous and quantitative single cells viability determination using dual nanoprobe inside ESEM," *IEEE Transactions on Nanotechnology*, vol. 11, no. 2, pp. 298–306, 2012.

[89] C. Zhang, P. Li, L. Liu, Y. Wang, Z. Gao, and G. Li, "Development of mechanostimulated patch-clamp system for cellular physiological study," *IEEE/ASME Transactions on Mechatronics*, vol. 19, no. 4, pp. 1138–1147, 2014.

[90] R. Zhu, D. Wang, S. Xiang, Z. Zhou, and X. Ye, "Piezoelectric characterization of a single zinc oxide nanowire using a nanoelectromechanical oscillator," *Nanotechnology*, vol. 19, no. 28, p. 285 712, 2008.

[91] M. Kiuchi, S. Matsui, and Y. Isono, "The piezoresistance effect of fib-deposited carbon nanowires under severe strain," *Journal of Micromechanics and Microengineering*, vol. 18, no. 6, p. 065 011, 2008.

[92] R. J. Grow, Q. Wang, J. Cao, D. Wang, and H. Dai, "Piezoresistance of carbon nanotubes on deformable thin-film membranes," *Applied Physics Letters*, vol. 86, no. 9, p. 093 104, 2005.

[93] J. J. Brown, J. W. Suk, G. Singh, A. I. Baca, D. A. Dikin, R. S. Ruoff, and V. M. Bright, "Microsystem for nanofiber electromechanical measurements," *Sensors and Actuators, A: Physical*, vol. 155, no. 1, pp. 1–7, 2009.

[94] J. H. Han and M. T. A. Saif, "In situ microtensile stage for electromechanical characterization of nanoscale freestanding films," *Review of Scientific Instruments*, vol. 77, no. 4, p. 045 102, 2006.

[95] A Jourdain, P. D. Moor, K Baert, I. D. Wolf, and H. A. C. Tilmans, "Mechanical and electrical characterization of bcb as a bond and seal material for cavities housing (rf-)mems devices," *Journal of Micromechanics and Microengineering*, vol. 15, no. 7, S89, 2005.

[96] H. W. Yu, M.-F., Dyer, M. J., Skidmore, G. D., Rhors and R. S. Lu, X. K., Ausman, K. D., Ehr, J. R. V., Ruoff, "3-dimensional manipulation of carbon nanotubes under a scanning electron microscope. Nanotechnology," vol. 10, p. 244, 1999.

[97] P. A. Williams, S. J. Papadakis, M. R. Falvo, A. M. Patel, M. Sinclair, A. Seeger, A. Helser, R. M. Taylor, S. Washburn, and R. Superfine, "Controlled placement of an individual carbon nanotube onto a microelectromechanical structure," *Applied Physics Letters*, vol. 80, no. 14, pp. 2574–2576, 2002.

[98] J. Cao, Q. Wang, and H. Dai, "Electromechanical Properties of Metallic, Quasimetallic, and Semiconducting Carbon Nanotubes under Stretching," *Physical Review Letters*, vol. 90, no. 15, p. 4, 2003.

[99] R. He and P. Yang, "Giant piezoresistance effect in silicon nanowires," *Nature Nanotechnology*, vol. 1, no. 1, pp. 42–46, 2006.

[100] P. Neuzil, C. C. Wong, and J. Reboud, "Electrically controlled giant piezoresistance in silicon nanowires," *Nano Letters*, vol. 10, no. 4, pp. 1248–1252, 2010.

[101] A. Lugstein, M. Steinmair, A. Steiger, H. Kosina, and E. Bertagnolli, "Anomalous piezoresistance effect in ultrastrained silicon nanowires," *Nano Letters*, vol. 10, no. 8, pp. 3204–3208, 2010.

[102] Z. Yong, L. Xinyu, R. Changhai, Z. Yan Liang, D. Lixin, and S. Yu, "Piezoresistivity Characterization of Synthetic Silicon Nanowires Using a MEMS Device," *Journal of Microelectromechanical Systems*, vol. 20, no. 4, pp. 959–967, 2011.

[103] D. J. Bell, Y. Sun, L. Zhang, L. X. Dong, B. J. Nelson, and D. Grützmacher, "Three-dimensional nanosprings for electromechanical sensors," *Sensors and Actuators, A: Physical*, vol. 130-131, no. SPEC. ISS. Pp. 54–61, 2006.

[104] G. Hwang, H. Hashimoto, D. J. Bell, L. Dong, B. J. Nelson, and S. Scho, "Piezoresistive InGaAs / GaAs Nanosprings with Metal Connectors," *Nano letters*, vol. 9, no. January, pp. 554–561, 2009.

[105] M. Kiuchi, S. Matsui, and Y. Isono, "The piezoresistance effect of FIB-deposited carbon nanowires under severe strain," *Journal of Micromechanics and Microengineering*, vol. 18, no. 6, p. 065 011, 2008.

[106] Xutao Ye, Yong Zhang, Changhai Ru, Jun Luo, Shaorong Xie, and Yu Sun, "Automated Pick-Place of Silicon Nanowires," *IEEE Transactions on Automation Science and Engineering*, vol. 10, no. 3, pp. 554–561, 2013.

[107] A. Fery and R. Weinkamer, "Mechanical properties of micro- and nanocapsules: single-capsule measurements," *Polymer*, vol. 48, no. 25, pp. 7221–7235, 2007.

[108] S. Muntwyler, B. E. Kratochvil, F. Beyeler, and B. J. Nelson, "Monolithically integrated two-axis microtensile tester for the mechanical characterization of microscopic samples," *J. Microelectromech. Syst.*, vol. 19, no. 5, pp. 1223–1233, 2010.

[109] A. Gustafsson, M.-E. Pistol, L. Montelius, and L. Samuelson, "Local probe techniques for luminescence studies of low-dimensional semiconductor structures," *Journal of Applied Physics*, vol. 84, no. 4, pp. 1715–1775, 1998.

[110] L. J. Brillson, "Nanoscale luminescence spectroscopy of defects at buried interfaces and ultrathin films," *Journal of Vacuum Science & Technology B: Microelectronics and Nanometer Structures Processing, Measurement, and Phenomena*, vol. 19, no. 5, pp. 1762–1768, 2001.

[111] J. H. Choi, H. Y. Ahn, Y. S. Lee, K. Park, T.-H. Kim, K. S. Cho, C. W. Baik, S. I. Kim, H. Yoo, E. H. Lee, B. L. Choi, S.-D. Kim, Y.-W. Kim, M. Kim, and S. Hwang, "Gan light-emitting diodes on glass substrates with enhanced electroluminescence," *J. Mater. Chem.*, vol. 22, pp. 22 942–22 948, 2012.

[112] J. B. Baxter, F. Wu, and E. S. Aydil, "Growth mechanism and characterization of zinc oxide hexagonal columns," *Applied Physics Letters*, vol. 83, no. 18, pp. 3797–3799, 2003.

[113] C. Li, M. Gao, C. Ding, X. Zhang, L. Zhang, Q. Chen, and L.-M. Peng, "In situ comprehensive characterization of optoelectronic nanomaterials for device purposes," *Nanotechnology*, vol. 20, no. 17, p. 175 703, 2009.

[114] J. H. He, P. H. Chang, C. Y. Chen, and K. T. Tsai, "Electrical and optoelectronic characterization of a zno nanowire contacted by focused-ion-beam-deposited pt," *Nanotechnology*, vol. 20, no. 13, p. 135 701, 2009.

[115] J.-O. Lee, C Park, J.-J. Kim, J. Kim, J. W. Park, and K.-H. Yoo, "Formation of low-resistance ohmic contacts between carbon nanotube and metal electrodes by a rapid thermal annealing method," *J. Phys. D: Appl. Phys.*, vol. 33, no. 16, p. 1953, 2000.

[116] H. Maki, M. Suzuki, and K. Ishibashi, "Local change of carbon nanotube-metal contacts by current flow through electrodes," *J. Appl. Phys.*, vol. 43, no. 4S, p. 2027, 2004.

[117] A. Bachtold, M. Henny, C. Terrier, C. Strunk, C. Schnenberger, J.-P. Salvetat, J.-M. Bonard, and L. Forr, "Contacting carbon nanotubes selectively with low-ohmic contacts for four-probe electric measurements," *Applied Physics Letters*, vol. 73, no. 2, pp. 274–276, 1998.

[118] B. G. Yacobi and D. B. Holt, "Cathodoluminescence scanning electron microscopy of semiconductors," *Journal of Applied Physics*, vol. 59, no. 4, R1–R24, 1986.

[119] A. Tuantranont, "Applications of nanomaterials in sensors and diagnostics," *Springer Ser. Chem. Sens. Biosens*, vol. 14, 2013.

[120] C. P. Wang, C. W. Liu, and C. Gau, "Silicon nanowire temperature sensor and its characteristic," in *2011 6th IEEE International Conference on Nano/Micro Engineered and Molecular Systems*, 2011, pp. 630–633.

The connection between Chapter 2 and Chapter 3

In Chapter 2, existing MEMS-based mechanical characterization platforms and SEM-based multi-physical characterization platforms were reviewed, and current challenges on these topics were analyzed. In the rest of this thesis, to improve aforementioned limitations in MEMS-based mechanical characterization, a MEMS-based platform integrating two-axis actuators and force sensors will be developed for microscale compression and shear testing of soft materials. To solve existing challenges in SEM-based characterization platforms, a multi-physical characterization system in SEM capable of characterizing the mechanical, electrical or optical property of nanomaterials will be developed.

In Chapter 3, a MEMS-based microgripper, integrating two-axis V-beam electrothermal actuators and tri-plate differential capacitive force sensors will be developed, for microscale compressive and shear testing of soft materials. For the first time, on-chip compressive and shear testing of polydimethylsiloxane (PDMS) microstructures prepared at different crosslinking levels will be demonstrated. The developed system features accurately characterizing compressive and shear properties of a variety of microscale soft materials.

CHAPTER 3
Microscale Compression and Shear Testing of Soft Materials Using A MEMS Microgripper with Two-Axis Actuators and Force Sensors

Microscale Compression and Shear Testing of Soft Materials Using A MEMS Microgripper with Two-Axis Actuators and Force Sensors

Juntian Qu†, Weize Zhang†, Andrew Jung, Simon Silva-Da Cruz, and Xinyu Liu*

Department of Mechanical Engineering, McGill University, Montreal, QC H3A 0C3, Canada

†These authors contributed equally to this work.

*Corresponding author: (xinyu.liu@mcgill.ca)

Published on: *IEEE Transactions on Automation Science and Engineering*, vol. 14, no. 2, 834 - 843, 2016.

ABSTRACT: This paper reports a microelectromechanical systems (MEMS) based microgripper, integrating two-axis actuators and force sensors, for microscale compressive and shear testing of soft materials. The device employs V-beam electrothermal actuators to actuate an active gripping arm and compress or shear a microscale sample grasped at the gripping tips, and two tri-plate differential capacitive sensors for measuring the compressive and shear forces applied to the sample with nanonewton resolution (compressive force resolution: 7.7 nN, and shear force resolution: 57.5 nN). Using the microgripper, we demonstrate, for the first time, on-chip compressive and shear testing of polydimethylsiloxane (PDMS) microstructures prepared at different crosslinking levels. This device, we believe, will be useful for accurately characterizing compressive and shear properties of a variety of microscale soft materials.

Note to Practitioners—The characterization of elastic and viscoelastic properties of micrometer-sized soft materials is of great significance in many disciplines such as biomaterials, pharmaceutics, and cell mechanics. Among various material characterization techniques, methods based on MEMS devices are well recognized for their high resolution, perfect size matching to microscale objects, and excellent cost-effectiveness. However, existing MEMS-based approaches are limited to one-axis (tensile or compression) testing, and cannot measure both compressive and shear properties of soft materials. This paper reports a force-controlled MEMS microgripper with two-axis measurement capabilities for elastic and viscoelastic

testing of PDMS microstructures in both the compressive and shear directions. The platform can facilitate various synthesis and/or characterization studies of microscale soft materials.

Index Terms - Compression and shear testing, microscale soft materials, elastic and viscoelastic properties, microelectromechanical (MEMS) microgrippers, capacitive force sensor, electrothermal actuator.

3.1 Introduction

Micrometer-sized soft materials (e.g., polymeric microcapsules and microparticles) are widely used in a variety of applications such as cell encapsulation and drug delivery [1, 2]. The mechanical properties of these microscale materials are important as they aid in establishing parameters to prevent dose dumping and cell death, influence the release of therapeutic agents, and ultimately determine the materials' performance in specific applications. For instance, in drug delivery, the drug-carrying microcapsules undergo stresses in both compressive and shear directions as they circulate in the body [3]. It is necessary to characterize both compressive and shear properties of the microcapsules, which can be used to guide the material synthesis and achieve the desired drug release profile. In addition, microscale mechanical characterization of soft materials is also important for cell mechanics and disease diagnostics, where the cellular mechanical property could be used as an effective biomarker for facilitating diagnosis of diseases such as cancers [4] and cardiovascular diseases [5], and for detecting cellular defects in mammalian embryos [6, 7].

To characterize the mechanical properties of soft microobjects, a technique capable of measuring low-magnitude forces and microscopic deformations is required [8]. Micropipette aspiration [9, 10], atomic force microscopy (AFM) [11], micro/nano-indentation [12, 13], and magnetic bead measurement [14] are representatives of the widely used techniques for mechanical characterization of microscale soft materials. However, these techniques are limited to quantification of only local mechanical properties of a material.

Compared to the aforementioned techniques, microelectromechanical systems (MEMS) based methods possess many advantages such as high sensing resolution, small footprint, and excellent cost-effectiveness [8]. A variety of MEMS-based platforms have been developed for mechanical testing of different kinds of materials at the micro and nanoscale. For example, several silicon- and polymer-based MEMS devices have been developed for mechanical characterization of single cells [15, 16, 6, 17], and applied to studies in basic cell mechanics and cellular defect diagnostics. Kim et al. [18, 8] put forward a MEMS-based approach to characterizing the elastic and viscoelastic properties of hydrogel microcapsules, and examined the correlation of the material's composition,

mechanical property, and drug-release profile. Christopher et al. [19] created a single-axis MEMS nanopositioning stage for dynamic rheological testing of complex fluids and soft matters; however, the device does not include a dedicated force sensor, and the stage dynamics during testing was used to extract the material properties. Besides the MEMS-based material testing platforms stated above, there are also a cohort of well-developed MEMS platforms for mechanical testing of one-dimensional (e.g., nanowires and nanotubes) [20, 21, 22] and two-dimensional (e.g., graphene and nano-films) [23] nanomaterials.

Besides the MEMS-based platforms that have been demonstrated for material testing, there are also other force-sensing MEMS microgrippers reported in the literature that can be readily adopted for this purpose. Kim et al. [24] developed a monolithic MEMS microgripper with two-axis capacitive force sensors and used it for force-controlled manipulation of biological cells. Xu [25] proposed a microgripper design that can alternatingly measure gripping forces and environment interaction forces (along the direction orthogonal to the gripping force direction) with a single capacitive force sensor. Additionally, a force-controlled MEMS rotary microgripper is has also been developed by Piriyanont et al. [26] on which a null-displacement feedback control technique was implemented for gripping force sensing without moving the force sensing gripping arm.

Despite the effectiveness of these MEMS platforms, most of them are limited to one-axis actuation or sensing and thus can only be applied to performing single-axis compression or tensile testing. The only exception existing in the literature is a MEMS-based material microtester that integrates electrostatic actuators and capacitive position and force sensors along two orthogonal axes [22]. The device is operated with an actuation voltage up to 120 V, and the output force of the electrostatic actuators is limited to the micronewton level ($\leq$ 100's μN). These operation parameters could limit the use of the device in certain application where low actuation voltages and large output forces are desired. Despite its two-axis actuation and sensing capabilities, this device was only applied to single-axis compression testing of plant cells [22].

This paper presents the development of a MEMS microgripper (Figure 3–1) with two-axis electrothermal actuators and capacitive force sensors; and demonstrates, for the first time, microscale

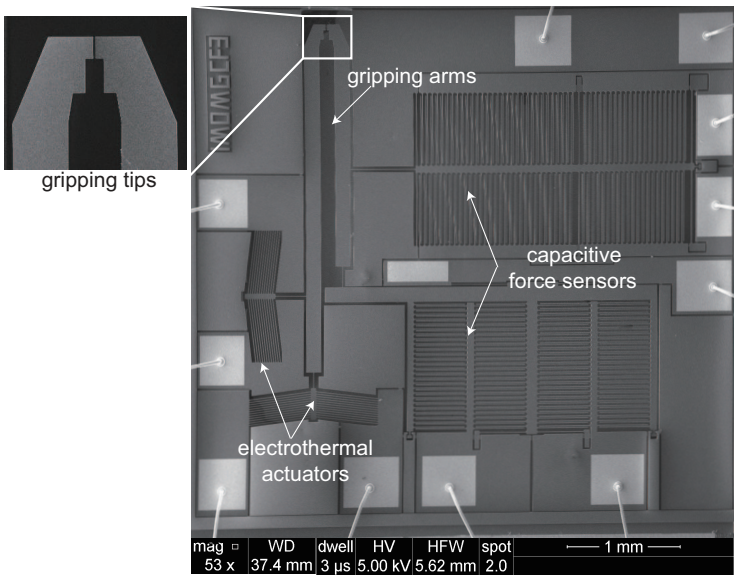

Figure 3–1: SEM photograph of a MEMS microgripper with two-axis electrothermal actuators and capactive force sensors.

elastic and viscoelastic characterization of soft materials in both compressive and shear directions. Two orthogonally arranged V-beam electrothermal actuators are attached to the active gripping arm of the microgripper, and produces two-axis micrometer motions at the tip of the active arm for material compressive and shear testing. The passive force sensing arm is connected with two differential capacitive force sensors for measuring the compressive and shear forces applied to a sample. As a proof-of-concept demonstration, the MEMS microgripper is used for measure the elastic and viscoelastic properties of polydimethylsiloxane (PDMS) microcubes through both compression and shear testing. This work is an extension of a previous conference paper [27] that was only focused on the elastic testing of PDMS materials. In this journal version, we demonstrate viscoelastic material testing through implementing closed-loop force control on the microgripper; and include more technical details, experimental results, and discussions.

3.2 Device Design, Fabrication, and Calibration

3.2.1 Device Design

The MEMS microgripper, as schematically shown in Figure 3–2(a), employs two identical V-beam electrothermal actuators for orthogonally driving the left active gripping arm along x and

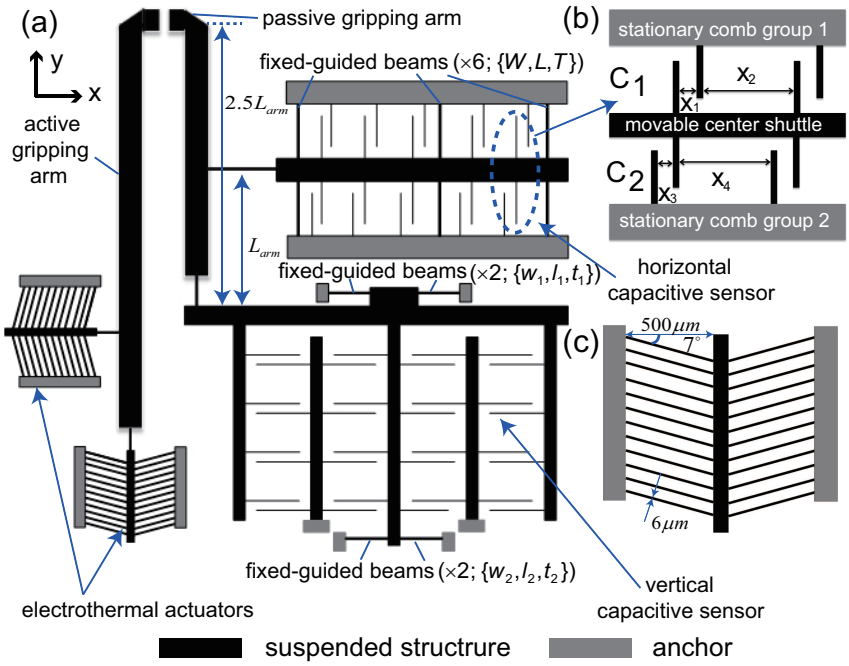

Figure 3–2: Schematic diagrams of (a) the entire microgripper, (b) the tri-plate differential capacitive force sensor, and the V-beam electrothermal actuator. (The symbols of major geometric parameters of the device are labelled, and their notations are listed in Table 3–1.)

y axes, which can compress or shear a microobject between the two gripping arms. Figure 3–2(c) shows the dimensional parameters of the two electrothermal actuators. The tips of the two gripping arms have an initial gap of 5 μm, and the electrothermal actuator along x axis can pull the left gripping arm to further open the gripping tips. The electrothermal actuator along y axis can push the left gripping arm forward and thus generate shearing motions at the tips.

In previous designs, electrostatic actuators have been widely used to drive MEMS microgrippers [22]. Limitations of the electrostatic actuators are their high actuation voltages required to generate larger displacements, relatively low force outputs ($\leq$100's μN), and large footprints. In contrast, the V-beam electrothermal actuator requires a much smaller chip area and a much lower driving voltage, and is capable of producing millinewton-level forces [18].

Two tri-plate differential capacitive sensors are connected to the right passive arm and measure forces exerted to the tip of the passive arm along x and y axes. A testing sample, placed between the tips of the two gripping arms, is characterized by driving the left tip to compress or shear

Table 3–1: Parameters of Capacitive Force Sensors

Symbol	Description	Value
	Horizontal force sensor	
W	Width of tethering beams in horizontal force sensor	8 μm
L	Length of tethering beams in horizontal force sensor	600 μm
T	Thickness of tethering beams in horizontal force sensor	25 μm
n	Number of parallel-plate pairs in horizontal force sensor	102
k_x	Stiffness of tethering beams in horizontal force sensor	60.1 N/m
l_x	Overlapping comb fingers' length in horizontal force sensor	550 μm
t_x	Comb fingers' thickness in horizontal force sensor	25 μm
	Vertical force sensor	
w_1	Width of upper tethering beams in vertical force sensor	6 μm
l_1	Length of upper tethering beams in vertical force sensor	450 μm
t_1	Thickness of upper tethering beams in vertical force sensor	25 μm
w_2	Width of bottom tethering beams in vertical force sensor	6 μm
l_2	Length of bottom tethering beams in vertical force sensor	370 μm
t_2	Thickness of bottom tethering beams in vertical force sensor	25 μm
n'	Number of parallel-plate pairs in vertical force sensor	136
k_y	Stifffness of tethering beams in vertical force sensor	56.1 N/m
l_y	Overlapping comb fingers' length in vertical force sensor	500 μm
t_y	Comb fingers' thickness in vertical force sensor	25 μm

the sample and then measuring the applied force and the resultant sample deformation. In the horizontal capacitive sensor (along x axis), a movable central shuttle is tethered by six fixed-guided beams with the same length and in-plane width. The movable central shuttle in the vertical capacitive sensor is tethered by four fixed-guided beams (two on the upper side and two on the lower side). The two groups of tethering beams in the horizontal and vertical capacitive sensors are arranged orthogonally to decouple the force sensing along x and y axes. Once a force F is applied to the right gripping tip, its horizontal and vertical components (F_x and F_y) will be transmitted to the central shuttles of the capacitive sensors and thus induce horizontal and vertical displacements (d_x and d_y) of movable comb fingers of the two sensors.

$$F_x = \frac{2k_x d_x}{5}, \quad F_y = k_y d_y \tag{3.1}$$

where k_x and k_y are the total spring constants of tethering beams in the horizontal and vertical capacitive sensors, respectively. The equation of fixed-guided beam gives

$$k_x = 6\frac{ETW^3}{L^3}, \quad k_y = 2\frac{Et_1w_1^3}{l_1^3} + 2\frac{Et_2w_2^3}{l_2^3} \tag{3.2}$$

where $E = 169$ GPa is the Young's modulus of silicon, $\{L,\ W,\ T\}$ are the length, width, and thickness of the six tethering beams in the horizontal sensor, $\{l_1,\ w_1,\ t_1\}$ and $\{l_2,\ w_2,\ t_2\}$ are the length, width, and thickness of upper and lower tethering beams in the vertical sensor, respectively.

The two capacitance values of the differential capacitive sensor can be expressed by

$$C_1 = n\frac{K\varepsilon_0 tl}{x_1} + n\frac{K\varepsilon_0 tl}{x_2}, \quad C_2 = n\frac{K\varepsilon_0 tl}{x_3} + n\frac{K\varepsilon_0 tl}{x_4} \tag{3.3}$$

where n is the number of parallel-comb pairs, K is the dielectric constant of air, ε_0 is the permittivity of free space, t ($t = t_x$ for horizontal sensor and $t = t_y$ for vertical sensor) is the out-of-plane thickness of the combs, l ($l = l_x$ for horizontal sensor and $l = l_y$ for vertical sensor) is the overlapping length of the parallel plates, and x_i ($i = 1, 2, 3, 4$) is the gap sizes between the stationary and movable combs.

The initial gaps between stationary and movable parallel combs are $x_{10} = x_{30} = d_0$ and $x_{20} = x_{40} = d_0'$. When a gripping force is transmitted to the horizontal central shuttle, the movable combs are displaced closer to stationary comb group 1 and away from stationary comb group 2 (displacement: d_x). Then, $x_1 = d_0 - d_x$, $x_2 = d_0' + d_x$, $x_3 = d_0 + d_x$, and $x_4 = d_0' - d_x$.

The differential capacitive sensor is connected to a capacitance readout chip (AD7746, Analog Devices), which converts the capacitance values C_1 and C_2 into a voltage output based on

$$V_{out-x} = V_{ref}(\frac{C_1 - C_2}{C_1 + C_2}) \tag{3.4}$$

Where V_{ref} is a preset reference voltage.

Substituting Eq. 3.3 into Eq. 3.4 and setting $d_0 << d_0'$ yield

$$V_{out-x} = V_{ref}(\frac{d_x d_0' - d_x d_0}{d_0 d_0' - d_x^2}) \cong V_{ref}\frac{d_x}{d_0} \tag{3.5}$$

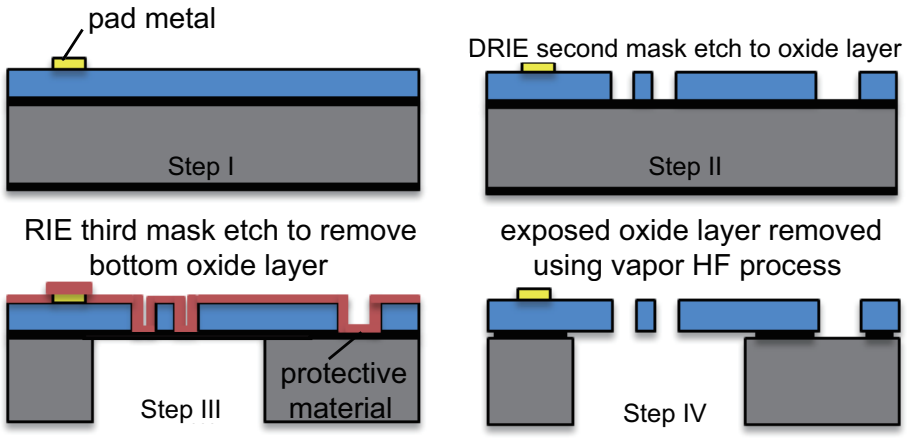

Figure 3–3: Cross-section schematic of the SOIMUMPs process for microgripper fabrication.

In order for the capacitive sensor to have a linear relationship between the output voltage V_{out-x} and the central shuttle displacement d_x (therefore the applied force F_x), it is a common practice to make the repeated comb fingers far apart (so that $d_0 << d_0'$). In our design, we set $d_0 = 5$ μm and $d_0' = 20$ μm, yielding a linearity of $\leq$1.6% in both axes (Figure 3–4). The above analysis is also applicable to designing the vertical capacitive sensor. One can readily adjust the force measurement ranges in both axes by changing the total spring constants of the tethering beams in the capacitive sensors.

3.2.2 Fabrication

The microgripper was fabricated using a silicon-on-insulator (SOI) foundry process (SOIMUMPs, MEMSCAP), as schemacally shown in Figure 3–3. Briefly, the process starts with a 150 mm Phosphorous doped SOI wafer (25 μm thick device layer). *Step 1*: Metal layers of 20 nm chromium and 500 nm gold are evaporated onto the top surface of the device layer, and patterned via lift-off to form ohmic contact pads. *Step II*: The device layer is then etched through using deep reactive ion etching (DRIE) to form the microgripper structures. *Step III*: The bottom handle layer is etched through until the buried oxide layer via DRIE, and a frontside protection material (details not released by the foundry) is used to cover the device layer during the handle layer etching. *Step IV*: After stripping the frontside protection material, a vapor hydrogen fluoride (HF)

process is used to remove the suspended area of the oxide layer to finally release the microgripper structures.

We chose the SOIMUMPs process for device prototyping in consideration of its commercial availability and high fabrication yield. However, two limitations of this process need to be noticed. One is that it cannot create a thickness step in the etched handle layer and thus does not allow electrical isolation cuts in the device layer that are mechanically connected by the handle layer [24]. Therefore, our current microgripper prototypes have electrical connections among the two electrothermal actuators and the left gripping arm, which indicates: (i) potential cross-talks between x- and y-axis actuation, and (ii) non-zero electric potential at the left gripping tip.

Regarding actuation cross-talks, we experimentally demonstrated that the cross-talks of the two actuators are negligible (Figure 3–5). The electric potential at the left gripping tip could prevent the current microgripper prototypes from operating with the two tips merged in aqueous solutions and/or being used in characterizing conductive materials. In our experiments of characterizing dielectric PDMS, no obvious effect of the electric field at the tips was observed from the force sensor data. Another limitation is that the SOIMUMPs process does not create suspended structures in the device layer sticking out of the device frame; therefore, the gripping arms of our current prototypes are enclosed in the device frame. In our experiments, we had to use a glass microneedle to feed the gripping tips with a PDMS microcube for characterization. Note that both limitations can be overcome by adopting a customized SOI microfabrication process well established in the literature [24, 22].

3.2.3 Device Calibration

3.2.3.1 Force Sensor Calibration

A flexible glass microneedle was used as a force sensor to calibrate the on-chip capacitive force sensors. The microneedle was first calibrated by a precision balance (S94790A, Fisher Scientific; resolution: 1 μN), and its spring constant and linear force sensing range were determined to be 0.31 μN/μm and 0-310 μN, respectively. The microneedle was then controlled by a motorized micromanipulator (MP-285, Sutter) to push the right gripping tip along x and y directions, during

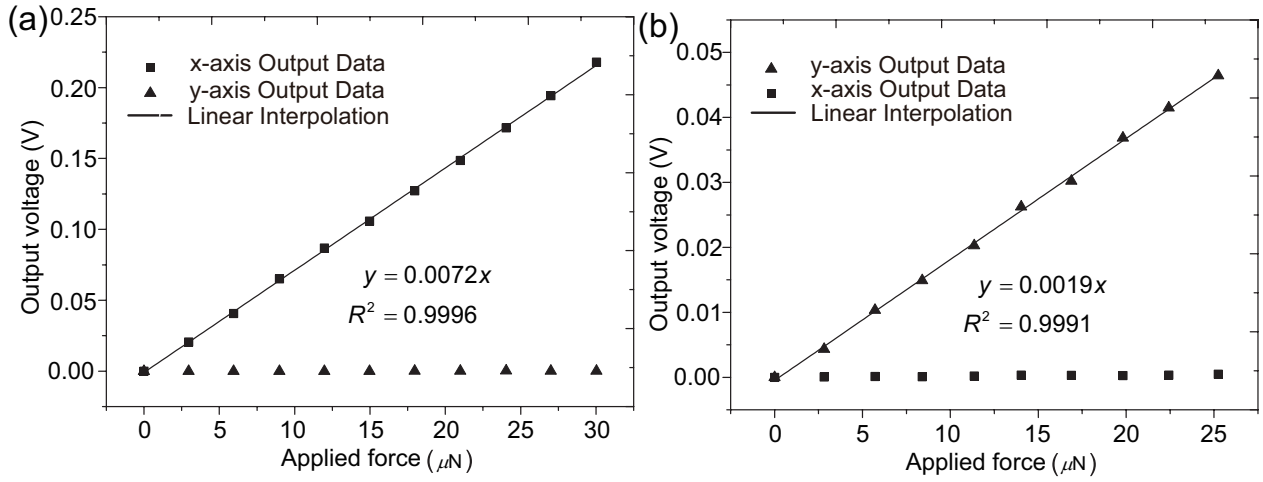

Figure 3–4: Calibration results of the (a) horizontal and (b) vertical capacitive force sensors.

which the microneedle deflection (thus the applied force) and the output voltage from the capacitive force sensor were recorded. The microneedle deflection was recorded under a stereo microscope (SZX-16, Olympus) with a 11.5× objective and a digital CMOS camera (A602cf, Basler), providing a pixel size of 2.16 μm. The recorded image frames were analyzed using a sub-pixel visual tracking algorithm (resolution: 0.08 pixel) [28] to measure the microneedle deflections. Under the current experimental setup, the force measurement resolution of the microneedle is 53 nN.

Figure 3–4 shows calibration results of the horizontal and vertical force sensors. The horizontal force sensor is capable of resolving a compressive gripping force up to 30 μN with a resolution of 7.7 nN and a linearity of 1.04%, and the vertical force sensor is capable of resolving a shear gripping force up to 25 μN with a resolution of 57.5 nN and and a linearity of 1.59%. Under the maximal force of 30 μN applied to the x-axis force sensor (voltage output: 0.218 V), the coupled force on the y-axis sensor was only 0.089 μN (corresponding to 0.17 mV). Similarly, under the maximal force of 25 μN applied to the y-axis force sensor (voltage output: 0.046 V), the coupled force on the x-axis sensor was only 0.068 μN (corresponding to 0.49 mV). The horizontal and vertical force measurement ranges can be readily adjusted by changing the total stiffness of tethering beams in each capacitive force sensor.

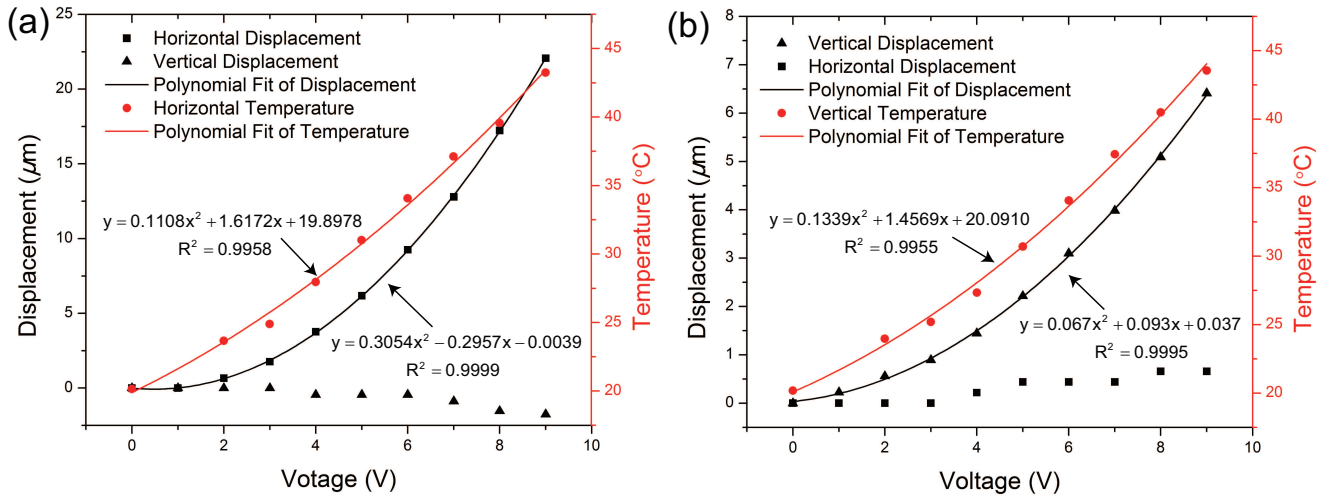

Figure 3–5: Calibration results of the displacement and temperature of the left gripping tip as a function of the voltage applied to the (a) horizontal and (b) vertical actuators.

3.2.3.2 Electrothermal Actuator Calibration

The two electrothermal actuators were characterized under a compound microscope (BX-53, Olympus) with a 20× objective and a digital camera (A602cf, Basler), and this imaging setup has a pixel size of 0.22 μm. The displacement (along x or y axes) of the left gripping tip was recorded when an actuation voltage of 0-10 V (1 V increment) was applied to the horizontal or vertical actuator. Using the sub-pixel visual tracking algorithm to process the recorded image frames, the measurement resolution of the gripping tip displacement was 17.6 nm. The calibration results are shown in Figure 3–5. In the compressive direction (x axis), the active gripping tip moved by 22.07 μm at 9 V, and, in shear direction (y axis), the tip moved by 6.41 μm at 9 V. The horizontal actuator produced larger displacements at the left gripping tip than the vertical actuator because the horizontal output displacement from the central shuttle of the horizontal actuator was further amplified by the left gripping arm (acting as a lever). Under the maximal output displacement of 22.07 μm along the x-axis, the coupled displacement along the y-axis was 1.76 μm. Under the maximal output displacement of 6.41 μm along the y-axis, the coupled displacement along the x-axis was 0.66 μm.

To investigate the Joule heating effect of the two electrothermal actuators on the left gripping tip, we measured its temperature rise as a function of the actuation voltages of both actuators. A micro-thermocouple (TJC36-CASS-010U-12m, Omega Engineering) was used to probe the left gripping tip in air when an actuation voltage was applied to a specific actuator, and the tip temperature was recorded after thermal equilibrium was reached (15 minutes after voltage application). Figure 3–5 shows the calibration data of the temperature of left gripping tip vs. the actuation voltages. One can observe that the highest temperature of the left gripping tip is 43 °C (at actuation voltage of 9 V for x or y axis). Our experimental results of PDMS characterization, to be shown in Section 3.4, demonstrate that, the measured compressive and shear moduli of the PDMS samples were not significantly altered—that is, the stress-strain curves remain linear—within the characterized strain ranges.

3.3 Materials and Methods

3.3.1 Preparation of PDMS MicroCubes

A series of PDMS microcubes (20 μm×20 μm×20 μm) were fabricated via soft lithography. Briefly, a mold with an array of 20 μm×20 μm cavities (20 μm deep) was first fabricated using AZ-40XT photoresist on a silicon wafer via standard photolithography. The uncured PDMS was then prepared from Sylgard 184 (Dow Corning) at three mixing ratios (w/w) of the base and curing agent (10:1, 15:1, and 20:1), poured to the mold, degassed in a vacuum chamber for two hours, and finally cured at 80 °C for another two hours. The cured PDMS piece was peeled off from the mold, and the microcube samples were scratched off from the molded PDMS piece using a blade. The released microcubes was inspected under microscope, and the complete ones (20 μm×20μm×20μm) were chosen for characterization experiments.

3.3.2 Experimental Setup

Figure 3–6(a) shows the experimental setup, including a MEMS microgripper bonded in a DIP-40 package, a capacitance readout circuit, an I^2C chip-computer interface (Aardvark), a microscope (SZX-16, Olympus) with a digital CMOS camera (A602cf, Basler), a glass microneedle mounted

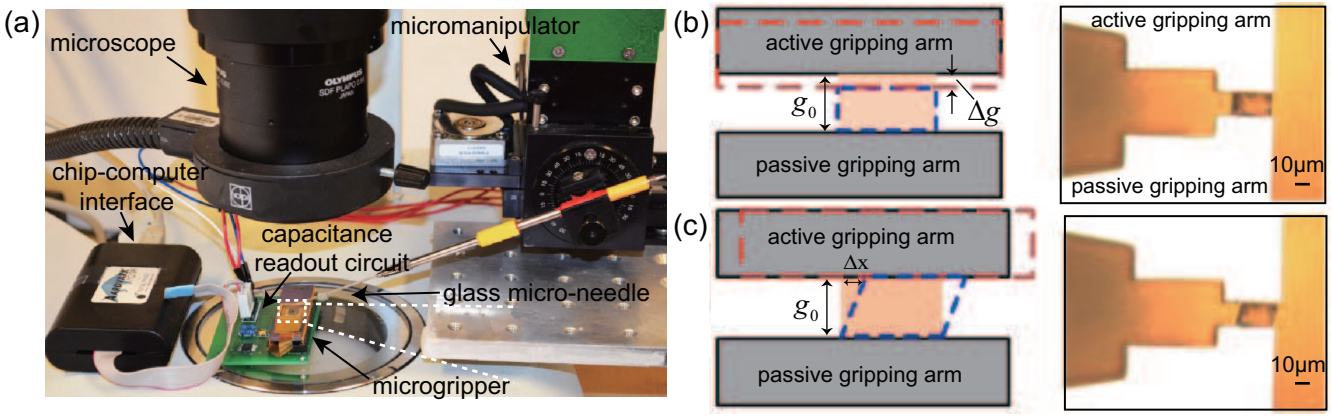

Figure 3–6: (a) Experimental setup for material compression and shear testing, inset picture shows top view of microgripper device bonded in DIP-40 package (b)(c) Schematic diagrams (left) and photographs (right) of a PDMS microcube under (b) compressive and (c) shear deformations.

on a motorized 3-DOF micromanipulator (MP-285, Sutter), and a data acquisition board (PCIe-6259, National Instruments) mounted on a host computer. The glass microneedle was used to pick up a PDMS microcube via adhesion, and place it between the two gripping tips. The microscope (11.5× objective) and the CMOS camera were used to record the images of the sample during testing, and the sub-pixel visual tracking algorithm was used to analyze the recorded images and measure deformations of the sample (resolution: 172.8 nm).

3.3.3 Compression and Shear Testing of PDMS MicroCubes

3.3.3.1 Elastic Testing

We first characterized the elastic properties of the PDMS microcubes in the compression and shear directions. For elastic testing, the active gripping arm was controlled to apply multi-step compressive or shear forces to a microcube, and the force-deformation data were obtained right after each force step was applied. Based on the measured force-deformation data, the compressive modulus of the material can be calculated by

$$E = \frac{\sigma}{\varepsilon} = \frac{\frac{F_x}{A_0}}{\frac{\triangle g}{g_0}} = \frac{F_x g_0}{A_0 \triangle g} \tag{3.6}$$

Where σ is the applied stress, ε is the resultant strain, A_0 is the original cross-section area (20 μm×20 μm) of the microcube through which the compressive force (F_x) is applied, g_0 and $\triangle g$ are

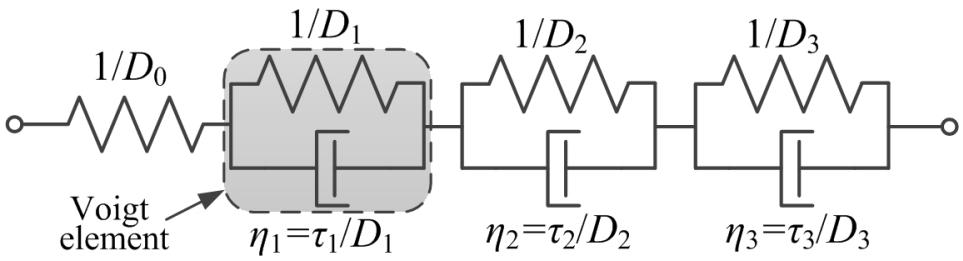

Figure 3–7: The linear viscoelastic model including a spring (which corresponds to a instantaneous creep compliance) and three Voigt elements (which corresponds to a three-term Prony series expansion) in series. η is the dashpot viscosity of the Voigt element.

the original size and the deformation of the sample along the compressive direction, respectively (Figure 3–6(b)).

The shear modulus G of the microcubes can be calculated by

$$G = \frac{\tau}{\gamma} = \frac{\frac{F_y}{A_0}}{\frac{\triangle x}{g_0}} = \frac{F_y g_0}{A_0 \triangle x} \tag{3.7}$$

where τ is shear stress, γ is shear strain, $\triangle x$ is the shear deformation of the sample (Figure 3–6(c)).

3.3.3.2 Viscoelastic Testing

For silicon-based polymers such as PDMS, it will experience a time-dependent increase in strain when subjected to a step constant stress, which is known as the viscoelastic creep. The time-varying creep strain $\varepsilon(t)$ in response to a constant stress σ is given by

$$\varepsilon(t) = D(t)\sigma \tag{3.8}$$

where $D(t)$ is the creep compliance of the material and represents the material's viscoelastic property. To maintain a constant compressive or shear stress applied to the PDMS microcubes, the compressive or shear force was regulated via closed-loop control (see Section 3.3.4). Once a constant compressive or shear stress was applied, the time-varying deformation (thus the strain $\varepsilon(t)$) of the microcube was measured at a function of time.

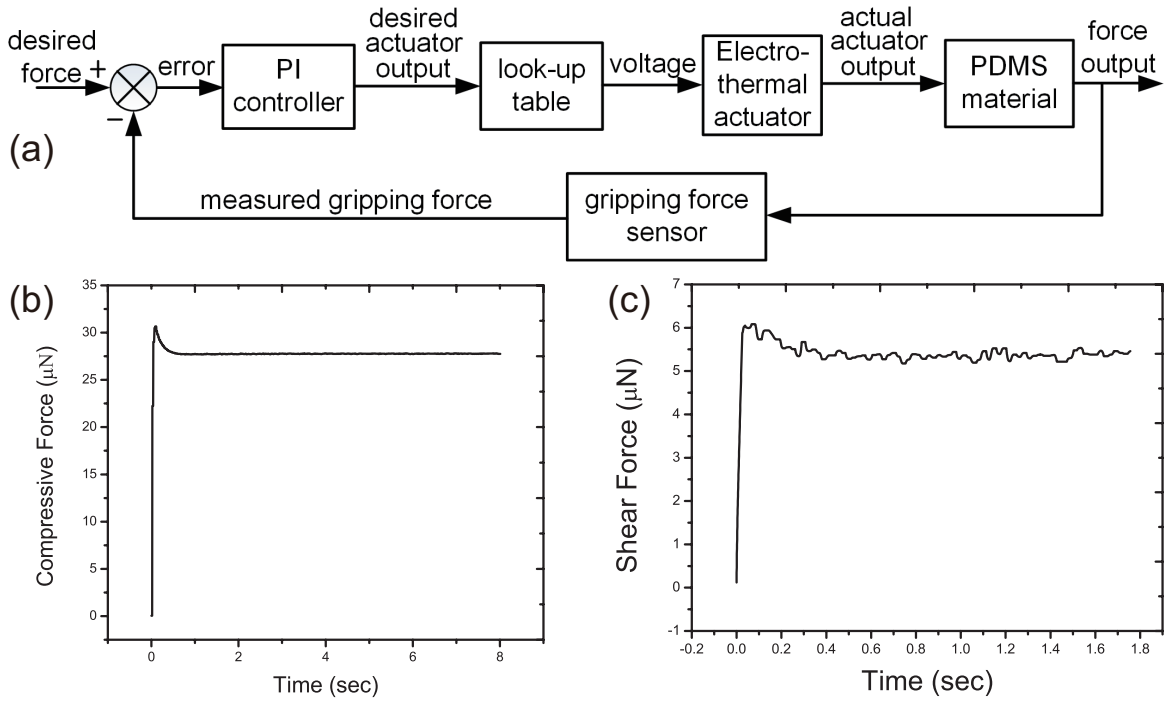

Figure 3–8: Block diagram of the closed-loop controller for regulating the compressive and shear forces during viscoelastic creep testing. (a) Control diagram (b) compressive force control (c) shear force control.

The time-varying creep compliance in the compressive (D_c) and shear directions (D_s) can be described by a linear viscoelastic model with by a Prony series expansion [29]:

$$D_c(t) = D_{0c} + \sum_{i=1}^{3} D_{ic}\left(1 - e^{-\frac{t}{\tau_{ic}}}\right) \tag{3.9}$$

$$D_s(t) = D_{0s} + \sum_{i=1}^{3} D_{is}\left(1 - e^{-\frac{t}{\tau_{is}}}\right) \tag{3.10}$$

where $\{D_{0c}, D_{0s}\}$ are the instantaneous creep compliance, $\{D_{ic}, D_{is}\}$ and $\{\tau_{ic}, \tau_{is}\}$ $(i = 1, 2, 3)$ are the compliance and retardation time constant parameters of each Prony series term, respectively, and the subscripts "$_c$" and "$_s$" indicate the compliance and time constant parameters in the compression and shear directions, respectively. Figure 3–7 shows the Prony-series viscoelastic model including a spring and three Voigt elements connected in series. Each Voigt element is described by a Prony term in Eq. 3.9 and Eq. 3.10. In this study, the compressive/shear viscoeleastic properties of the PDMS microcubes were quantified by $\{D_{0c}, D_{0s}\}$, $\{D_{ic}, D_{is}\}$, and $\{\tau_{ic}, \tau_{is}\}$.

3.3.4 Closed-Loop Force Control

A closed-loop force control system, as shown in Figure 3–8, was developed to maintain constant compressive and shear forces applied to the PDMS microcubes during the viscoelastic creep testing. The calibration results of the nonlinear electrothermal actuators (Figure 3–5) were used to generate look-up tables for system linearization. The control system used a proportional integral (PI) controller (sampling rate: 30 Hz) for both the compressive and shear force regulation.

The step responses of the force control along the compression and shear directions are shown in Figure 3–8 (b) and Figure 3–8 (c). The results of compressive force control has a setting time (error band: 5%) of 0.318 s, the overshoot is 13.52%, and the static error is 2.8% (step force value: 27 μN). For shear force control, the setting time (error band: 5%) is 0.199 s, the overshoot is 12.04%, and the static error is 5% (step force value: 5.4 μN). We also performed Matlab/Simulink simulations of the closed loop control system, and determined the closed-loop bandwidths of the control system to be 910 Hz in x-axis and 770 Hz in y-axis.

Note that using the look-up tables for linearization ignored the dynamics of the electrothermal actuators. We performed finite element simulation on the electrothermal actuators of the micro-grippers, and found that the response time of the actuator was <1 ms, which is much smaller than the system's settling time in both directions. Thus, it is reasonable to ignore the dynamics of the electrothermal actuators in the controller design.

3.4 Experimental Results and Discussion

All the material testing experiments were performed at room temperature (20-21 °C). The gap between the two gripping tips was firstly increased to 22 μm to allow a microcube to be loaded using a microneedle, and then decrease to 15 μm to preload the microcube to ensure complete contact between the side surfaces of the microcube and the side walls of gripping arms (which was verified by visual inspection prior to testing). The non-parallelism of the side walls of gripping arms, caused by the increase of the gripping arm gap during sample loading, was negligible (angle: 0.185 °). During the characterization process, no slippage between the sample and the side walls

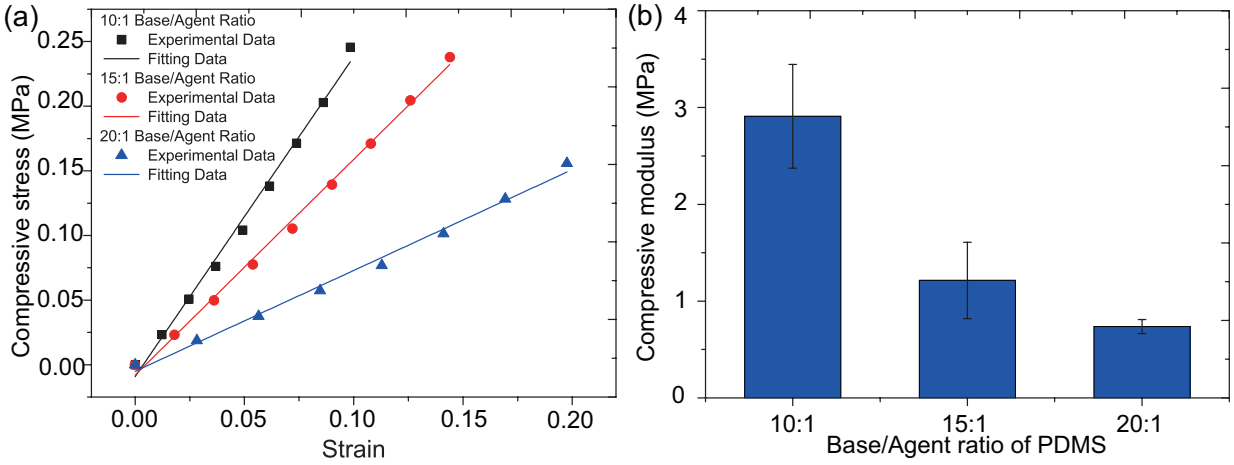

Figure 3–9: Experimental results of elastic compressive testing. (a) Typical compressive stress-strain curves and (b) extracted compressive modulus values (n=3) of PDMS microcubes.

of gripping tips was observed. Figure 3–6 (b)(c) show typical microscopic photographs of a PDMS microtube under compressive and shear deformations.

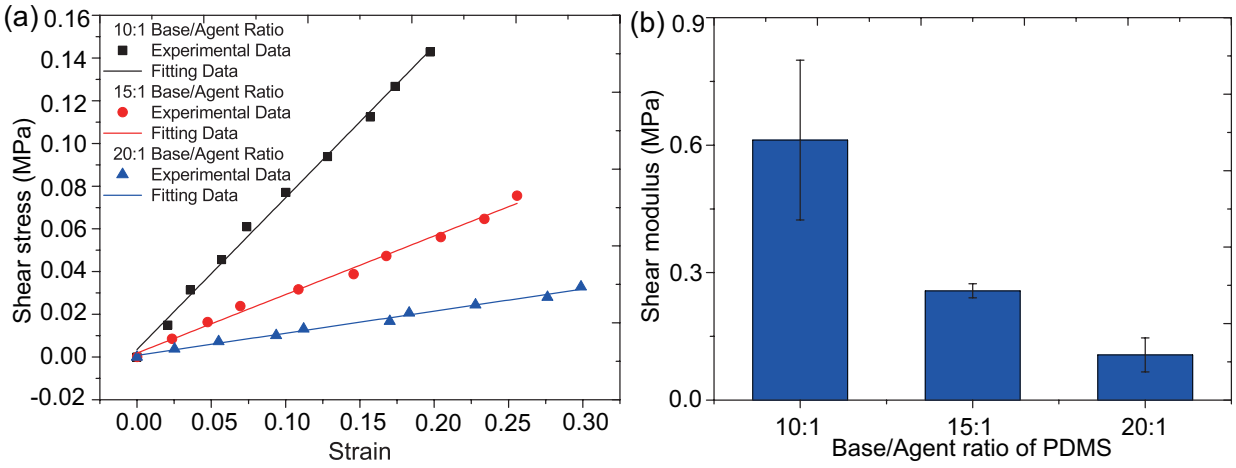

Figure 3–10: Experimental results of elastic shear testing. (a) Typical shear stress-strain curves and (b) extracted shear mudulus values (n=3) of PDMS microcubes.

3.4.1 Elastic Characterization Results

Figure 3–9(a) shows typical compressive stress-strain curves obtained from PDMS microcubes prepared at the three mixing ratios. For each mixing ratio, three microcubes were characterized. Using Eq. 3.6, their compressive moduli were calculated to be 2.91 ± 0.54 MPa (10:1 ratio; n=3), 1.21 ± 0.39 MPa (15:1 ratio; n=3), and 0.74 ± 0.07 MPa (20:1 ratio; n=3), as shown in Figure

3–9(b). Figure 3–10(a) shows typical shear stress-strain curves obtained from samples with the three mixing ratios. Using Eq. 3.7, the shear moduli were calculated to be 0.61±0.19 MPa (10:1 ratio; n=3), 0.26±0.02 MPa (10:1 ratio; n=3), and 0.11±0.04 MPa (10:1 ratio; n=3), as shown in Figure 3–10(b). These results are comparable to experimental results of the compressive/shear elastic modulus previously reported in the literature [30, 31].

From the experimental results (Figures 3–9(b) and 3–10(b)), it can be clearly noted that both compressive and shear moduli increased as the base/curing agent mixing ratio decreased. This is because, with the same amount of PDMS base, increasing the amount of curing agent yields a higher level of crosslinking in the PDMS polymer network and thus increasing the material's muduli in both compressive and shear directions.

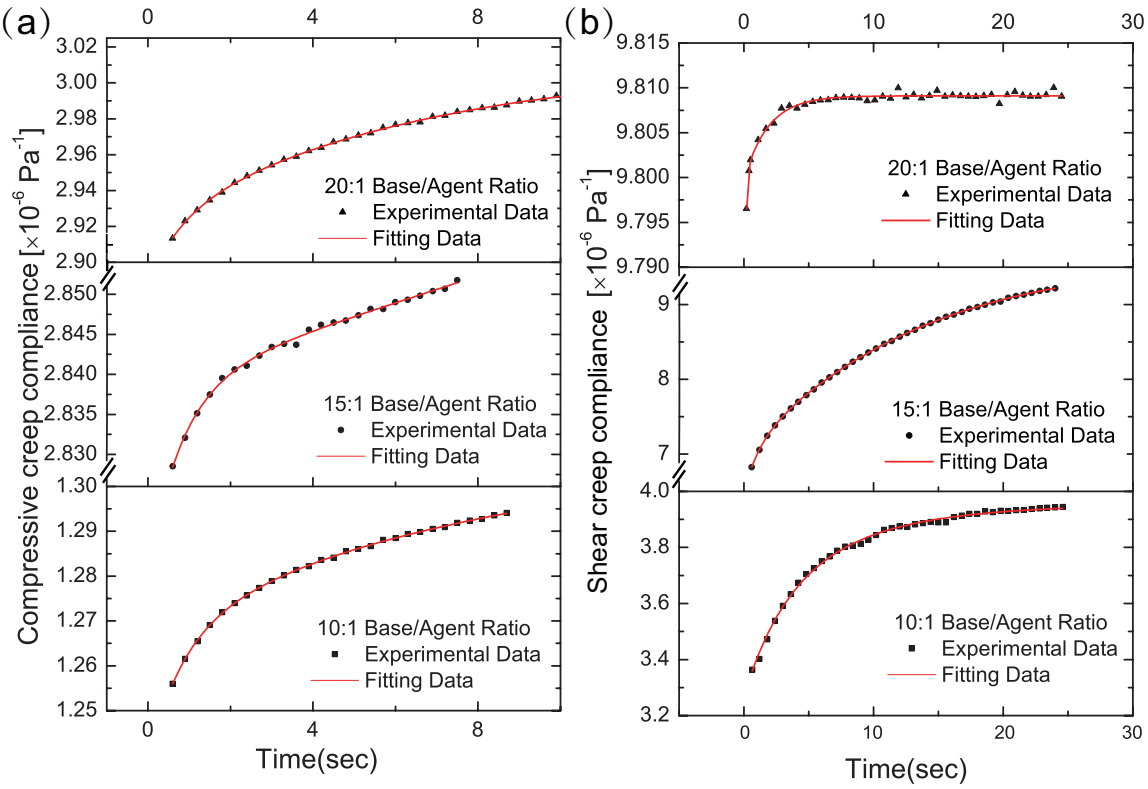

Figure 3–11: Three typical experimental curves. (a) The time-varying compressive creep compliance ($D_c(t)$ in Eq. 3.9) of PDMS microcubes at the three mixing ratio. (b) The time-varying shear creep compliance ($D_s(t)$ in Eq. 3.10) of PDMS microcubes at the three mixing ratio. The data were fitted using the Prony-series viscoelastic creep model.

Table 3–2: Experimental Results of the Viscoelastic Parameters.

Components		Order of Prony series terms 0	1	2	3	Unit
10:1	D_{ic}	1.2±0.14	0.02±0.004	0.027±0.006	0.03±0.003	MPa^{-1}
	τ_{ic}		9.28±2.29	0.99±0.18	9.38±2.26	s
15:1	D_{ic}	2.78±0.16	0.02±0.003	0.03±0.01	0.02±0.01	MPa^{-1}
	τ_{ic}		0.47±0.33	1.51±0.26	1.71±0.29	s
20:1	D_{ic}	2.88±0.21	0.03±0.007	0.08±0.07	0.07±0.04	MPa^{-1}
	τ_{ic}		1.55±0.88	3.46±2.39	4.31±1.69	s
10:1	D_{is}	2.89±0.29	0.15±0.07	0.17±0.07	0.16±0.097	MPa^{-1}
	τ_{is}		4.43±2.22	6.58±4.09	10.32±3.14	s
15:1	D_{is}	6.56±0.019	0.61±0.18	0.89±0.4	0.91±0.43	MPa^{-1}
	τ_{is}		4.28±3.13	8.14±5.21	8.13±5.19	s
20:1	D_{is}	9.70±0.31	0.03±0.02	0.006±0.003	0.03±0.02	MPa^{-1}
	τ_{is}		0.07±0.05	2.83±2.48	0.28±0.20	s

3.4.2 Viscoelastic Characterization Results

Figure 3–11 show the typical experimental data of the creep compliance of PDMS microcubes measured along the compressive and shear directions, respectively. Fitting the experimental data into the Prony-series viscoelastic model (Eqs. 3.9 and 3.10), the materials' viscoelastic parameters were extracted, as summarized in Table 3–2. Based on the experimental results of viscoelastic testing, one can clearly see that the instantaneous creep compliance, which reflects the elastic response of the material right after the stress was applied, increased (i.e., the material became softer) with the base/agent mixing ratios. This observation is in agreement with the elastic testing results.

3.4.3 Discussion

In this paper, we have developed a MEMS microgripper integrating two-axis electrothermal actuators and capacitive force sensors, and used it as an experimental platform for measuring the elastic and viscoelastic properties of soft microstructures along both compression and shear directions. Our microgripper and the associated material testing technique has several advantages.

(i) The microgripper has the capability of two-axis actuation and force sensing, which enables compression and shear testing of soft microstructures. In contrast, most of the existing MEMS microgrippers [8, 18, 22, 24, 25] are limited to one-axis actuation, and thus only can perform single-axis compression or tensile testing. (ii) Based on the devices two-axis actuation and force sensing configuration, closed-loop force control has been implemented in both axes for viscoelastic material characterization, which allowed the first experimental demonstration of viscoelastic compression/shear testing of soft micro-structures. (iii) In terms of force sensing principle, the differential capacitive force sensing mechanism used in our micrgripper design provides, in general, better measurement resolution and a wider linear range than other force sensing mechanisms (e.g., piezoresistive [32], optical [33] and vision-based [34] sensing mechanisms). Through two groups of tethering beams orthogonally arranged in the two axes, minimal measurement coupling of the two force sensors was also achieved.

We chose PDMS for demonstration of the microscale compression and shear testing. As an elastomer, PDMS has been employed for construction of wearable and stretchable biosensors [35], microfluidic chips [36], biomimetic micro- and nano-structures [37], bioMEMS sensors [6], and flexible cell-culture substrates [38], all with implications in biological and medical disciplines. The design of many of these PDMS devices require the characterization of the mateiral's mechanical property [6, 36, 38]. In addition, the experimental technique we demonstrated using the microgripper can be readily extended to testing microstructures made from other types of soft biomaterials such as hydrogels [39] and synthetic polymers [40], which has also been widely used in life science research.

Finally, we would point out three limitations of our current device prototype. (i) Because of the SOIMUMPs process we used, the device has electrical connections among the two electrothermal actuators and the left active gripping arm. Although we have experimentally confirmed the negligible cross-talk between the two electrochemical actuators, their actuation leads to a non-zero electric potential on the left gripping arm. (ii) The gripping arms of our current device are enclosed in the device frame due to the limitation of the SOIMUMPs process we used for device

prototpying. (iii) The electrothermal actuators induce a temperature rise of the left gripping arm during actuation, making the current device less suitable for characterizing temperature-sensitive materials. As pointed out in Section II-B, with the adoption of a customized SOI microfabrication process [22], the first two limitations can be readily overcome. The third limitation can be much alleviated by increasing the heat transfer on the active gripping arm (e.g., by adding heat sinks to the arm [41]).

3.5 Conclusion

This paper presents a MEMS microgripper integrating with two-axis actuators and sensors for compressive and shear testing of microscle soft materials. The device is capable of generating micrometer compressive and shear motions at its gripping tips, and measuring compressive and shear forces at nanonewton resolutions. The characterization of PDMS microcubes was demonstrated, and the obtained results of PDMS elastic and viscoelastic properties in both compressive and shear directions show good agreement with previously reported data and present reasonable trends, demonstrating the effectiveness of the microgripper as a microscale material testing platform.

References

[1] C. E. Mora-Huertas, H. Fessi, and A. Elaissari, "Polymer-based nanocapsules for drug delivery," *Int. J. Pharmaceut.*, vol. 385, no. 1–2, pp. 113–142, 2010.

[2] A. Kang, J. Park, J. Ju, G. S. Jeong, and S.-H. Lee, "Cell encapsulation via microtechnologies," *Biomaterials*, vol. 35, no. 9, pp. 2651–2663, 2014.

[3] A. Fery and R. Weinkamer, "Mechanical properties of micro- and nanocapsules: single-capsule measurements," *Polymer*, vol. 48, no. 25, pp. 7221–7235, 2007.

[4] W. Xu, R. Mezencev, B. Kim, L. Wang, J. McDonald, and T. Sulchek, "Cell stiffness is a biomarker of the metastatic potential of ovarian cancer cells," *PLoS ONE*, vol. 7, no. 10, e46609, 2012.

[5] C. Y. Y. Yip, J.-H. Chen, R. Zhao, and C. A. Simmons, "Calcification by valve interstitial cells is regulated by the stiffness of the extracellular matrix," *Arterioscler. Thromb. Vasc. Biol.*, vol. 29, no. 6, pp. 936–942, 2009.

[6] X. Liu, R. Fernandes, A. Jurisicova, R. F. Casper, and Y. Sun, "In situ mechanical characterization of mouse oocytes using a cell holding device," *Lab. Chip*, vol. 10, no. 16, pp. 2154–2161, 2010.

[7] L. Z. Yanez, J. Han, B. B. Behr, R. A. R. Pera, and D. B. Camarillo, "Human oocyte developmental potential is predicted by mechanical properties within hours after fertilization," *Nat Commun*, vol. 7, Feb. 2016.

[8] K. Kim, J. Cheng, Q. Liu, X. Y. Wu, and Y. Sun, "Investigation of mechanical properties of soft hydrogel microcapsules in relation to protein delivery using a mems force sensor," *J. Biomed. Mater. Res., Part A*, vol. 92, no. 1, pp. 103–113, 2010.

[9] R. M. Hochmuth, "Micropipette aspiration of living cells," *J. Biomech.*, vol. 33, pp. 15–22, 2000.

[10] X. Liu, Y. Wang, and Y. Sun, "Cell contour tracking and data synchronization for real-time, high-accuracy micropipette aspiration," *IEEE Trans. Autom. Sci. Eng.*, vol. 6, no. 3, pp. 536–543, 2009.

[11] R. Roy, W. Chen, L. Cong, L. A. Goodell, D. J. Foran, and J. P. Desai, "A semi-automated positioning system for contact-mode atomic force microscopy (afm)," *IEEE Trans. Autom. Sci. Eng.*, vol. 10, no. 2, pp. 462–465, 2013.

[12] J. Tan, Y. J. Chao, X. Li, and J. W. Van Zee, "Microindentation test for assessing the mechanical properties of silicone rubber exposed to a simulated polymer electrolyte membrane fuel cell environment," *J. Fuel Cell Sci. Tech.*, vol. 6, p. 041 017, 2009.

[13] Y. Zhang and C. Pan, "Measurements of mechanical properties and number of layers of graphene from nano-indentation," *Diamond Relat. Mater.*, vol. 24, pp. 1–5, 2012.

[14] R Bausch, W Möller, and E Sackmann, "Measurement of local viscoelasticity and forces in living cells by magnetic tweezers," *Biophys. J.*, vol. 76, pp. 573–579, 1999.

[15] Y. Sun, K.-T. Wan, K. P. Roberts, J. C. Bischof, and B. J. Nelson, "Mechanical property characterization of mouse zona pellucida.," *IEEE Trans. Nanobiosci.*, vol. 2, no. 4, pp. 279–286, 2003.

[16] M. Gnerlich, S. F. Perry, and S. Tatic-Lucic, "A submersible piezoresistive mems lateral force sensor for a diagnostic biomechanics platform," *Sensor. Actuat. A-Phys.*, vol. 188, pp. 111–119, 2012.

[17] X. Liu, J. Shi, Z. Zong, K.-T. Wan, and Y. Sun, "Elastic and viscoelastic characterization of mouse oocytes using micropipette indentation," *Ann. Biomed. Eng.*, vol. 40, no. 10, pp. 2122–2130, 2012.

[18] K. Kim, X. Liu, Y. Zhang, J. Cheng, X. Y. Wu, and Y. Sun, "Elastic and viscoelastic characterization of microcapsules for drug delivery using a force-feedback mems microgripper," *Biomed. Microdevices*, vol. 11, no. 2, pp. 421–427, 2009.

[19] G. F. Christopher, J. M. Yoo, N. Dagalakis, S. D. Hudson, and K. B. Migler, "Development of a mems based dynamic rheometer," *Lab. Chip*, vol. 10, no. 20, pp. 2749–2757, 2010.

[20] Y. Zhu and H. D. Espinosa, "An electromechanical material testing system for in situ electron microscopy and applications," *Proc. Natl. Acad. Sci. U.S.A.*, vol. 102, no. 41, pp. 14 503–14 508, 2005.

[21] Y. Zhang, X. Liu, C. Ru, Y. L. Zhang, L. Dong, and Y. Sun, "Piezoresistivity characterization of synthetic silicon nanowires using a mems device," *J. Microelectromech. S.*, vol. 20, no. 4, pp. 959–967, 2011.

[22] S. Muntwyler, B. E. Kratochvil, F. Beyeler, and B. J. Nelson, "Monolithically integrated two-axis microtensile tester for the mechanical characterization of microscopic samples," *J. Microelectromech. Syst.*, vol. 19, no. 5, pp. 1223–1233, 2010.

[23] C. Cao, B. Chen, T. Filleter, and Y. Sun, "Mechanical characterization of thin films using a mems device inside sem," in *2015 28th IEEE International Conference on Micro Electro Mechanical Systems (MEMS)*, 2015, pp. 381–384.

[24] K Kim, X Liu, Y Zhang, and Y Sun, "Nanonewton force-controlled manipulation of biological cells using a monolithic MEMS microgripper with two-axis force feedback," *J. Micromech. Microeng.*, vol. 18, p. 055 013, 2008.

[25] Q. Xu, "Design, Fabrication, and Testing of an MEMS Microgripper With Dual-Axis Force Sensor," *IEEE Sensors Journal*, vol. 15, no. 10, pp. 6017–6026, 2015.

[26] B. Piriyanont, A. G. Fowler, and S. O. R. Moheimani, "Force-Controlled MEMS Rotary Microgripper," *J. Microelectromech. Syst.*, vol. 24, no. 4, pp. 1164–1172, 2015.

[27] J. Qu, W. Zhang, A. Jung, S.-D. Cruz, and X. Liu, "A mems microgripper with two-axis actuators and force sensors for microscale mechanical characterization of soft materials," in *In Proc. IEEE Int. Conf. Automat. Sci. Eng. (CASE)*, 2015, pp. 1620–1625.

[28] X. Liu, J. Tong, and Y. Sun, "A millimeter-sized nanomanipulator with sub-nanometer positioning resolution and large force output," *Smart Mater. Struct.*, vol. 16, no. 5, p. 1742, 2007.

[29] I. M. Ward and J. Sweeney, *Mechanical Properties of Solid Polymers*, 3rd. Wiley, 2012.

[30] Z. Wang, A. A. Volinsky, and N. D. Gallant, "Crosslinking effect on polydimethylsiloxane elastic modulus measured by custom-built compression instrument," *J. Appl. Polym. Sci.*, vol. 131, no. 22, 2014.

[31] I. D. Johnston, D. K. McCluskey, C. K. L. Tan, and M. C. Tracey, "Mechanical characterization of bulk Sylgard 184 for microfluidics and microengineering," *J. Micromech. Microeng.*, vol. 24, p. 035 017, 2014.

[32] G. Lin, R. E. Palmer, K. S. Pister, and K. P. Roos, "Miniature heart cell force transducer system implemented in mems technology," *IEEE Trans. Biomed. Eng.*, vol. 48, no. 9, pp. 996–1006, 2001.

[33] X. Zhang, S. Zappe, R. Bernstein, O. Sahin, C.-C. Chen, M. Fish, M. Scott, and O. Solgaard, "Micromachined silicon force sensor based on diffractive optical encoders for characterization of microinjection," *Sensor. Actuat. A-Phys.*, vol. 114, no. 2?3, pp. 197 –203, 2004.

[34] X. Liu, Y. Sun, W. Wang, and B. M. Lansdorp, "Vision-based cellular force measurement using an elastic microfabricated device," *Journal of Micromechanics and Microengineering*, vol. 17, no. 7, p. 1281, 2007.

[35] H. Kudo, T. Sawada, E. Kazawa, H. Yoshida, Y. Iwasaki, and K. Mitsubayashi, "A flexible and wearable glucose sensor based on functional polymers with soft-mems techniques," *Biosensors and Bioelectronics*, vol. 22, no. 4, pp. 558 –562, 2006.

[36] M. Zhang, J. Wu, L. Wang, K. Xiao, and W. Wen, "A simple method for fabricating multi-layer pdms structures for 3d microfluidic chips," *Lab. Chip*, vol. 10, pp. 1199–1203, 2010.

[37] A. K. Epstein and J. Aizenberg, "Biomimetic nanostructured surfaces with designer mechanics and geometry for broad applications," in *MRS Proceedings*, Cambridge Univ Press, vol. 1236, 2009, 1236–SS09.

[38] R. N. Palchesko, L. Zhang, Y. Sun, and A. W. Feinberg, "Development of polydimethylsiloxane substrates with tunable elastic modulus to study cell mechanobiology in muscle and nerve," *PLoS ONE*, vol. 7, no. 12, pp. 1–13, Dec. 2012.

[39] J.-C. Kuo, H.-W. Huang, S.-W. Tung, and Y.-J. Yang, "A hydrogel-based intravascular microgripper manipulated using magnetic fields," *Sensor. Actuat. A-Phys.*, vol. 211, pp. 121 –130, 2014.

[40] J. C. Breger, C. Yoon, R. Xiao, H. R. Kwag, M. O. Wang, J. P. Fisher, T. D. Nguyen, and D. H. Gracias, "Self-folding thermo-magnetically responsive soft microgrippers," *ACS Appl. Mater. Interfaces.*, vol. 7, no. 5, pp. 3398–3405, 2015.

[41] Q. Qin and Y. Zhu, "Temperature control in thermal microactuators with applications to in-situ nanomechanical testing," *Appl. Phys. Lett.*, vol. 102, no. 1, 2013.

The connection between Chapter 3 and Chapter 4

The developed MEMS-based microgripper system reported in Chapter 3 features two-axis actuation and force sensing capabilities for microscale compressive and shear testing of soft materials, which has improved the existing limitation of one-axis actuation/sensing in MEMS-based mechanical characterization platforms. Also the on-chip compressive and shear testing of PDMS microstructures prepared at different crosslinking levels were demonstrated for the first-time to verify the effectiveness of the developed platform.

Chapter 4 will address the existing issue of large contact resistance in SEM-based *in-situ* electrical characterization process. An *in-situ* two-point electrical nanoprobing system will be developed in SEM. In order to reduce the contact resistance level during electrical characterization, a systematic investigation will be carried out on the effect of SEM chamber conditions (i.e., cleanliness level and vacuum pressure) and imaging parameters (i.e., magnification and acceleration voltage) on the contact resistance of two-point SEM-based electrical nanoprobing. Through systematically adjusting the experimental parameters, the probe-sample contact resistance is significantly reduced from the mega-ohm level to the kilo-ohm level.

Besides, the developed SEM-based *in-situ* two-point electrical nanoprobing system in Chapter 3 will be a crucial component of our multi-physical characterization system in SEM, which will be further employed for other electrical and coupling-field property characterization of nanomaterials in Chapter 5 and 6.

CHAPTER 4
Investigating the Impact of SEM Chamber Conditions and Imaging Parameters on the Contact Resistance of *In-Situ* Nanoprobing

Investigating the Impact of SEM Chamber Conditions and Imaging Parameters on the Contact Resistance of *In-Situ* Nanoprobing

Juntian Qu[1], Martin Lee[2], Michael Hilke[2] and Xinyu Liu[1]*

[1]*Department of Mechanical Engineering, McGill University, Montreal, QC H3A 0C3, Canada*

[2]*Department of Physics, McGill University, Montreal, QC H3A 0C3, Canada*

*Corresponding author: (xinyu.liu@mcgill.ca)

Published on: *IOP Nanotechnology*, vol. 28, no. 34, 345702 (11pp), 2017.

ABSTRACT: In this paper, we investigate the impact of vacuum chamber conditions (cleanliness level and vacuum pressure) and imaging parameters (magnification and acceleration voltage) of scanning electron microscopy (SEM) on the contact resistance of two-point *in-situ* nanoprobing of nanomaterials. Using two typical types of conductive nanoprobes, two-point nanoprobing is performed on silicon nanowires, during which changing trends of the nanoprobing contact resistance with the SEM chamber conditions and imaging parameters are quantified. The mechanisms underlying the experimental observations are also explained. Through systematically adjusting the experimental parameters, the probe-sample contact resistance is significantly reduced from the mega-ohm level to the kilo-ohm level. The experimental results can serve as a guideline to evaluate electrical contacts of nanoprobing and instruct how to reduce the contact resistance in SEM-based, two-point nanoprobing.

Index Terms - *In-situ* nanoprobing, contact resistance, SEM chamber conditions, SEM imaging parameters, SEM-based nanomanipulation.

4.1 Introduction

Over the past two decades, a variety of novel nanomaterials and nanostructures (e.g., 0D nanodots, 1D nanowires/tubes, 2D atomically-thin nanosheets, and 3D hierarchical nanostructures) have emerged as functional building blocks for constructing new types of electronic nanodevices [1, 2], thanks to their unique electrical properties. However, the assessment of their electrical properties is still challenging because of the technical difficulty in establishing low-resistance electrical contacts with these nanostructures [3].

There are two types of experimental methods for establishing electrical contacts with a nanostructure: (i) fabrication of metal contact electrodes, and (ii) direct electrical nanoprobing. For fabricating contact electrodes, the most common approach is through electron-beam lithography (EBL) [4]. The EBL process is costly and time-consuming, and often has relatively low yield [5, 6, 7]. In addition, the chemical treatment for electrode patterning could alter the surface properties of nanomaterials, thus introducing undesired artifacts in the measurement data of the sample's electrical properties. Alternatively, contact electrodes can also be directly "written" on a nanostructure by ion-beam-induced deposition (IBID) [3] or e-beam-induced deposition (EBID) [8], both of which decompose a gaseous precursor and form metal contact electrodes with the sample [9].

Although these direct-write methods are conceptually straightforward and generally provide higher spacial resolution than EBL [4], they still have several limitations which make them unsuitable for certain types of material characterization experiments. For instance, the IBID method employs a focused ion beam (FIB) with high energy (e.g., 30 KeV), which may alter or damage the sample surface. It has been reported that the deposition of platinum (Pt) electrodes on a silicon (Si) sample by a gallium (Ga) FIB destroyed crystallinity of the sample and converted it into amorphous Si [3, 10]. Furthermore, the highly energetic Ga ions from the FIB may also cause doping of semiconductor samples, and thus changing their electrical properties [11]. Compared with IBID, EBID is a less destructive process [11], but the composition and electrical property of EBID-deposited metal (e.g., platinum—Pt) electrodes depend on their thickness, resulting in varying electrical contact properties [11].

With the above discussions, the electrical nanoprobing technique is sometimes preferred by certain type of study that requires accurate electrical characterization of as-grown, unaltered nanomaterials [12]. This method uses conductive nanoprobes with nanometer-sized tips to directly probe a sample and establish electrical contacts [13]. For sample imaging, atomic force microscopes (AFMs) [14] or scanning electron microscopes (SEMs) are usually used. An AFM needs to first scan (for visualizing the sample and determining its position) and then probe (for establishing the electrical contact) the sample using the same AFM probe [15, 13]. This process is time-consuming and cannot perform simultaneous sample imaging and nanoprobing. In contrast, a SEM provides much faster sample imaging with nanometer resolution, which greatly facilitates the nanoprobing process [15].

For all the aforementioned methods, the contact resistance between an electrode/nanoprobe and a sample could significantly affect the measured current-voltage (I-V) data; therefore, it is highly desired to minimize the contact resistance during electrical characterization of nanomaterials. Several studies have been reported for reducing the contact resistance of metal electrodes (formed by EBL or EBID) through rapid thermal annealing [16], electric current flowing [17], and e-beam irradiation [18].

For nanoprobing, four-point measurement is a widely adopted technique to eliminate the effect of contact resistance, and has been used for quantifying electrical properties of various nanomaterials such as metallic/semiconductive nanowires [19, 20] and carbon nanotubes [21]. However, there are still experimental scenarios in which four-point probing is less feasible for electrical characterization of nanomaterials. For instance, certain types of nanomaterials (e.g., III-nitride nanorods) have relatively low aspect ratios, making it difficult to establish four-point contacts along the sample length. Additionally, to characterize as-grown nanowires vertically attached to their growth substrate, it is more convenient to conduct *in-situ* two-point nanoprobing, with one probe on top of a nanowire and the other on the growth substrate [22]. To date, few studies have been reported on experimental methods for reducing the contact resistance in SEM-based, two-point nanoprobing.

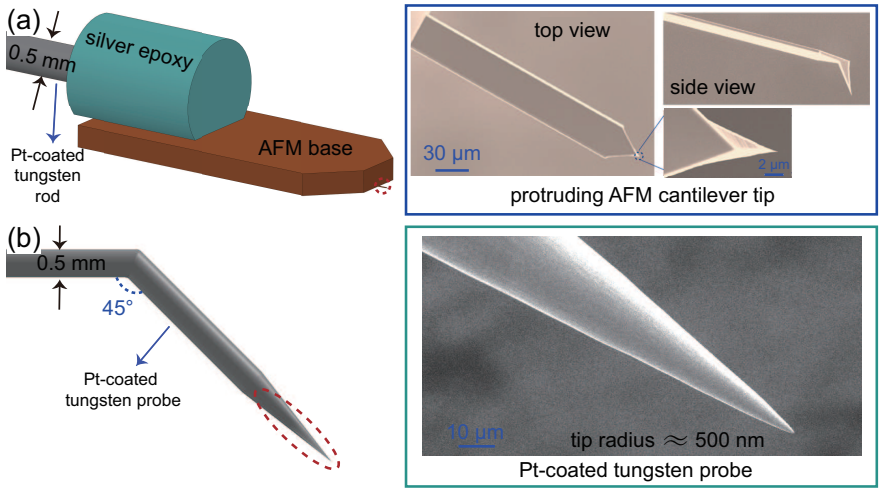

Figure 4–1: Conductive nanoprobes used in experiments. (a) An AFM nanoprobe with a protruding tip. (b) A tungsten nanoprobe. Both nanoprobes are coated with Pt through sputtering.

In this paper, we experimentally investigate the effect of SEM chamber conditions (i.e., cleanliness level and vacuum pressure) and imaging parameters (i.e., magnification and acceleration voltage) on the contact resistance of two-point nanoprobing. Using Si nanowires as a sample material, we perform *in-situ* nanoprobing using two types of conductive nanoprobes: AFM nanoprobes with protruding tips and tungsten nanoprobes, both of which are coated with Pt. We establish an experimental method to extract the probe-sample contact resistance from I-V data sets of multiple two-point nanoprobing measurements on different portions of the same Si nanowire. We quantify changing trends of the nanoprobing contact resistance with SEM chamber conditions and imaging parameters, which will serve as an experimental guideline on how to improve the electrical contacts in SEM-based nanoprobing experiments.

4.2 Experimental Methods

4.2.1 Preparation of Conductive Nanoprobes

Two types of typical conductive nanoprobes with different tip sizes were adopted in our experiments, which could be used to probe samples with different sizes. One is an AFM probe with a protruding tip (ATEC-FM, Nanosensors) of 10 nm in radius, as shown in Figure 4–1(a). The protruding tip can be directly visualized from the top view of a SEM (right of Figure 4–1(a)), which is suited for SEM-based nanoprobing. The other is a tungsten nanoprobe (ST-20-0.5, GGB

Industries) with a tip radius of 500 nm, as shown in Figure 4–1(b), which is commonly used in SEM-based nanomanipulation.

Both types of off-the-shelf commercial probes cannot be directly used for electrical nanoprobing because the AFM probe, microfabricated from single crystalline Si, has relatively low conductivity and the tungsten probe usually carries a thin layter of insulating oxide. The conductivity of the nanoprobes can be improved by coating of gold (Au), silver (Ag), or Pt [13], among which Pt coating provides excellent electrical conductivity and wear resistance. We coated a 15 nm layer of Pt on surfaces of the AFM and tungsten probes using a high-vacuum sputtering coater (EM ACE600, Leica), which provides the same group of contact materials (Pt/Si) between the two types of nanoprobes and the nanowire sample. The coated AFM probe was glued onto a Pt-coated tungsten rod (diameter: 0.5 mm; Figure 4–1(a)) via conductive silver epoxy (AA-DUCT 906, Atom Adhesives), and the tungsten rod was finally inserted into a mounting hole of the nanomanipulator for both mechanical and electrical connections. The coated tungsten probe can be directly inserted into the mounting hole of the nanomanipulator (Figure 4–1(b)).

4.2.2 SEM-based Nanomanipulation System

A SEM-based nanomanipulation system (Figure 4–2(a)) was used to perform nanoprobing experiments, which comprises: (i) a field-emission SEM (Quanta 450 FEG, FEI) for sample imaging; (ii) a four-probe piezoelectric nanomanipulator (LF-2000, Toronto Nano Instrumentation), mounted inside the SEM chamber, for driving four conductive probes for sample probing; (iii) a precision source meter (SMU 2400, Keithley) for performing I-V measurements on a sample; and (iv) a host computer for control of the nanomanipulator and the data acquisition from the source meter. The nanomanipulator includes four separate nanopositioners, each of which has a three-axis coarse positioning stage and a fine positioning stage. A unique advantage of the TNI LF-2000 over other commercial nanomanipulators is that it integrates position feedback (resolution: 0.1 nm) on each of its fine positioning stage, allowing closed-loop-controlled, high-precision nanopositioning. This feature enables accurate positioning and probing of nanowire samples in our experiments.

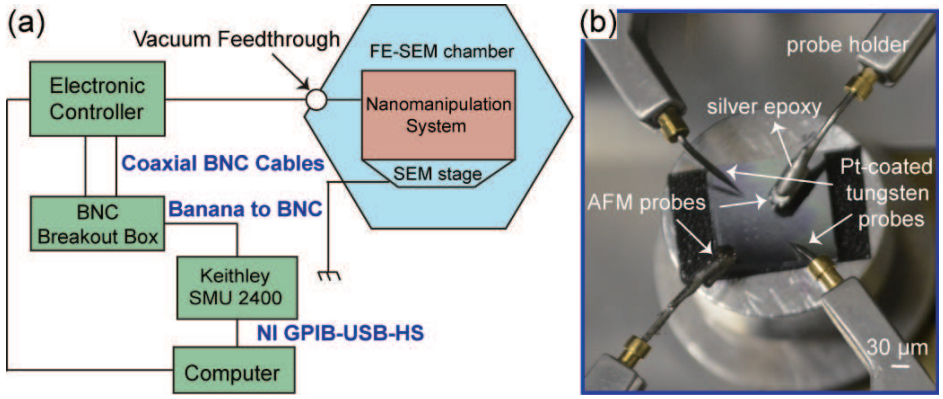

Figure 4–2: SEM-based nanomanipulation system. (a) Schematic diagram of the system setup. (b) Photograph of two AFM probes and two tungsten nanoprobes, all mounted on the nanomanipulator.

As shown in Figure 4–2(b), two AFM probes and two tungsten probes are mounted on the nanomanipulator, with the same type of probe facing each other. The electrical cables connecting the four nanoprobes are led out of the SEM chamber through a vacuum feedthrough, and finally fed into the source meter through a custom-made, noise-shielding BNC breakout box (Figure 4–2(a)).

4.2.3 Conductivity Verification of Pt-Coated Nanoprobes

To confirm the high conductivity of our Pt-coated nanoprobes, the tips of two nanoprobes of the same type were brought into contact inside the SEM chamber (Figure 4–3(a)), and the total resistance between the two cables connecting the two nanoprobes in contact was measured by the source meter. The measured resistance values (Figure 4–3(b)) from the AFM and tungsten probes were compared with that from two high-conductivity commercial nanoprobes (P-100PtIr(P), Unisoku). We found that, the total resistance between two Pt-coated tungsten probes (5.5 Ω) is comparable with that between the high-conductivity commercial nanoprobes (6.6 Ω). The measured resistance data prove the high conductivity of the Pt-coated tungsten probes. The resistance measured from two AFM probes is slightly higher (38.7 Ω) than that of the tungsten probes, which could be caused by the relatively low conductivity of the silver epoxy used for attaching the AFM probe onto the tungsten rod. To verify this, we measured the resistance of the silver epoxy connecting the AFM nanoprobe and the tungsten rod (Figure 4–1(a)) to be 15.8 Ω. Thus, the remaining resistance of the loop of the two AFM nanoprobes without the epoxy is $38.7-15.8\times2=7.1$ Ω, which

is at a similar level with that (6.6 Ω) of the high-conductivity commercial probes. Compared with the much higher resistance (in range of KΩ to MΩ) of the Si nanowires, the total resistance values of the nanoprobing setup with AFM and tungsten probes could be safely ignored in the following experiments.

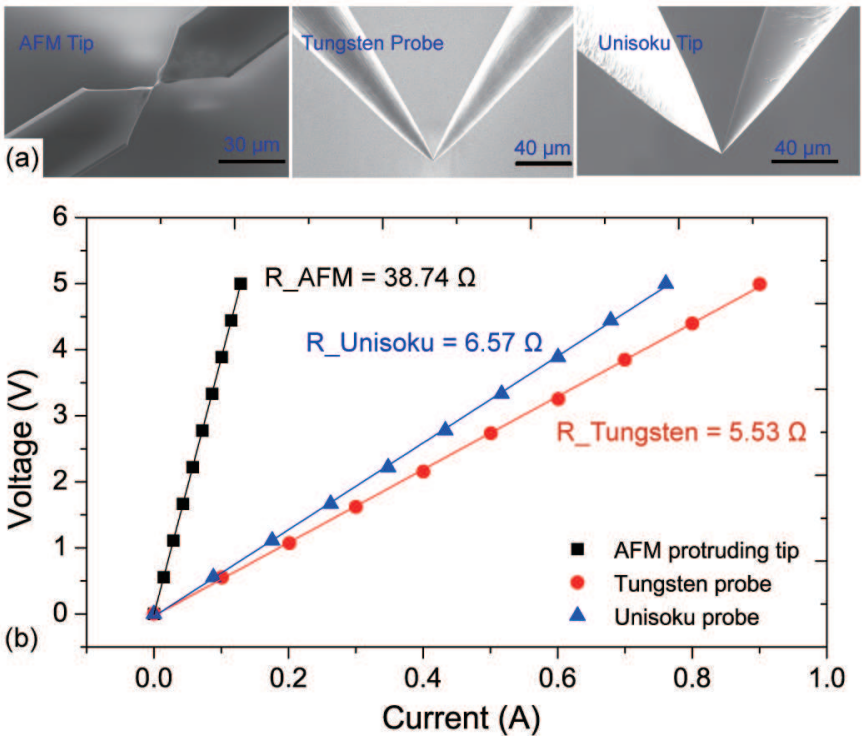

Figure 4–3: Conductivity verification of the conductive nanoprobes. (a) SEM images of nanoprobe tips in contact. (b) Experimental data of overall resistance of the measurement setup including the resistance of nanoprobe tip-tip contact and the connection cables.

4.2.4 Fabrication and Quality Assessment of Si Nanowires

We selected Si nanowires as the sample material for nanoprobing experiments. Fabrication of silicon nanowires have been well developed using both bottom-up and top-down approaches [23, 24]. The top-down approach such as EBL can predefine the dimensions and locations of Si nanowires on a substrate; therefore, we employed EBL to fabricate the Si nanowires. 200 μm-long Si nanowires were fabricated on the device layer (thickness: 220 nm) of a silicon-on-insulator (SOI) wafer through an established EBL process [25], and the detailed fabrication process is shown in Figure 4–4. 5μm and 800 nm wide nanowires were fabricated, which are probed by the tungsten

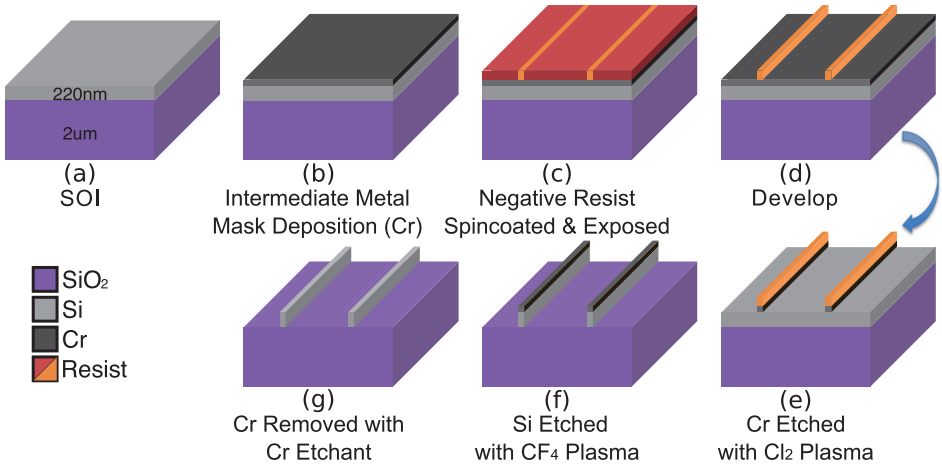

Figure 4–4: EBL fabrication process of the silicon (Si) nanowires. (a) The process starts from a piece of $1' \times 1'$ Si-on-insulator (SOI) wafer, which includes a 220 nm device layer, a 2 μm dioxide layer, and a 625 μm handle layer. (b) A thin layer of chromium (Cr) is deposited on the device layer as the intermediate metal mask. (c) High-resolution negative e-beam resist (ma-N 2400 series) is spin-coated and exposed by an e-beam writer (VB6 UHR EWF, Vistec). (d) After exposure, the resist is developed in its developer (ma-D 532) and rinsed in deionized (DI) water. (e) After drying, the wafer is inserted into an inductively-coupled-plasma reactive-ion etcher (ICP-RIE) for anisotropic dry etching of the exposed Cr metal mask using Cl_2 plasma. (f) After patterning of the Cr metal mask, the device layer undergoes ICP-RIE etching using CF_4 plasma to pattern the Si layer into nanowires. (g) Finally, the Cr mask on top of the nanowires is removed by wet etching in the Cr etchant.

and AFM nanoprobes, respectively. Figure 4–5 shows two groups of nanowires of 5 μm and 800 nm in width.

For our nanoprobing experiments, good electrical isolation between two adjacent Si nanowires is essential. To verify if the device layer of the SOI wafer has been completely etched through during nanowire patterning, we carried out element composition analysis (Figure 4–6) in the nanowires

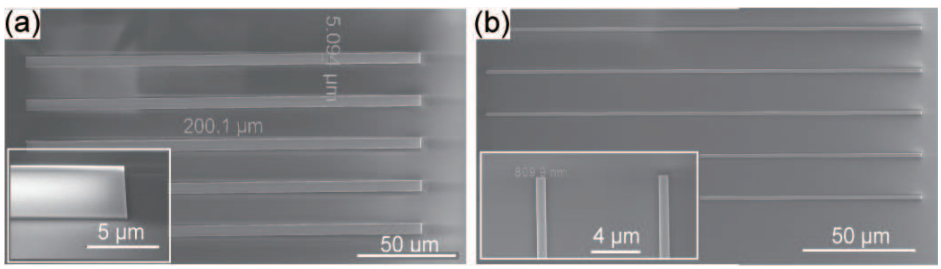

Figure 4–5: SEM photographs of (a) 5 μm and (b) 800 nm Si nanowires.

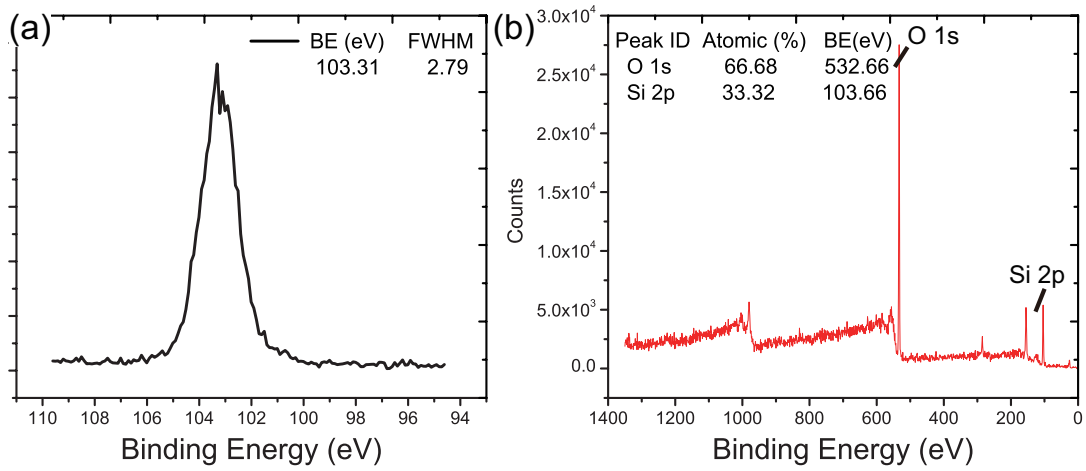

Figure 4–6: XPS element composition analysis in surrounding areas of Si nanowires. (a) High-resolution XPS spectrum in the energy range of the Si 2p signal. (b) Wide-scan spectrum showing all elements present.

surrounding areas (which is supposed to be the SiO_2 layer of the SOI wafer) using X-ray photoelectron spectroscopy–XPS (K-Alpha, Thermo Scientific), right after the EBL patterning. It was confirmed that SiO_2 (binding energy: $\sim$ 103 eV) is the sole component detected in the surrounding areas of Si nanowires and no residual single crystalline Si was detected on top of the SiO_2 layer, thus proving that adjacent nanowires are electrically isolated by the SiO_2 layer. In addition, we also performed line-scanning energy-dispersive X-ray spectroscopy (EDS) (EDAX, AMETEK) on single Si nanowires to quantify the Si element concentration along the nanowire length. The results (Figure 5–6) reveal uniform Si concentration and thus uniform conductivity along the nanowires.

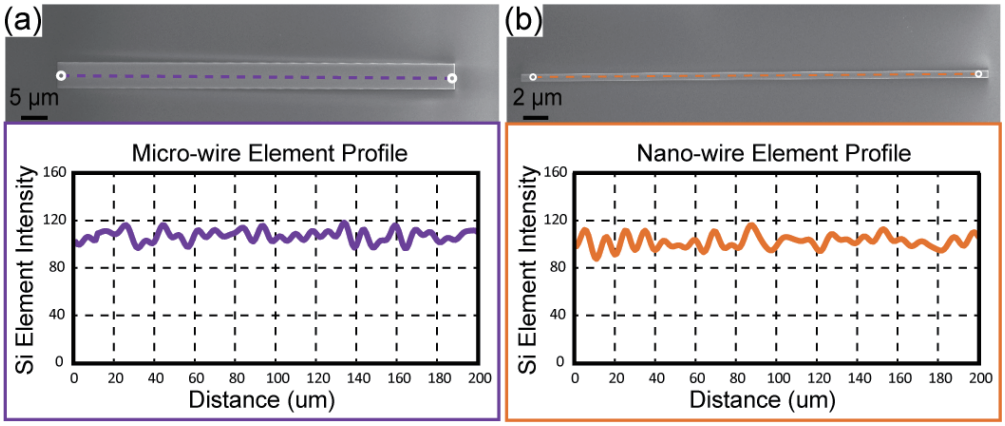

Figure 4–7: EDS element concentration analysis of (a) 5 μm and (b) 800 nm Si nanowires.

4.2.5 Nanoprobing Strategy for Contact Resistance Measurement

To experimentally quantify the nanoprobing contact resistance, the transmission-line method (TLM) was employed [26]. The TLM is a rapid, accurate, and cost-effective technique for contact resistance measurement [26], and requires simpler testing structures than the cross-bridge Kelvin resistor (CBKR) structures [27]. It assumes linear dependence of the measured resistance (between the two probes) on the probe spacing (which is true for our Si nanowires with uniform surface conductivity), and involves multiple resistance measurements (at different probe spacings) from which the contact resistance can be extracted [26]. With our experimental setup, the total resistance R_m measured by the source meter includes three components: Si nanowire resistance R_{Si}, two contact resistances $2R_c$ between the probes and the sample, and the remaining total resistance R_p of the two nanoprobes and the electrical connections in the measurement loop. Based on the resistance measurement results in Section 4.2.3, R_p (Ωs) is much lower than R_{Si} and $2R_c$ ($k\Omega$s to $M\Omega$s), and thus can be safely ignored. Therefore,

$$R_m = R_{Si} + 2R_c \tag{4.1}$$

The nanowire resistance R_{Si} can be described by:

$$R_{Si} = \frac{\rho_{Si} \cdot L}{T \cdot W} = \frac{R_S}{W} \cdot L \tag{4.2}$$

where ρ_{Si} is the resistivity of Si nanowire, T and W are the nanowire thickness and width, L is the probe spacing, and $R_s = \frac{\rho_{Si}}{T}$ is the sheet resistance of Si nanowire (which is constant in this work).

Fitting Eq. 4.2 into Eq. 4.1 yields:

$$R_m = \frac{R_S}{W} \cdot L + 2R_c \tag{4.3}$$

where the total measured resistance R_m is linearly proportional to the probe spacing L with a slope of $\frac{R_S}{W}$. If we perform multiple measurements of R_m vs. L, and the y-intercept of the fitted linear curve of R_m vs. L equals to $2R_c$.

In our experiments (Figure 4–8), we first controlled the nanomanipulator to land one of the two nanoprobes onto one end of a Si nanowire, and then employed the other nanoprobe as a "mobile electrode" to probe the nanowire at four randomly selected locations (circles in Figure 4–8) along the sample length. The "mobile-electrode" nanoprobe was first landed at the rightmost location with the largest probe spacing, and then moved towards the other probe for the subsequent three probings. At each probe spacing L, the corresponding resistance R_m was measured through I-V scanning of the probed nanowire.

Note that the contact force between the nanoprobe and the nanowire could significantly affect the contact resistance. To keep our system setup simple, we chose not to include a force sensor for quantifying the contact force. Instead, we controlled the vertical displacement of the nanomanipulator while landing a nanoprobe onto the sample to keep the contact forces relatively consistent. Specifically, we visually detected the contact of the nanoprobe with the nanowire by monitoring the starting point of the nanoprobe sliding on the sample [28], and then further lowered the nanoprobe only by 10 nm. This consistent landing operation ensures a relatively consistent level of contact force. In addition, it has been shown previously that unequally spaced contact points in the TLM provide more accurate measurement results [26], and this is the reason why the four contact points for a single nanowire (Figure 4–8) were randomly selected in our experiments. Also note that the reason why we move the "mobile-electrode" nanoprobe from the initial rightmost contact location towards the other probe (arrow directions in Figure 4–8) is to ensure we always probe on intact portions of the nanowire and thus avoid the effect of probing-induced sample damage on the measurement data.

4.3 Experimental Results and Discussion

Various experimental conditions could affect the probe-sample contact resistance during SEM-based nanoprobing. In this work, we investigate the impact of SEM chamber conditions (i.e., chamber cleanliness and vacuum pressure) and imaging parameters (i.e., magnification and acceleration voltage) on the contact resistance of Si nanowire probing. We demonstrate that the contact

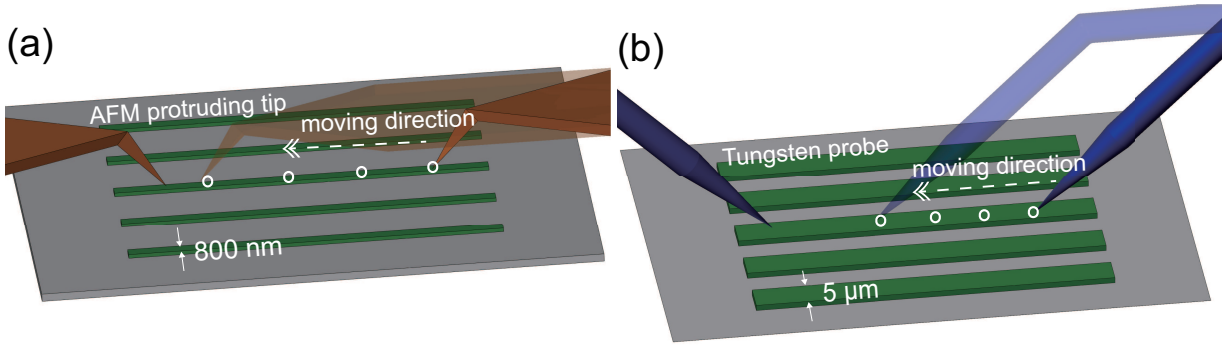

Figure 4–8: Nanoprobing strategy of Si nanowires of (a) 5 μm and (b) 800 nm width.

resistance of both types of nanoprobes on the Si nanowires can be significantly reduced through systematic adjustment of the chamber conditions and imaging parameters.

4.3.1 Impact of SEM Chamber Conditions

4.3.1.1 Chamber Cleanliness Level

Though the SEM vacuum chamber is generally claimed to be a "clean" environment, there still exist certain level of hydrocarbon (HC) residues that have not been completely removed by vacuum pumps [29]. Decomposition of the HC by the e-beam irradiation will deposit carbon contaminants on the sample surface [30], which increases the contact resistance of electrical nanoprobing.

The origin of HC contamination can be traced back to mainly three sources: the vacuum pump system, the parts inside the SEM chamber, and the sample itself. Unless the SEM pump is a dry scroll one, it cannot be neglected as a source of HC [31]. Even in many SEMs with turbomolecular pumps, a thin layer of oil can still be observed inside the SEM chamber [31]. SEM parts such as O-rings or stage lubricants can outgas carbonaceous materials into the SEM chamber, and a sample itself can also be a source of HC if it is not washed and handled properly [31].

To examine the impact of chamber cleanliness, we used a plasma cleaner mounted on the SEM to clean the chamber for 10 min, and performed nanoprobing experiments before and after the chamber cleaning (vacuum level: 7.0×10^{-4} Pa for AFM probing; and 4.65×10^{-4} Pa for tungsten probing). The SEM imaging parameters were: (i) working distance (WD): 10 mm; (ii) acceleration voltage (V_{acc}): 10 kV; and (iii) magnification: 7500×. To protect the nanomanipulation system (with mounted probes and Si nanowires) from being etched by the cleaning plasma, it was rapidly

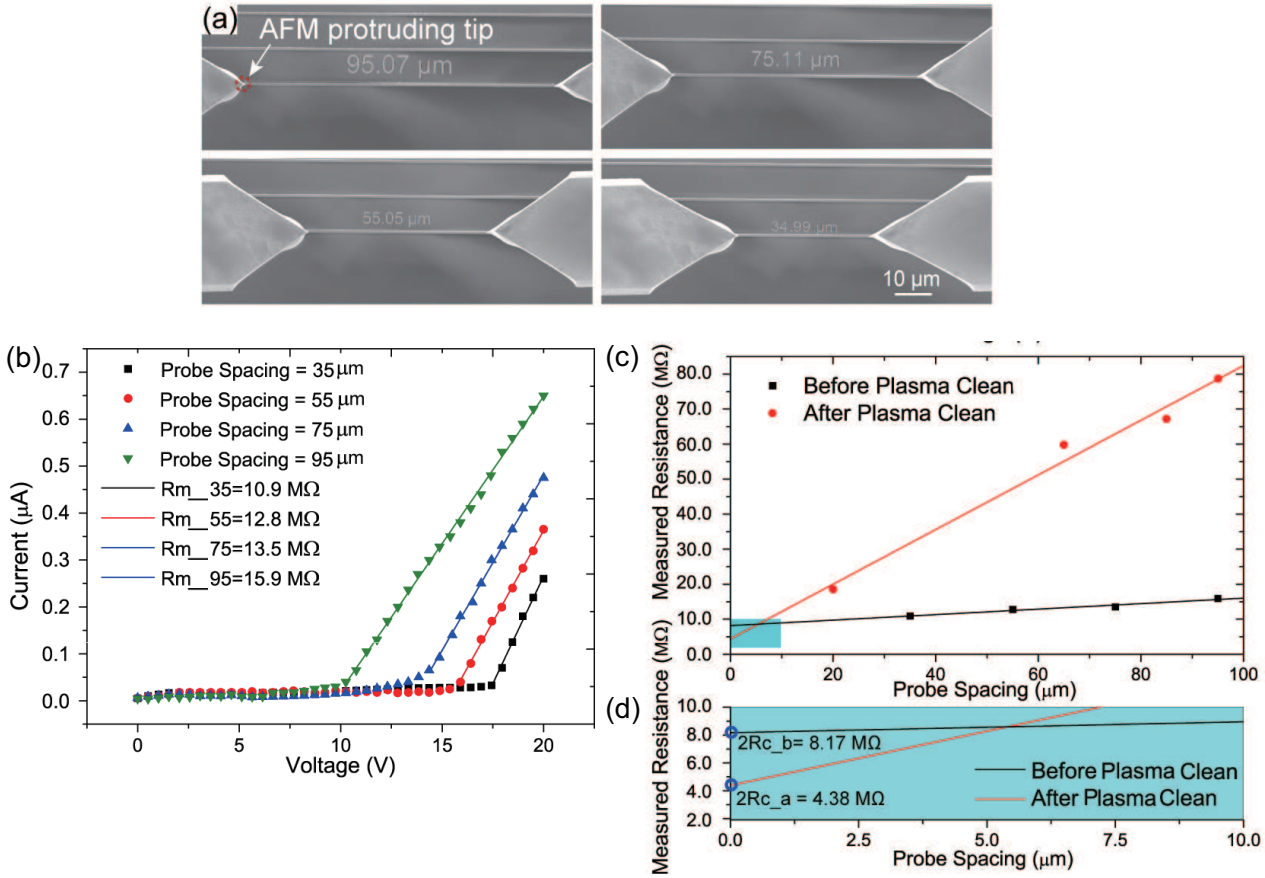

Figure 4–9: Experimental results of nanoprobing by AFM probes. (a) Image sequence of nanowire probing (top views). (b) Typical I-V curves for varying probe spacings before plasma cleaning. The linear portions of the I-V curves are fitted to extract the total resistance R_m. (c) Linear curve fitting of the total resistance (R_m) data from four measurements at different probe spacings. (d) Zoomed-in view of the y-intercepts of the linearly fitted curves in (c), which is equal to $2R_c$.

transferred into the SEM chamber right after cleaning. The entire transfer process took less than 1 min, which minimizes the chance of chamber re-contamination. We also tried to minimize the source of HC from the nanowire sample through cleaning. The sample was first rinsed with acetone and methanol to remove organic contaminants, and then treated with diluted hydrofluoric acid (1.63%) for 60 s to remove any SiO_2 on the Si nanowires.

Figures 4–9(a) and 4–10(a) show image sequences of the AFM and tungsten tips probing the 800 nm and 5 μm wide nanowires, respectively. For measuring the total resistance R_m, a voltage sweep from 0 to 20 V was applied to each probed nanowire, during which the I-V data were measured. During the resistance measurement, the e-beam was switched off using a beam blanker

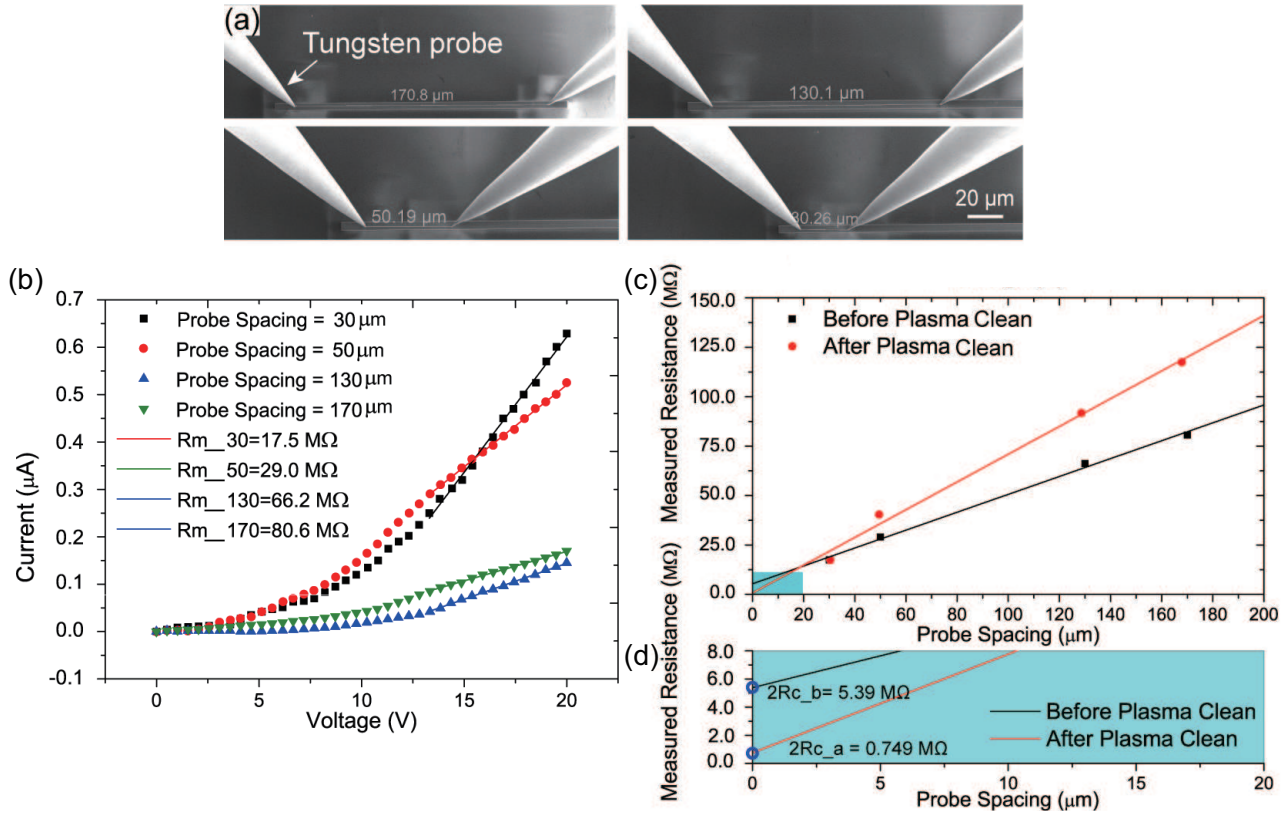

Figure 4–10: Experimental results of nanoprobing by tungsten probes. (a) Image sequence of nanowire probing (top views). (b) Typical I-V curves for varying probe spacings before plasma cleaning. The linear portions of the I-V curves are fitted to extract the total resistance R_m. (c) Linear curve fitting of the total resistance (R_m) data from four measurements at different probe spacings. (d) Zoomed-in view of the y-intercepts of the linearly fitted curves in (c), which is equal to $2R_c$.

to avoid electrical noise induced by the incident electrons. Additionally, before each measurement, the nanowire probed by the two nanoprobes were first grounded to eliminate any charge build-up on the sample caused by e-beam irradiation.

Figures 4–9(b) and 4–10(b) show the typical I-V curves measured before chamber cleaning by the AFM and tungsten nanoprobes, respectively. The nonlinear portion of each I-V curve indicates initial Schottky contacts between the nanoprobes and the nanowire, which indicates the existence of certain barrier height defined as the potential difference between the metal (probe coating) vacuum work function and the semiconductor (Si) vacuum electron affinity. Note that low-resistance ohmic contact with n-type Si (employed in our SOI wafer) relies on proper choice

of the metal material [32] (that is, the vacuum work function of the metal must be close to or smaller than the electron affinity of the Si), a high doping level of the Si [33], and high-temperature annealing of the metal-Si junction [34]. However, in our case, these conditions are not possible to achieve. Firstly, among the metal materials (Au, Ag and Pt) commonly adopted in nanoprobe coating, relatively large Schottky barrier heights exist because of larger vacuum work functions for Au (5.10-5.47 eV), Ag (4.26-4.74 eV), and Pt (5.12-5.93 eV) over the electron affinity of Si ($\sim$ 4.05 eV). We chose Pt for nanoprobe coating because of its good antioxidation nature, high electrical conductivity, and excellent wear resistance. Secondly, the lightly-doped Si device layer ($\sim 1\ \Omega \cdot cm$) of our SOI wafer does not meet the requirement of highly doping level to achieve ohmic contact. Lastly, though additional annealing step after the metal deposition on Si can improve the contact resistivity (by forming silicide-Si contact), it is not applicable to our case of nanoprobing a Si nanowire using a Pt-coated probe. Thus, the I-V data of Schottky contact are observed in Figures 4–9(b) and 4–10(b). When the sweep voltage increases to form a large forward-bias voltage at the contacts, the I-V curve becomes a straight line whose inverse slope was equal to R_m. For each nanowire, the resistance values (R_m) from four measurements (at different probe spacings) were fitted into a linear curve (Figures 4–9(c) and 4–10(c)), whose y-intercept gives $2R_c$ (Figures 4–9(d) and 4–10(d)).

For each type of nanoprobe, repeated experiments were performed on five nanowires (n = 5), and the comparison of the contact resistance values before and after plasma cleaning is shown in Figure 4–11. One can see that, after plasma cleaning, the contact resistance for the AFM probes has been reduced by 23.6%, from 2.59 $\pm$ 0.885 MΩ to 1.98 $\pm$ 0.380 MΩ. For tungsten probes, the contact resistance has been reduced by 83.5%, from 3.07 $\pm$ 0.767 MΩ to 0.507 $\pm$ 0.105 MΩ. Based on these data, we conclude that plasma cleaning can effectively reduce the contact resistance of nanoprobing. This is because SEM imaging of the nanowires inside an uncleaned chamber inevitably deposits insulating carbonaceous contaminants onto the nanowires due to the residual HC in the chamber, which causes relatively high contact resistance [35, 36].

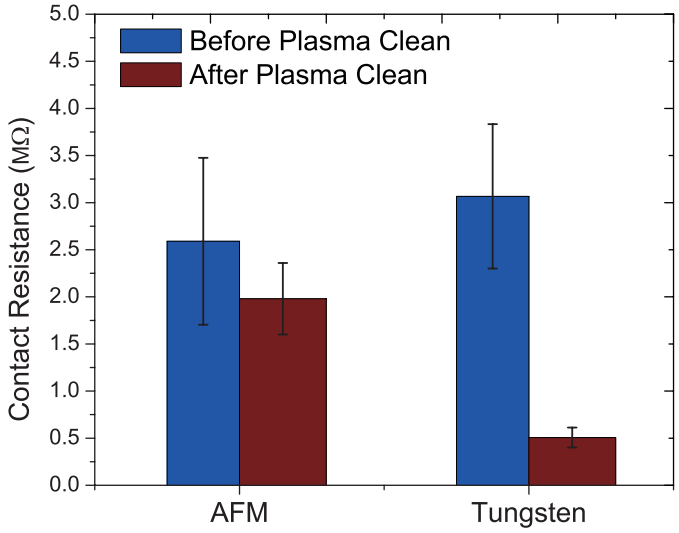

Figure 4–11: Comparison of contact resistance of the AFM and tungsten probes before and after plasma cleaning (n = 5).

4.3.1.2 Chamber Vacuum Level

The vacuum level of a SEM chamber is another critical parameter that may affect the electrical nanoprobing. The plasma cleaning method usually cannot completely eliminate the HC contamination [30]; thus, even with chamber cleaning, there still could be HC residues causing contaminant deposition on samples. In this section, we further investigate the impact of the chamber vacuum level on the contact resistance of nanoprobing.

We first plasma-cleaned the SEM chamber for 10 min, and then performed nanoprobing experiments on the Si nanowires at four different vacuum levels in the range of 10^{-3} ~10^{-4} Pa (the common vacuum range for the SEM we used). At each vacuum level, the contact resistance was measured on five nanowires (n = 5), and the same SEM imaging parameters (WD: 10 mm, V_{acc}: 10 kV, magnification: 7500×) were used for all the experiments. The quantitative relationship between the contact resistance and the chamber vacuum level is shown in Figure 4–12.

From the results, we can see that, through second-order polynomial fitting of the measured data points, the contact resistance values from AFM and tungsten probes follow a similar changing trend with the vacuum level. The contact resistance decreases with increased vacuum level, indicating that the probe-sample contact can be significantly improved when a higher vacuum level of

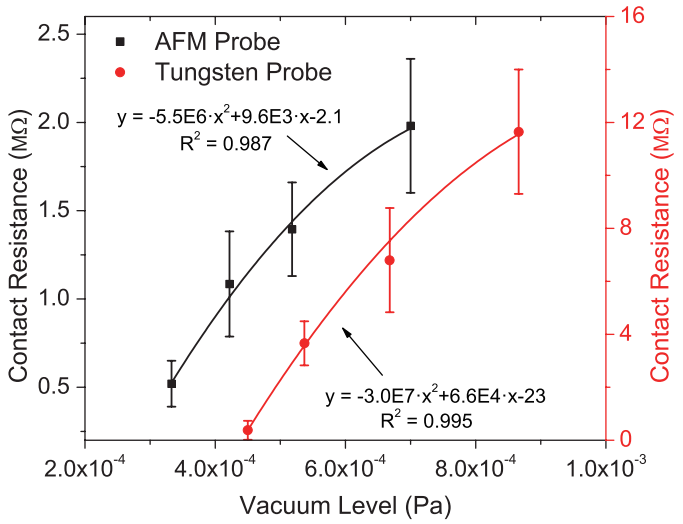

Figure 4–12: Experimental results of vacuum level impact on nanoprobing (n = 5).

the SEM chamber is reached. For tungsten probes, the contact resistance at the highest vacuum level (4.5×10^{-4} Pa) of the vacuum adjustment range is 0.377 ± 0.357 MΩ (n = 5), 96.8% lower than that (11.65 ± 2.35 MΩ, n = 5) at the lowest vacuum level (8.66×10^{-4} Pa) of the vacuum adjustment range. For AFM probes, the contact resistance at the highest vacuum level (3.33×10^{-4} Pa) of the vacuum adjustment range is 0.52 ± 0.13 MΩ (n = 5), 73.7% lower than that (1.98 ± 0.380 MΩ, n = 5) at the lowest vacuum level (7.0×10^{-4} Pa) of the vacuum adjustment range.

It has been reported that the thickness of deposited carbonaceous contaminants during SEM imaging depends on the vacuum level of the SEM chamber and a high vacuum level is always desired to mitigate the carbonaceous contamination during *in-situ* nanoprobing [35]. This explains the experimental data we observed in Figure 4–12.

Compared with the contact resistance obtained in Section 4.3.1.1 of chamber cleanliness investigation, for tungsten probes (contact resistance after plasma cleaning: 0.507 ± 0.105 MΩ at 4.65×10^{-4} Pa), the contact resistance at the highest vacuum level of 4.5×10^{-4} Pa is 25.6% further reduced; for AFM probes (contact resistance after plasma cleaning: 1.98 ± 0.380 MΩ at 7.0×10^{-4} Pa), the contact resistance at the highest vacuum level of 3.33×10^{-4} Pa is 73.7% further reduced. Through this investigation, we demonstrated that a high vacuum level of the SEM chamber could further reduce the contact resistance after the chamber is cleaned.

4.3.2 Impact of SEM Imaging Parameters

Besides the chamber conditions, SEM imaging parameters (e.g., magnification, V_{acc}, WD, and irradiation time) could also affect the electrical contacts of two-point nanoprobing, because all these parameters alter the e-beam irradiation dose (and thus energy) of the sample and thus affect the e-beam-induced deposition of carbonaceous contaminants on the sample surface. This type of contaminant deposition occurs even under a relatively high vacuum level of the SEM chamber [36]. Since the imaging magnification and V_{acc} are two common parameters a user adjusts during SEM imaging, we studied their impact on the electrical contact of two-point nanoprobing. For the irradiation time, it is well accepted that it should be kept as short as possible during nanoprobing to minimize the irradiation-induced sample damage and HC deposition. Thus, in our experiments, we kept an approximately constant irradiation time of ∼5 min, which is the shortest time a proficient user takes to establish the probe-sample contacts using our SEM setup. The WD is usually kept fixed for a SEM and rarely adjusted by a user. Thus, we fixed it to be 10 mm.

4.3.2.1 Imaging Magnification

For our SEM (Quanta 450 FEG, FEI), the magnification commonly used for SEM nanoprobing ranges from 5500× to 11000×, and the corresponding e-beam spot size number is adjusted from 3.5 to 2.0 accordingly. The magnification and its associated spot size number mainly determine the electron dose of the e-beam delivered to a nanowire sample, and thus affect the amount of HC contaminant deposited to the sample. To our best knowledge, no previous study is reported on experimentally examining the impact of imaging magnification on the contact resistance of nanoprobing.

We performed nanoprobing experiments on the Si nanowires through SEM imaging at four different magnifications (5500×, 7500×, 9500×, and 11000×), and the corresponding e-beam spot size numbers were 3.5, 3.0, 2.5, and 2.0, respectively. The adjustment of the e-beam spot size based on the imaging magnification is necessary to ensure sharp SEM vision (without blurring) at different magnifications. Other imaging parameters remained constant in the experiments: WD = 10 mm and V_{acc} = 10 kV. For each I-V measurement, we firstly probed a nanowire under the

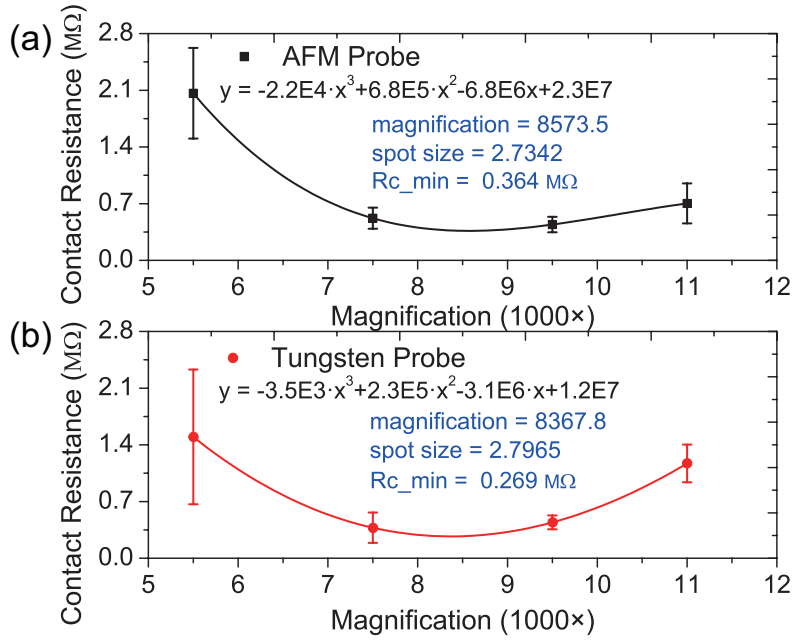

Figure 4–13: Experimental results of nanoprobing contact resistance vs. imaging magnification (n = 5), by using (a) AFM and (b) tungsten probes.

guidance of SEM vision (at a specific magnification), then switched off the e-beam, and connected the two probes contacting the sample to the electrical ground to minimize the charge build-up on the sample. Finally, the I-V curve was measured. The TLM was used to extract the contact resistance from four I-V data sets obtained at different probe spacings. At each magnification, the contact resistance was measured on five nanowires (n = 5), and the quantitative relationship between the contact resistance and the magnification is shown in Figure 4–13.

The contact resistance data, from the AFM and tungsten probes, were fitted by third-order polynomial equations with satisfactory coefficients of determination. The fitted curves of the contact resistance show a similar changing trend with the magnification, and reach their minima at medium levels of magnification. Based on the equations of fitted curves, the lowest contact resistance values are found to be: (i) 0.364 MΩ (magnification: 8574×; spot size: 2.73) for AFM probes; and (ii) 0.269 MΩ (magnification: 8368×; spot size: 2.80) for tungsten probes.

From the data in Figure 4–13, one can observe that, within the range of 5500× to 11000×, too high and too low magnifications both increased the contact resistance. This was caused by the

combinatorial effect of the imaging magnification and its associated spot size number. Note that, when the imaging parameters are adjusted, an increase in imaging magnification is associated with a decrease in the e-beam spot size. A higher magnification leads to a smaller area of the sample surface to be scanned by the e-beam, but its associated smaller e-beam spot size number also reduces the total amount of electrons delivered to the scan area of the sample in each scan cycle (which equivalently reduces the total e-beam energy delivered to the sample). Thus, the electron dose delivered to the scan area of the sample during each scan cycle, defined as the amount of electrons per unit scan area, could be high when the magnification is at its low or high end of the range of 5500×—11000× (when the contribution of the electron amount or the scan area dominates, respectively). It is known that the amount of HC deposition to the sample is proportional to the energy per unit area (proportional to the electron dose) delivered during e-beam scanning [37]; thus, it is well-reasoned that the amount of HC deposition is also proportional to the electron dose delivered to the sample during scanning. This explains the observed changing trend of the contact resistance in Figure 4–13.

To further explain the experimental data, we performed EDS analysis of the carbon concentration (and thus the HC concentration) on the nanowire surface after each nanoprobing experiment. As shown in Figure 4–14 and Figure 4–15, the measurement curves of carbon concentration well correlate with those of the contact resistance. These data further verify that the change in contact resistance was caused by the change in the amount of HC deposition during SEM imaging.

Through this investigation, we conclude that the imaging magnification and its associated spot size number have a combinatorial effect on the contact resistance of the nanoprobing and a low level of contact resistance can be achieved by adopting a medium level of magnification. Based on the fitted curves of our measurement data, one can see that, compared with the minimal contact resistance values (AFM: 0.52 MΩ, Tungsten: 0.377 MΩ) we have achieved while investigating the vacuum level impact, the contact resistance can be further reduced to as low as 0.364 MΩ (magnification: 8574×; spot size: 2.73) for AFM probes and 0.269 MΩ (magnification: 8368×; spot size: 2.80) for tungsten probes.

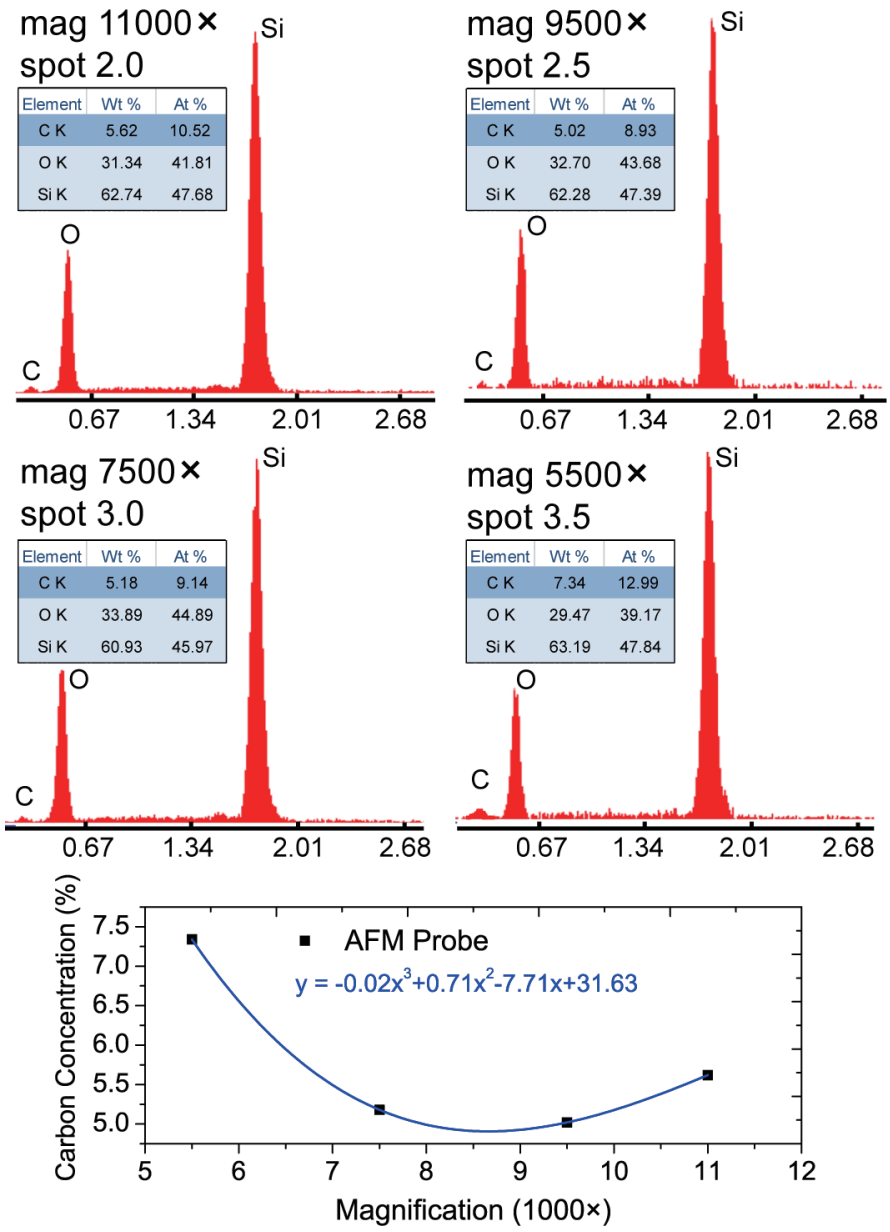

Figure 4–14: Energy-dispersive X-ray spectroscopy (EDS) analysis of carbon element concentration on 800 nm nanowires nanoprobed by the AFM probes at different magnifications. Due to the relatively large penetration depth (e.g. ~ 2 μm at 10 kV) during EDS measurement and the thin Si nanowires (220 nm in height), the relatively high intensity of Si and oxygen elements mainly derive from the EDS signal component from the SiO_2 layer underneath the Si nanowire).

4.3.2.2 Acceleration Voltage

After investigating the impact of imaging magnification, the optimal imaging magnifications of 8574× (beam spot size: 2.73) for AFM probes and 8368× (beam spot size: 2.80) for tungsten

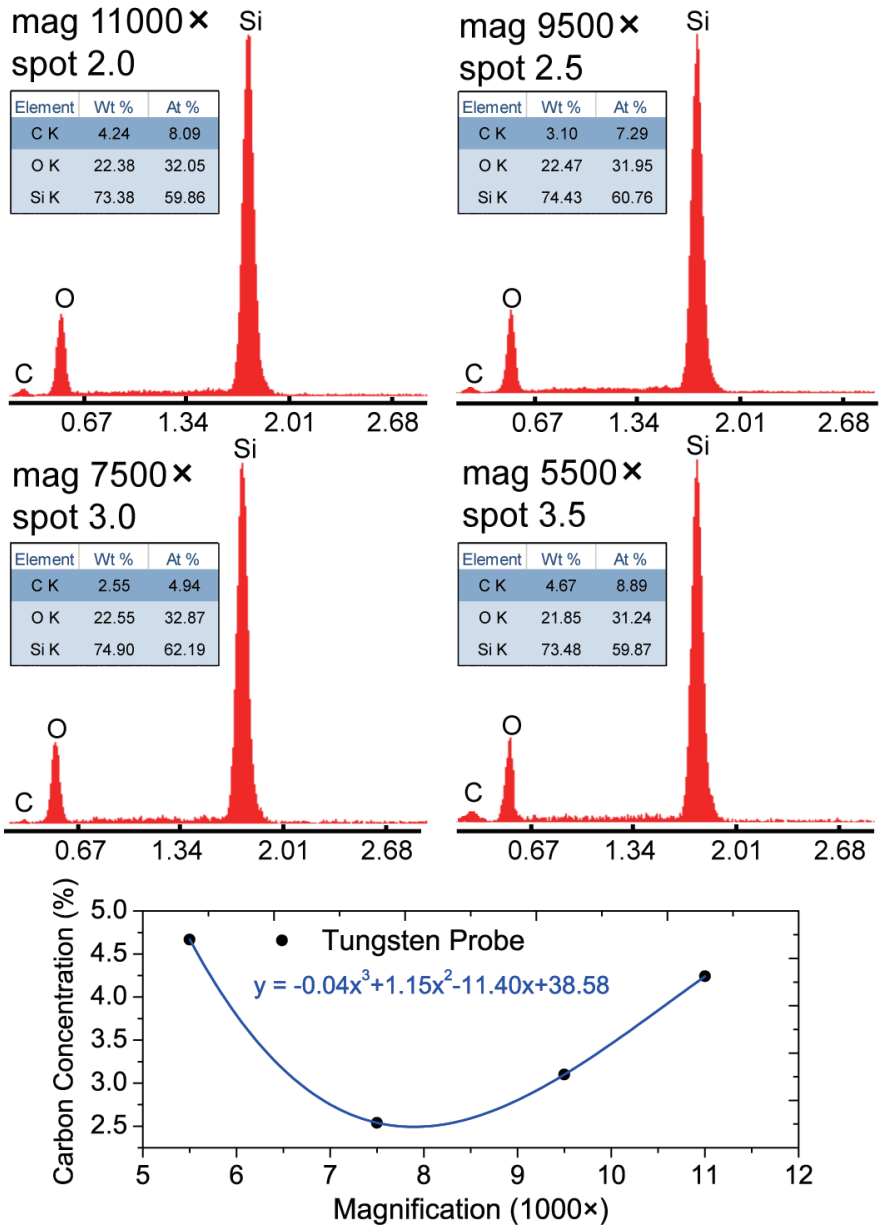

Figure 4–15: EDS analysis of carbon element concentration on 5 μm nanowires nanoprobed by the tungsten probes at different magnifications. Due to the relatively large penetration depth (e.g. $\sim$ 2 μm at 10 kV) during EDS measurement and the thin Si nanowires (220 nm in height), the relatively high intensity of Si and oxygen elements mainly derive from the EDS signal component from the SiO_2 layer underneath the Si nanowire).

probes were used for experiments probing the impact of the acceleration voltage V_{acc} on the contact resistance. We performed nanoprobing experiments on the Si nanowires at three different acceleration voltages of 2kV, 5kV, and 7kV. At each voltage, the contact resistance was measured on five

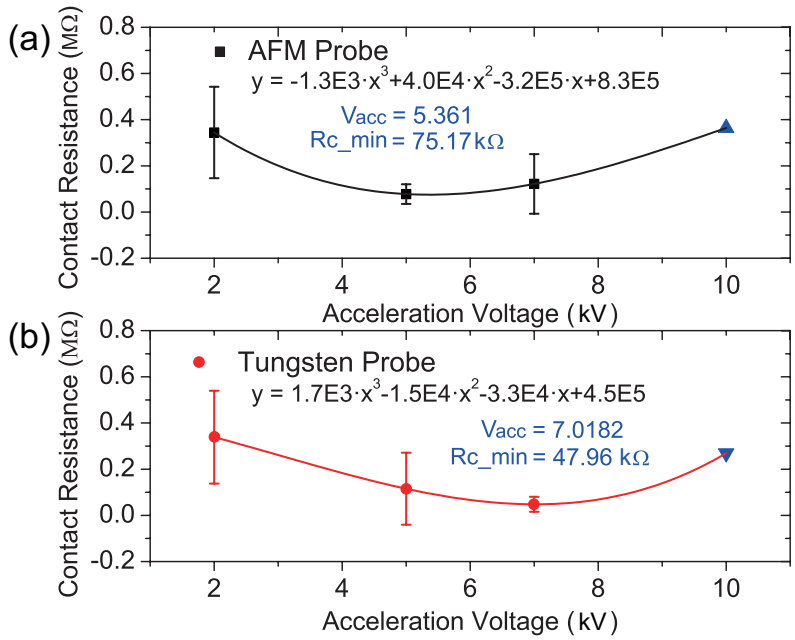

Figure 4–16: Experimental results of the contact resistance vs. acceleration voltage (n = 5), by using (a) AFM and (b) tungsten probes. The blue triangles indicate the minimum values of contact resistance obtained from the investigation of the imaging magnification impact.

nanowires (n = 5). The quantitative relationship between the contact resistance and acceleration voltage is shown in Figure 4–16, which also includes the contact resistance values at 10 kV (blue triangles) that were obtained in Section 4.3.2.1 (fitted from Figure 4–13).

The experimental results in Figure 4–16 show that the contact resistance data from both the AFM and tungsten probes follow a similar trend with the acceleration voltage. In the range of 2–10 kV, the contact resistance was high at both the low and high ends of the voltage range, and reached its minimum at a medium level of the acceleration voltage. Through third-order polynomial fitting of the contact resistance data, we found the minimum values of the contact resistance to be: (i) 75.17 KΩ at 5.361 kV for AFM probes, and (ii) 47.96 KΩ at 7.018 kV for tungsten probes, which are 79.4% and 85.9% lower than the highest values in the two contact resistance curves (0.364 MΩ at 10 kV for AFM probes, and 0.339 MΩ at 2 kV for tungsten probes), respectively. Besides, compared with the minimum values of contact resistance (AFM: 0.364 MΩ, tungsten: 0.269 MΩ) we have achieved after the investigation of the imaging magnification impact, the contact resistance has been further reduced by 79.4% and 82.2%, respectively.

The observed trend of the contact resistance as a function of the acceleration voltage, which reflects the deposition level of the HC, can be attributed to the combinatorial effect of the dissociation reaction rate and the deposition rate of HC inside the SEM chamber. A previous theoretical study has shown that low-energy electrons induce a higher rate of the dissociation reaction that generates HC since their energy matches the peak of dissociation cross-section energy of the precursor molecules [38]. On the other hand, the e-beam induced deposition of HC on a sample is a dynamic process, during which the HC molecules arrive at and leave the sample surface simultaneously. It has been demonstrated that the rate of HC deposition primarily depends on the electron dose (which is determined by the period of time the e-beam dwells on the sample and the e-beam current) [36]. Thus, with a fixed scanning time per image frame, a higher acceleration voltage generates a higher e-beam current and thus a higher electron dose, leading to a higher deposition rate of the HC on the sample surface. As the amount of HC deposition depends on both the dissociation reaction and the deposition rate of the HC, the combinatorial effect of these two rates could explain the observed changing trend of the contact resistance we measured, as shown in Figure 4–16.

To further support the measurement data of contact resistance, we performed EDS analysis (Figure 4–17 and Figure 4–18) of the carbon element concentration on the samples that were nanoprobed under different acceleration voltages. For the EDS analysis, we employed a constant acceleration voltage of 5 kV and a relatively short analysis period of 30 s. Since the period of time for EDS analysis is much shorter than that (5 min) for nanoprobing, the additional HC deposition occurring during the EDS analysis can be safely ignored. From Figure S5 & S6, we can see that the carbon element concentrations on different samples show similar trends to those of the measured contact resistance data in Figure 4–16, further validating our experimental observations of the contact resistance as a function of the acceleration voltage.

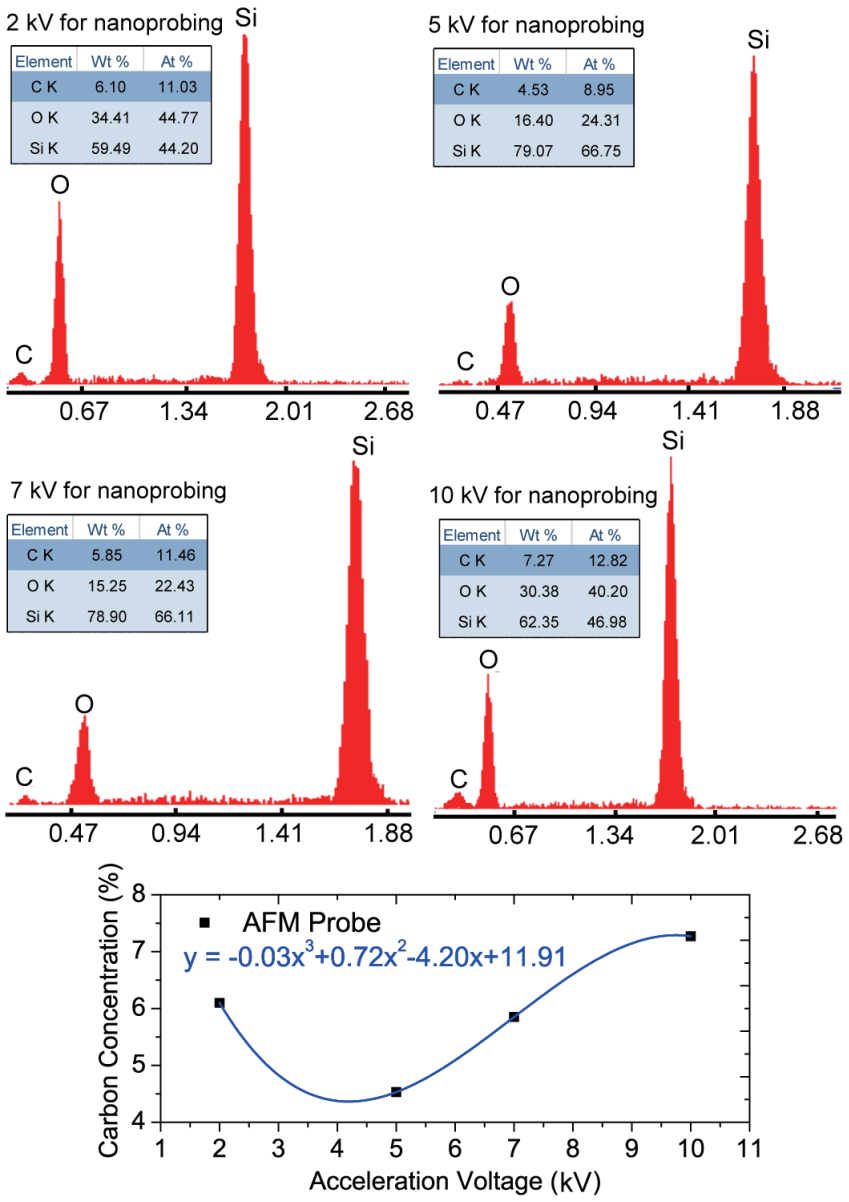

Figure 4–17: EDS analysis of carbon element concentration on 800 nm nanowires nanoprobed by the AFM probes at different acceleration voltages. Due to the relatively large penetration depth (e.g. $\sim 2\ \mu$m at 10 kV) during EDS measurement and the thin Si nanowires (220 nm in height), the relatively high intensity of Si and oxygen elements mainly derive from the EDS signal component from the SiO_2 layer underneath the Si nanowire).

4.3.3 Discussion

In this work, we performed a systematic investigation of the impact of the SEM chamber conditions and imaging parameters on the contact resistance of electrical nanoprobing. The two-point *in-situ* nanoprobing method adopted in this work can avoid potential modification of sample's

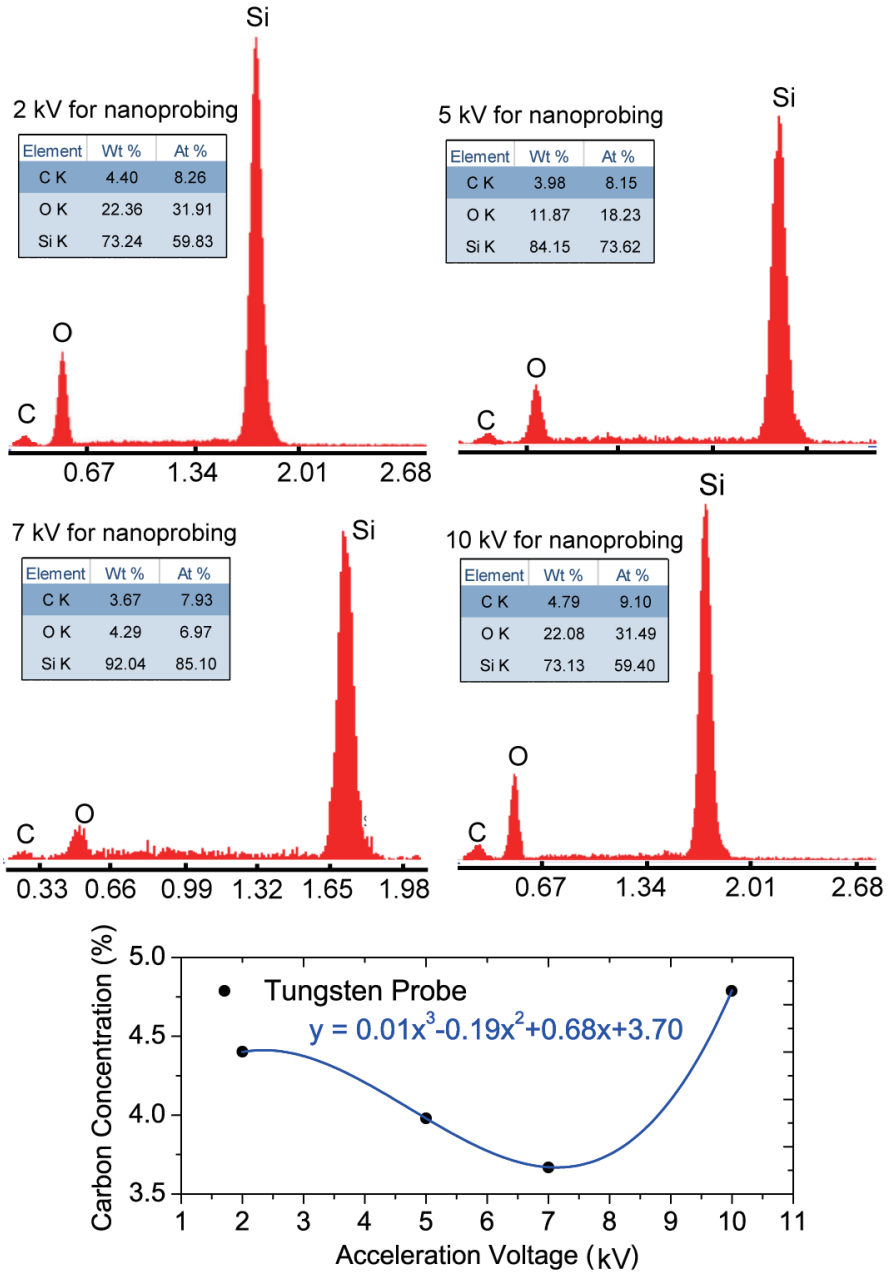

Figure 4–18: EDS analysis of carbon element concentration on 5 μm nanowires nanoprobed by the tungsten probes at different acceleration voltages. Due to the relatively large penetration depth (e.g. ~ 2 μm at 10 kV) during EDS measurement and the thin Si nanowires (220 nm in height), the relatively high intensity of Si and oxygen elements mainly derive from the EDS signal component from the SiO_2 layer underneath the Si nanowire).

electrical properties that may be caused by other methods involving electrode contacts enabled by EBL, IBID, or EBID. In addition, the nanoprobing method allows the the electrical contacts

to be established, removed, and re-established at different portions of a nanometer-sized sample, providing high flexibility for electrical characterization of nanomaterials. It could serve as an alternative method to four-point nanoprobing, for testing low-aspect-ratio nanostructures or as-grown nanomaterials for which four-point probing becomes technically challenging.

The experimental results we obtained in this work could serve as a guidance for experimentalists to evaluate and improve the electrical contacts of SEM-based two-point nanoprobing. Note that, as the specific experimental conditions may vary with different system setups, readers are suggested to refer to the experimental methodology presented in this work rather than the contact resistance values that are specific for our experimental setup. In addition, in order to make the proposed experimental method easy to realize and practical for use by common practitioners, we decided not to integrate a micro force sensor in our system for quantifying the contact force. Instead, we controlled the contact force of nanoprobing to be relatively constant by ensuring consistent vertical displacements of the AFM and tungsten probes. If the contact force needs to be quantified in a specific experiment, it is feasible to integrate a micro force sensor (e.g., a piezoresistive self-sensing AFM cantilever) with the nanoprobe, to quantify/control the contact force and examine its effect on the probe-sample contact resistance.

4.4 Conclusion

This paper reported the experimental investigation of the impact of SEM chamber conditions (cleanliness level and vacuum pressure) and imaging parameters (magnification and acceleration voltage) on the contact resistance value of two-point nanoprobing. After systematically adjusting the chamber parameters and imaging parameters, the contact resistance of tungsten and AFM probes has been reduced from 3.07 MΩ to 47.96 KΩ and from 2.59 MΩ to 75.10 KΩ, respectively. This investigation will serve as a useful guideline to reduce the contact resistance in SEM-based nanoprobing and help improve electrical contacts between the nanoprobes and the sample.

References

[1] G. Shen and D. Chen, "One-dimensional nanostructures for electronic and optoelectronic devices," *Front. Optoelectron. China*, vol. 3, no. 2, pp. 125–138, 2010.

[2] N. Tao, "Nanoelectronics, sensors and single molecule biophysics," *J. Phys. Condens. Matter*, vol. 24, no. 16, p. 160 301, 2012.

[3] A. Vil, F. Hernndez-Ramirez, J. Rodrguez, O. Casals, A. Romano-Rodrguez, J. Morante, and M. Abid, "Fabrication of metallic contacts to nanometre-sized materials using a focused ion beam (FIB)," *Mater Sci Eng C*, vol. 26, no. 5C7, pp. 1063 –1066, 2006.

[4] V. Fauske, M. Erlbeck, J. Huh, D. Kim, A. Munshi, D. Dheeraj, H. Weman, B. Fimland, and A. van Helvoort, "In situ electronic probing of semiconducting nanowires in an electron microscope," *J. Microsc.*, vol. 262, no. 2, pp. 183–188, 2016.

[5] V. Gopal, V. R. Radmilovic, C. Daraio, S. Jin, P. Yang, and E. A. Stach, "Rapid prototyping of site-specific nanocontacts by electron and ion beam assisted direct-write nanolithography," *Nano Lett.*, vol. 4, no. 11, pp. 2059–2063, 2004.

[6] V. Gopal, E. A. Stach, V. R. Radmilovic, and I. A. Mowat, "Metal delocalization and surface decoration in direct-write nanolithography by electron beam induced deposition," *Appl. Phys. Lett.*, vol. 85, no. 1, pp. 49–51, 2004.

[7] F. Hernandez-Ramirez, J. Rodriguez, O. Casals, E. Russinyol, A. Vila, A. Romano-Rodriguez, J. Morante, and M. Abid, "Characterization of metal-oxide nanosensors fabricated with focused ion beam FIB," *Sens. Actuators, B*, vol. 118, no. 1-2, pp. 198 –203, 2006.

[8] I. Utke, P. Hoffmann, and J. Melngailis, "Gas-assisted focused electron beam and ion beam processing and fabrication," *J. Vac. Sci. Technol., B*, vol. 26, no. 4, pp. 1197–1276, 2008.

[9] S. Bauerdick, A. Linden, C. Stampfer, T. Helbling, and C. Hierold, "Direct wiring of carbon nanotubes for integration in nanoelectromechanical systems," *J. Vac. Sci. Technol., B*, vol. 24, no. 6, pp. 3144–3147, 2006.

[10] S. Rubanov and P. R. Munroe, "FIB-induced damage in silicon," *J. Microsc.*, vol. 214, no. 3, pp. 213–221, 2004.

[11] G. Chen, E. M. Gallo, J. Burger, B. Nabet, A. Cola, P. Prete, N. Lovergine, and J. E. Spanier, "On direct-writing methods for electrically contacting gaas and ge nanowire devices," *Appl. Phys. Lett.*, vol. 96(22), no. 22, p. 223 107, 2010.

[12] A. S. Walton, C. S. Allen, K Critchley, M. L. Gorzny, J. E. M. c Kendry, R. M. D. Brydson, B. J. Hickey, and S. D. Evans, "Four-probe electrical transport measurements on individual metallic nanowires," *Nanotechnology*, vol. 18, no. 6, p. 065 204, 2007.

[13] A. Bietsch, M. A. Schneider, M. E. Welland, and B. Michel, "Electrical testing of gold nanostructures by conducting atomic force microscopy," *J. Vac. Sci. Technol., B*, vol. 18, no. 3, pp. 1160–1170, 2000.

[14] M. C. Hersam, A. C. F. Hoole, S. J. OShea, and M. E. Welland, "Potentiometry and repair of electrically stressed nanowires using atomic force microscopy," *Appl. Phys. Lett.*, vol. 72, no. 8, pp. 915–917, 1998.

[15] S. Kleindiek, A. Rummel, K. Schock, and M. Kemmler, "Combining current imaging and electrical probing for fast and reliable in situ electrical fault isolation," in *Proc: European Microscopy Congress, 2016*, Wiley Online Library, 2016.

[16] J.-O. Lee, C Park, J.-J. Kim, J. Kim, J. W. Park, and K.-H. Yoo, "Formation of low-resistance ohmic contacts between carbon nanotube and metal electrodes by a rapid thermal annealing method," *J. Phys. D: Appl. Phys.*, vol. 33, no. 16, p. 1953, 2000.

[17] H. Maki, M. Suzuki, and K. Ishibashi, "Local change of carbon nanotube-metal contacts by current flow through electrodes," *J. Appl. Phys.*, vol. 43, no. 4S, p. 2027, 2004.

[18] A. Bachtold, M. Henny, C. Terrier, C. Strunk, C. Schnenberger, J.-P. Salvetat, J.-M. Bonard, and L. Forr, "Contacting carbon nanotubes selectively with low-ohmic contacts for four-probe electric measurements," *Applied Physics Letters*, vol. 73, no. 2, pp. 274–276, 1998.

[19] Z. Zhang, K. Yao, Y. Liu, C. Jin, X. Liang, Q. Chen, and L.-M. Peng, "Quantitative analysis of current-voltage characteristics of semiconducting nanowires: decoupling of contact effects," *Adv. Funct. Mater.*, vol. 17, no. 14, pp. 2478–2489, 2007.

[20] L. Xiao, H. Xiao-Bo, L. Jun-Ling, G. Li, H. Qing, S. Dong-Xia, and G. Hong-Jun, "Four-probe scanning tunnelling microscope with atomic resolution for electrical and electro-optical property measurements of nanosystems," *Chinese Phys.*, vol. 14, no. 8, p. 1536, 2005.

[21] Q. Chen, S. Wang, and L.-M. Peng, "Establishing ohmic contacts for in situ current-voltage characteristic measurements on a carbon nanotube inside the scanning electron microscope," *Nanotechnology*, vol. 17, no. 4, p. 1087, 2006.

[22] S. Zhao, O. Salehzadeh, S. Alagha, K. L. Kavanagh, S. P. Watkins, and Z. Mi, "Probing the electrical transport properties of intrinsic inn nanowires," *Applied Physics Letters*, vol. 102, no. 7, p. 073 102, 2013.

[23] B. K. Teo and X. H. Sun, "From top-down to bottom-up to hybrid nanotechnologies: road to nanodevices," *J. Cluster Sci.*, vol. 17, no. 4, pp. 529–540, 2006.

[24] R. G. Hobbs, N. Petkov, and J. D. Holmes, "Semiconductor nanowire fabrication by bottom-up and top-down paradigms," *Chem. Mater.*, vol. 24, no. 11, pp. 1975–1991, 2012.

[25] A. A. Tseng, K. Chen, C. D. Chen, and K. J. Ma, "Electron beam lithography in nanoscale fabrication: recent development," *IEEE Trans. Electron. Packag. Manuf.*, vol. 26, no. 2, pp. 141–149, 2003.

[26] R. Janoch, A. M. Gabor, A. Anselmo, and C. E. Dub, "Contact resistance measurement - observations on technique and test parameters," in *2015 IEEE 42nd Photovoltaic Specialist Conference (PVSC)*, 2015, pp. 1–6.

[27] N. Stavitski, M. J. H. van Dal, A. Lauwers, C. Vrancken, A. Y. Kovalgin, and R. A. M. Wolters, "Systematic TLM measurements of NiSi and PtSi specific contact resistance to n- and p-type Si in a broad doping range," *IEEE Electron Device Lett.*, vol. 29, no. 4, pp. 378–381, 2008.

[28] C. Ru, Y. Zhang, Y. Sun, Y. Zhong, X. Sun, D. Hoyle, and I. Cotton, "Automated four-point probe measurement of nanowires inside a scanning electron microscope," *IEEE Trans. Nanotechnol.*, vol. 10, no. 4, pp. 674–681, 2011.

[29] A. E. Vladar, M. T. Postek Jr., and R. Vane, "Active monitoring and control of electron-beam-induced contamination," *Proc. SPIE*, vol. 4344, pp. 835–843, 2001.

[30] C. Soong, P. Woo, and D. Hoyle, "Contamination cleaning of TEM/SEM samples with the zone cleaner," *Micros. Today*, vol. 20, no. 06, pp. 44–48, 2012.

[31] M. T. Postek, "An approach to the reduction of hydrocarbon contamination in the scanning electron microscope," *Scanning*, vol. 18, no. 4, pp. 269–274, 1996.

[32] E. H. Rhoderick, "Metal-semiconductor contacts," *IEE J. Solid-State and Electron Device*, vol. 129, no. 1, pp. 1–14, 1982.

[33] A. Yu, "Electron tunneling and contact resistance of metal-silicon contact barriers," *Solid State Electron.*, vol. 13, no. 2, pp. 239 –247, 1970.

[34] H. Muta, "Electrical properties of platinum-silicon contact annealed in an H2 ambient," *Jpn. J. Appl. Phys.*, vol. 17, no. 6, p. 1089, 1978.

[35] D. Zhang, "A nano-tensile testing system for studying nanostructures inside an electron microscope," PhD thesis, STI, 2010.

[36] A. Vladar and M. Postek, "Electron beam-induced sample contamination in the sem," *Microsc. Microanal.*, vol. 11, pp. 764–5, Aug. 2005.

[37] A. J. V. Griffiths and T Walther, "Quantification of carbon contamination under electron beam irradiation in a scanning transmission electron microscope and its suppression by plasma cleaning," *J. Phys.: Conf. Ser.*, vol. 241, no. 1, p. 012 017, 2010.

[38] K. Rykaczewski, W. B. White, and A. G. Fedorov, "Analysis of electron beam induced deposition EBID of residual hydrocarbons in electron microscopy," *J. Appl. Phys.*, vol. 101, no. 5, p. 054 307, 2007.

The connection between Chapter 4 and Chapter 5

Chapter 4 reported an experimental investigation of the impact of SEM chamber conditions (cleanliness level and vacuum pressure) and imaging parameters (magnification and acceleration voltage) on the contact resistance value of two-point nanoprobing. An experimental strategy of reducing probe-sample contact resistance through systematically adjusting the experimental parameters has been identified.

In Chapter 5, utilizing the developed SEM-based *in-situ* two-point electrical nanoprobing system represented in Chapter 4, I will carry out a systematic electrical characterization of single n-i-n-n^+ GaN nanowires (NWs), which holds great potential for use in high-power and/or high-frequency electronic devices. The electrical transport properties and breakdown behaviors of single n-i-n-n^+ GaN nanowires (NWs) will be investigated through *in-situ* nanoprobing in SEM. And the dependence of the NW breakdown parameters on the n^+-GaN Si-doping concentration and the NW diameter will be experimentally quantified. Enabled by the low NW-nanoprobe contact resistance, a breakdown current density of 4.65 MA/cm^2 and a breakdown power of 96.84 mW are achieved, both the highest among the previously reported results measured on GaN NWs.

CHAPTER 5
Characterizing the Electrical Breakdown Properties of Single n-i-n-n^+:GaN Nanowires

Characterizing the Electrical Breakdown Properties of Single n-i-n-n^+:GaN Nanowires

Juntian Qu[1,2,†], Renjie Wang[3,†], Yu Sun[1], Ishiang Shih[3], Zetian Mi[3,4*] and Xinyu Liu[1,2*]

[1]*Department of Mechanical and Industrial Engineering, University of Toronto, Toronto, ON, Canada, M5S 3G8*

[2]*Department of Mechanical Engineering, McGill University, Montreal, QC, Canada, H3A 0C3*

[3]*Department of Electrical and Computer Engineering, McGill University, Montreal, QC, Canada, H3A 0E9*

[4]*Department of Electrical Engineering and Computer Science, University of Michigan, Ann Arbor, MI, United States, 48109*

†These authors contributed equally to this work.

*Corresponding author: (xyliu@mie.utoronto.ca)

Published on: *Applied Physics Letters*, vol. 113, no. 19, 193103, 2018.

ABSTRACT: The electrical transport properties and breakdown behaviors of single n-i-n-n^+ GaN nanowires (NWs) are investigated through *in-situ* nanoprobing under scanning electron microscopy (SEM). The nanoprobing contact resistance is dramatically reduced by increasing the Si-doping concentration of the top n^+-GaN segment of the NW. The dependence of the NW breakdown parameters (i.e., breakdown voltage, power and current density) on the n^+-GaN Si-doping concentration and the NW diameter is experimentally quantified and explained by the localized thermal decomposition mechanism of the NW. Enabled by the low NW-nanoprobe contact resistance, a breakdown current density of 4.65 MA/cm^2 and a breakdown power of 96.84 mW are achieved, both the highest among the previously reported results measured on GaN NWs.

Index Terms - *In-situ* electrical nanoprobing, electrical breakdown, GaN NW, breakdown current density.

5.1 Introduction

Recent advances in microelectronics have made group III-nitride nanowires (NWs) in the spotlight owing to the excellent controllability of their electronic properties [1] and their broad applications in (opto)electronics [2]. Catalyst-free gallium nitride (GaN) NWs, usually vertically grown on a substrate by molecular beam epitaxy (MBE), possess high crystalline quality (e.g., strain- and dislocation-free) and high electron mobilities, and thus hold great potential for use in high-power and/or high-frequency electronic devices [2, 3].

The electrical properties (e.g., transport property and breakdown behavior) of GaN NWs significantly affect the performance of GaN-NW-based devices. As an important electrical property, the breakdown current density of GaN nanowires has been studied previously as guidelines to the design of GaN nanowire devices. Due to Joule heating, the breakdown of horizontally-arranged GaN nanowires have been observed to occur at an average current density of approximately 3×10^6 A/cm^2 at estimated peak temperatures around 1050-1100 K [4, 5]. However, due to phonon surface scattering, the relatively poor heat dissipation of nanowires has hindered the development of high performance vertically oriented GaN nanowire devices [6, 7]. Besides, for GaN-based laser optoelectrical circuits, the requirement of high current density (much higher than threshold current density) is essential to excite lasers for high output. For instance, under CW operation, the threshold current density of green-emitting GaN-based quantum well lasers were reported in the range of $\sim$ 3.1-18 kA/cm^2 [8, 9, 10] and that of red-emitting vertically oriented GaN-based nanowire laser is $\sim$ 2.9 kA/cm^2 [11]. The level of breakdown current density of GaN NWs tends to depend on nanowire geometries (e.g., diameter and height), material compositions, and arrangements on their growth substrates. Recently, GaN-NW arrays with precisely controlled geometries, composition, and array pattern arrangement have been synthesized by using selective area epitaxy (SAE) [12, 13, 14, 15, 16], and these GaN-NW arrays have been used to fabricate a variety of optoelectronic devices such as multi-color light emitting devices (LEDs) and full-color displays [15, 16, 17].

The GaN NWs are typically grown on sapphire substrates with thick GaN epilayers [14, 15, 16]. Compared to sapphire substrates, heavily doped Si substrates exhibit advantages of high

thermal and electrical conductivities, and thus can serve as a good heat sink at the NW bottom for high-power electronic applications. To be compatible with existing silicon device technologies, SAE of GaN NWs on Si substrate has been recently explored and investigated by many researchers [18, 19, 20]. In this work, we synthesized, high-quality n-i-n-n^+ GaN NWs on Si substrate using SAE and obtained SAE NWs with different diameters on the same Si substrate. This allows us to readily perform electrical nanoprobing on as-grown GaN NWs and study the effect of NW diameter and doping level on the electrical breakdown behavior of the NWs.

This article reports the electrical characterization of single n-i-n-n^+ GaN NWs vertically grown on a Si substrate through SAE. Benefiting from the flexibility of *in-situ* nanoprobing technique under scanning electron microscopy (SEM), the electrical breakdown parameters (i.e., breakdown voltage, power and current density) of the n-i-n-n^+ GaN NWs were experimentally quantified, and the dependence of the NW breakdown behavior on the NW diameter and the Si-doping concentration of the top n^+-GaN segment of the NW was investigated. Leveraging the excellent transport property of the n-i-n-n^+ NW structure and the low NW-nanoprobe contact resistance (enabled by the high Si-doping level of the n^+-GaN segment), a breakdown current density of up to 4.65 MA/cm^2 and a breakdown power of up to 96.84 mW were achieved, both the highest among the previously reported breakdown parameters of single GaN NWs. The results will provide useful guidelines for experimentally improving the breakdown performance of single GaN NWs with precisely-controlled geometries on Si substrates, and thus enable applications of these GaN NWs in high-power nanoelectronics.

5.2 Epitaxial Growth of Nanowires

The n-i-n-n^+ GaN-NW heterostructures were epitaxially grown on an n-Si substrate (prime grade as-doped Si wafers, Nova Electronic Materials; thickness : 279 $\pm$ 25 μm), using a radio frequency plasma-assisted MBE system (GENxplor, Veeco). Ti-mask-based SAE was employed to regulate the NW width [12, 13, 21]. The molecular beam epitaxy (MBE) growth parameters of the top and bottom n-GaN segments and the middle non-doped segment are: (i) the substrate temperature: 885 °C, (ii) Ga beam equivalent pressure: 2.35×10^{-7} Torr, and (iii) the Si-doping

cell temperature: 1150 °C. The top n^+-GaN segment is more heavily Si-doped to reduce the NW-electrode contact resistance. To study the effect of the Si-doping concentration of the n^+-GaN segment on the electrical characteristics of the NW, we grew samples with n^+-GaN segments at four different Si-doping cell temperatures: 1150 °C, 1200 °C, 1300 °C, and 1350 °C, corresponding to Si-doping concentrations of 1.52×10^{18} cm^{-3}, 4.89×10^{18} cm^{-3}, 5.04×10^{19} cm^{-3}, 1.48×10^{20} cm^{-3}, respectively.

As shown in Fig. 5–1(a), an n-i-n-n^+ GaN NW heterostructure consists of segments of ∼100 nm lightly Si-doped n-GaN, ∼500 nm non-doped GaN, ∼100 nm lightly Si-doped n-GaN, and ∼100 nm heavily Si-doped n^+-GaN (bottom to top). The heavy doping of the n^+-GaN segment ensures low resistance between the NW and the subsequently deposited Ti/Au electrode on its top surface.

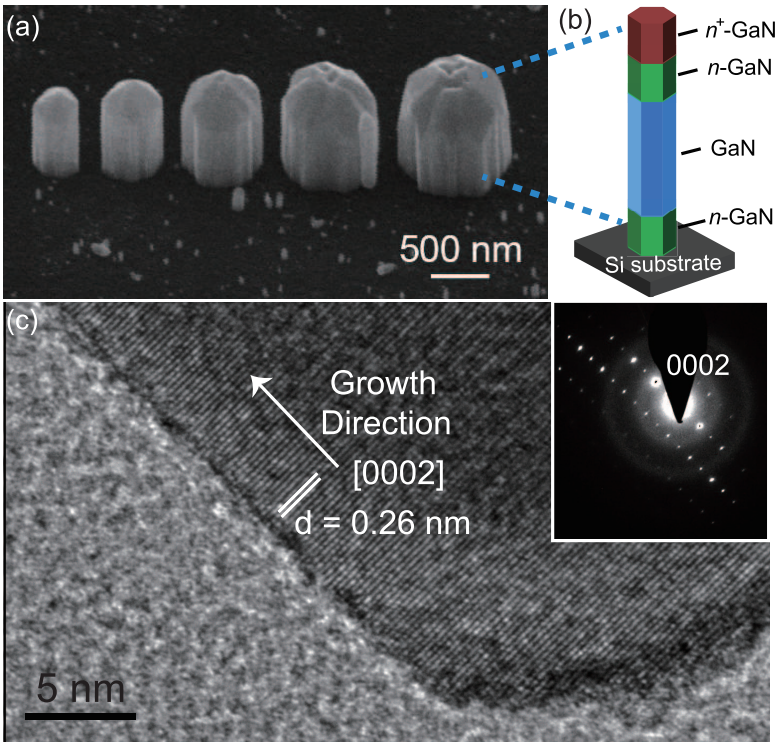

Figure 5–1: Sample illustrations: (a) SEM images (45° tilt angle) of GaN single nanowires with precisely controlled diameters ranging from 400-800 nm. (b) Schematic of single n-i-n-n^+:GaN nanowire grown on Si substrate. (c) High-resolution TEM image and selected area electron diffraction (SAED) pattern (inset).

Fig. 5–1(b) shows a typical SEM photograph of five n-i-n-n$^+$:GaN NWs grown on the same substrate, all with a hexagonal morphology. The maximum diameter of the hexagonal NW cross-section (simply called diameter of the NW in the following sections) of the NW samples range from 400 nm to 950 nm, and were controlled by adjusting the widths of the Ti nanohole initially patterned on the Si substrate (Ti mask). The capability of readily controlling the NW diameter, enabled by the Ti-mask SAE technique, allows us to characterize the electrical transport properties of the n-i-n-n$^+$ GaN NWs at different NW diameters and therefore establish the relationship between the NW diamter/cross-sectional area and the material's electrical breakdown parameters such as breakdown voltage and power.

The crystal quality of the NW was examined through high-resolution transmission electron microscopy (TEM) (FEI Tecnai F20 with a camera of 4k $\times$ 4k pixels). Fig. 5–1(c) shows the crystalline structure of the root region of the n-i-n-n$^+$:GaN NW, indicating high crystal quality. The interplane spacing of the NW crystal was measured to be 0.26 nm, confirming the NW growth along the [0002] direction (c-axis). The selected-area electron diffraction (SAED) pattern (inset of Fig. 5–1(c)) also confirms the [0002] growth direction.

5.3 Electrical Nanoprobing of Single NWs

To improve the electrical contacts between the two nanoprobes and the NW sample, Ti/Au electrodes were deposited on top surfaces of the NWs and on the back side of the Si substrate (Fig. 5–2(a)) through e-beam deposition. The Ti/Au deposition on top of the n$^+$-GaN segment was based on polyimide-based surface passivation and planarization [22], a Ti (20 nm)/Au (100 nm) bilayer was first deposited on the backside of Si substrate as the bottom contact. A polyimide layer was then spin-coated to cover the single NWs, followed by oxygen plasma etching to reveal the top surfaces of the n$^+$-GaN segments. Ti (10 nm)/Au (10 nm) metal layers were then deposited onto the n$^+$-GaN top surfaces, followed by rapid thermal annealing at $\sim$ 550 °C for 1 minute in nitrogen. Eventually, the polyimide layer remained on the sample substrate to enclose the NWs, preventing any contact property deterioration that could be induced by the sample exposure to air [3]. Due to the height difference ($\sim$ 50 nm) between the top surfaces of the polyimide and the

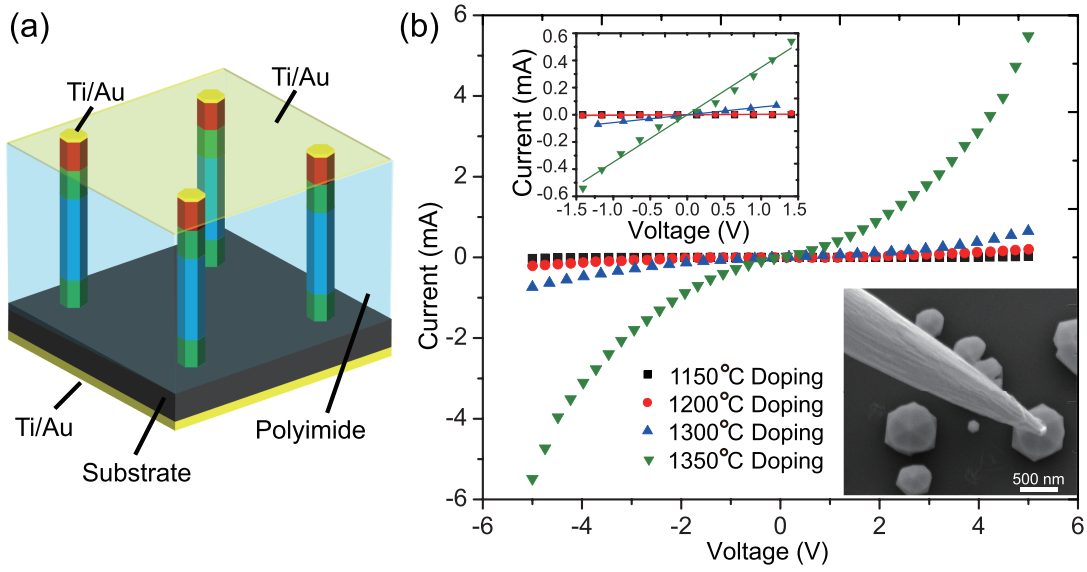

Figure 5–2: (a) 3D schematic of GaN single nanowire devices fabricated on Si substrate. (b) Representative I-V characteristics of single GaN nanowire with the different doping levels, obtained by nanoprobing individual GaN nanowire with length ∼ 800 nm and diameter ∼ 500 nm. The top-left inset shows the magnified I-V curves (voltage: -1.5 V to 1.5 V), based on which the NW overall resistance was calculated. The bottom-right inset shows the SEM image of such nanoprobing with a Pt-coated tungsten tip.

n^+-GaN segment, there is little Ti/Au deposited on the side wall of the n^+-GaN segment, and there is no electrical connection between individual NWs and the Ti/Au bilayer deposited on the polyimide.

We performed two-point electrical *in-situ* nanoprobing of the as-grown single n-i-n-n^+:GaN NWs inside a scanning electron microscope (SEM) by following a previously developed protocol [23]. Compared with the conventional nanolithography-based techniques for establishing electrical contacts with a single NW [24], *in-situ* nanoprobing is relatively easy to perform and more rapid, and allows the testing of many NWs with less experimental efforts for examining the effect of different growth parameters on the material's electrical properties. More importantly, nanolithography for patterning electrodes on a NW involves chemical treatment of the NW that may alter the NW's electrical properties [24, 25], but this is avoided in *in-situ* nanoprobing.

A nanomanipulator (LF-2000, TNI), mounted inside an SEM (Quanta 450 FEG, FEI), was employed for positioning conductive nanoprobes for electrical probing and testing of single NWs.

The nanomanipulator integrates position feedback (resolution: 0.1 nm) on each of its fine positioning stage, allowing closed-loop controlled, high-precision nanopositioning. The inset of Fig. 5–2(b) shows an n-i-n-n^+:GaN NW being probed by a Pt-coated tungsten nanoprobe (ST-20-0.5, GGB Industries).

In our nanoprobing experiments, one nanoprobe contacts the metal at the top surface of a GaN NW (inset of Fig. 5–2(b)), and the other one contacts the back electrode on the back side of Si substrate. The resistance of the Si substrate (resistivity: 0.005 ohm $\cdot$ cm, thickness: 279$\pm$25 μm) along its thickness was estimated to be 0.00014 Ω, which can be safely ignored comparing to the GΩ- to kΩ-level resistance of the NW. A precision source meter (SMU 2400, Keithley) was employed for I-V measurements of the NW samples. The sweeping voltage was from -5 V to 5V with a step increment of 0.25 V and a ramp rate of 100 V/s. During the measurement, the e-beam radiation from the SEM was switched off using a beam blanker to avoid any electrical noise induced by the incident electrons. In addition, before each measurement, the two nanoprobes connecting the GaN NW sample were firstly grounded to eliminate any charge built up on the sample due to SEM imaging.

5.4 Tranport Properties Characterization

Fig. 5–2(b) shows the representative I-V curves of single n-i-n-n^+ GaN NWs (height: 800 nm, and diameter: 500 nm) with four different doping concentrations in the n^+ segments of the samples. The linear I-V characteristics is observed in low voltage bias (-1.5 - 1.5 V, top-left inset of Fig. 5–2(b)) region (ohmic regime), while the nonlinear current voltage characteristics is generally observed at relatively high voltage bias (-6 - 6 V) region which is a space-charge-limited (SCL) regime for a solid with a relatively low free carrier concentration [26, 27]. One can also see that the Si-doping level in the n^+-GaN segment of an n-i-n-n^+ GaN NW significantly affects its I-V characteristics. According to the slopes of the linear regions of the I-V curves in the low sweep voltage range of -1.5–1.5 V, the resistance values of individual GaN NWs were calculated to be 2 MΩ, 0.5 MΩ, 16 KΩ and 3.3 KΩ for NWs with Si doping temperatures of 1150 °C, 1200 °C, 1300 °C and 1350 °C, respectively (n=5). Based on the resistance equation $R = l/\sigma A$, the overall

conductivity values (denoted by σ) of these NWs were calculated to be 0.023 $(\Omega \cdot \text{cm})^{-1}$, 0.092 $(\Omega \cdot \text{cm})^{-1}$, 2.940 $(\Omega \cdot \text{cm})^{-1}$, and 14.255 $(\Omega \cdot \text{cm})^{-1}$ for the Si doping temperatures of 1150 °C, 1200 °C, 1300 °C and 1350 °C, respectively.

Based on the overall conductivity of a single NW, we estimated the electron density of the intrinsic, non-doped GaN segment of the NW, which is one of the primary parameters of the NW quality. To this end, we used the resistance data measured from n-i-n-n^+ GaN NWs with n^+ segments doped at 1350 °C, which have the lowest contact resistance with the top electrode. Specifically, the electron density value of non-doped GaN segment was calculated from equation $\sigma = e \cdot n \cdot \mu$ [28], where σ is the conductivity in non-doped GaN segment, e is the constant value of elemental charge, n is the electron density to be obtained, and μ is the electron mobility for non-doped GaN NWs. A previous study has tested the electron mobility of non-doped GaN NWs to be 650 $cm^2/(\text{V} \cdot \text{s})$ [1], which was used in our calculation. The corresponding conductivity σ of the non-doped GaN segment was calculated to be 10.11 $(\Omega \cdot \text{cm})^{-1}$ based on the equation $R = l/(\sigma \cdot A)$, where the resistance value R for non-doped GaN segment was determined to be 3044 Ω (by subtracting the resistance values of the n-GaN and n^+-GaN segments from the total NW resistance of 3.3 KΩ), l is the length of the non-doped GaN segment (l =100 nm), and A is the NW cross-sectional area (diameter: 500 nm). From equation $\sigma = e \cdot n \cdot \mu$, the electron density value of non-doped GaN segment was finally estimated to be 9.71×10^{16} cm^{-3}, which is in agreement with the previously reported results of high-quality GaN materials [1, 29].

5.5 Electrical Breakdown Properties Characterization

After the I-V characterization, single n-i-n-n^+ GaN NWs were driven to their electrical breakdown by applying a forward ramp voltage from 0 V to 10 V (with a step increment of 0.25 V and a ramp rate of 100 V/s) at room temperature (21 °C), and the corresponding I-V curves were recorded. When the ramp voltage reached the NW breakdown value, the GaN NW was broken because of the Joule heating effect, and the breakdown voltage of the NW was determined to be the peak value of the I-V curve before the current dropped to zero (Fig. 5–4). Figs. 5–3(a)–(c) shows a sequence of three SEM photographs illustrating the process of NW breakdown testing. We

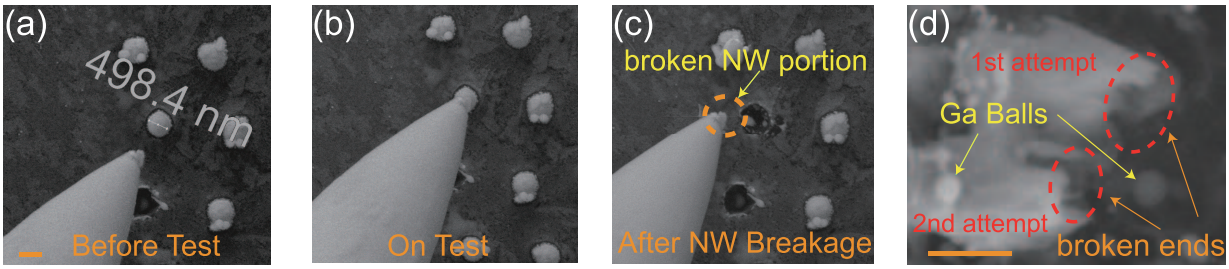

Figure 5–3: Sequential SEM images of single GaN nanowire probing: (a) Before breakdown tests (left scale bar: 500 nm). (b) During breakdown tests. (c) After breakdown tests. (d) Magnified image (right scale bar: 500 nm) of evaporated Ga balls and broken nanowires cross section area of 1st and 2nd measurement.

also detached two broken NW portions (from two individual tests) onto the same Si substrate for high-magnification SEM imaging. As shown in Fig. 5–3(d), there were Ga nano-balls on the NW portions that were formed from the thermal decomposition of GaN and the subsequent deposition of the decomposed Ga [4].

The I-V curves for electrical breakdown of single NWs with different diameters (400 nm–900 nm) and Si-doping temperatures (1150 °C–1350 °C) are shown in Figs. 5–4. We can see that the current injected through single NW increased with the applied voltage bias until a certain critical point, beyond which the current dramatically dropped to zero. The current and voltage values at the critical point were defined as the breakdown current and voltage. The dependence of the breakdown voltage on the NW diameter and Si-doping level of the n^+-GaN segment is illustrated in Fig. 5–5(a). Note each data point in Fig. 5–5(a) is the average of breakdown voltage values measured from GaN NWs with the same diameter and Si-doping temperature, and the x-axis error reflects the small variation of the NW diameter. The data show that, for the same n^+ doping concentration, the NW breakdown voltage remains relatively constant with small fluctuations (1150 °C doping: 8.51 ± 0.28 V, 1200 °C doping: 8.23 ± 0.52 V, 1300 °C doping: 6.84 ± 0.78 V, and 1350 °C doping: 5.38 ± 0.25 V). The electric field strength at the NW breakdown was calculated to be in the range of 10.76-17.02 MV/m, which is higher than that ($\sim$ 4.36 MV/m) measured from

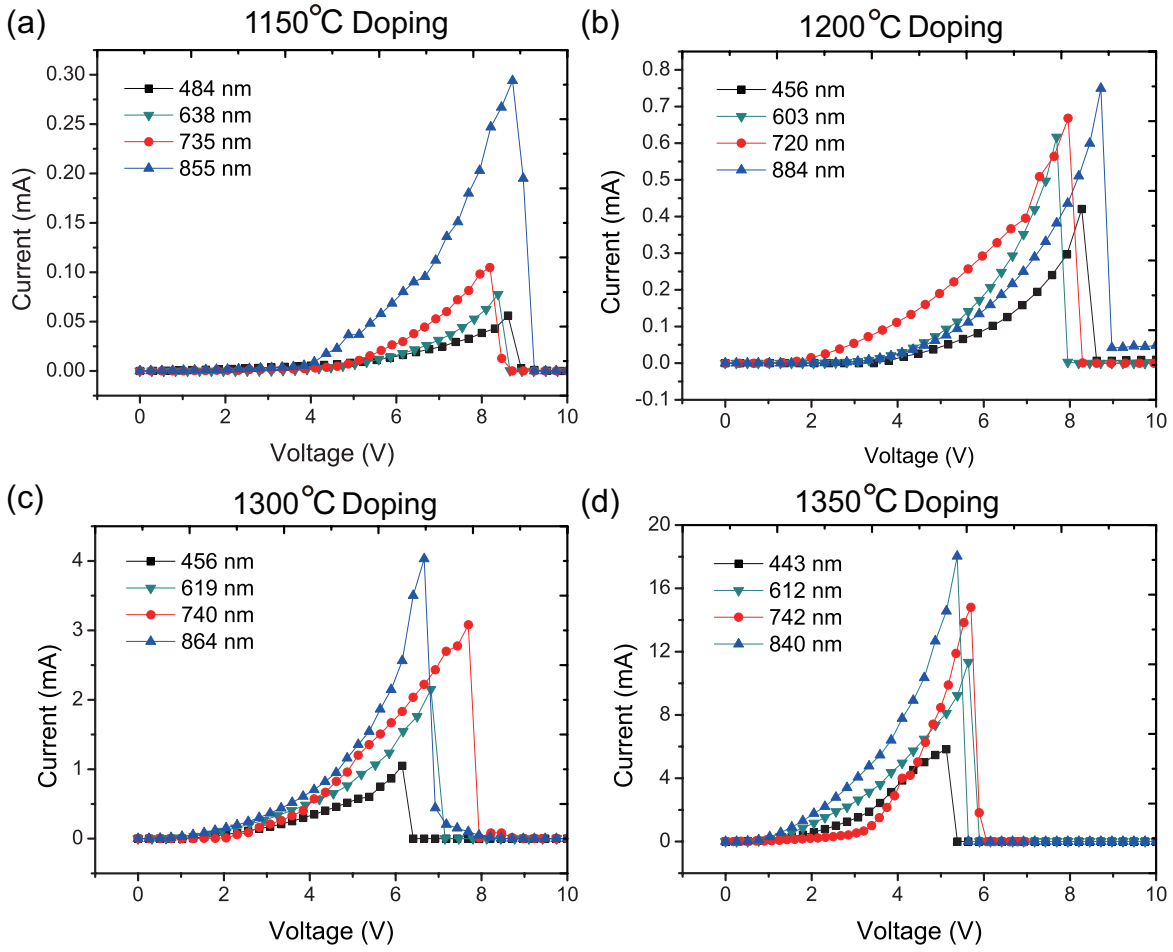

Figure 5–4: Single GaN nanowire failure I-V characteristics with different Si doping temperatures used in n^+-GaN: (a) 1150 °C. (b) 1200 °C. (c) 1300 °C. (d) 1350 °C.

single GaN NWs tested in a lateral arrangement [5]. Furthermore, it was observed that, at the same NW diameter, the breakdown voltage decreased when the n^+ doping level increased.

A previous study [5] demonstrated that the electrical breakdown of a GaN NW, which was arranged horizontally inside a TEM, occurred in the middle portion of the NW, because the thermal distribution of the NW has the highest temperature (T_{max}) in its middle portion and lower temperatures at its two ends connected with electrodes. In our experimental setup, the Pt-coated tungsten nanoprobe has higher thermal conductivity than that of the Si substrate; thus, the top of the n-i-n-n^+ GaN NW has a lower temperature than that of NW's root. Assuming

constant thermal conductivity over the entire NW, the NW's highest temperature T_{max} is [5, 30]

$$T_{max} = T_0 \exp\left(\frac{\alpha\sigma U^2}{8}\right) \tag{5.1}$$

where α is a constant inversely proportional to the thermal conductivity of the NW, σ is the electrical conductivity of the NW, and U is the applied DC bias (by ignoring the nanoprobe-NW contact resistance). According to Eq. (5.1), the maximum temperature T_{max} on the NW only depends on the DC bias not the NW diameter [5]. This explains the relatively constant breakdown voltages required to elevate the highest NW temperature (T_{max}) to the material's melting point for NWs with the same Si-doping concentration but different diameters (Fig. 5–5(a)). In addition, a higher Si-doping concentration results in a larger electrical conductivity (σ) of the NW; this led to the decrease in the breakdown voltage U for NWs with the same diameter (Fig. 5–5(a)) when the Si-concentration increased, assuming T_{max} is the same for all the NWs. Note that Eq. (5.1) does not consider the heat transfer efficiency at the top and bottom of a NW, and was only used to qualitatively explain the observed trends of the breakdown voltage vs. the Si-doping level and the NW diameter.

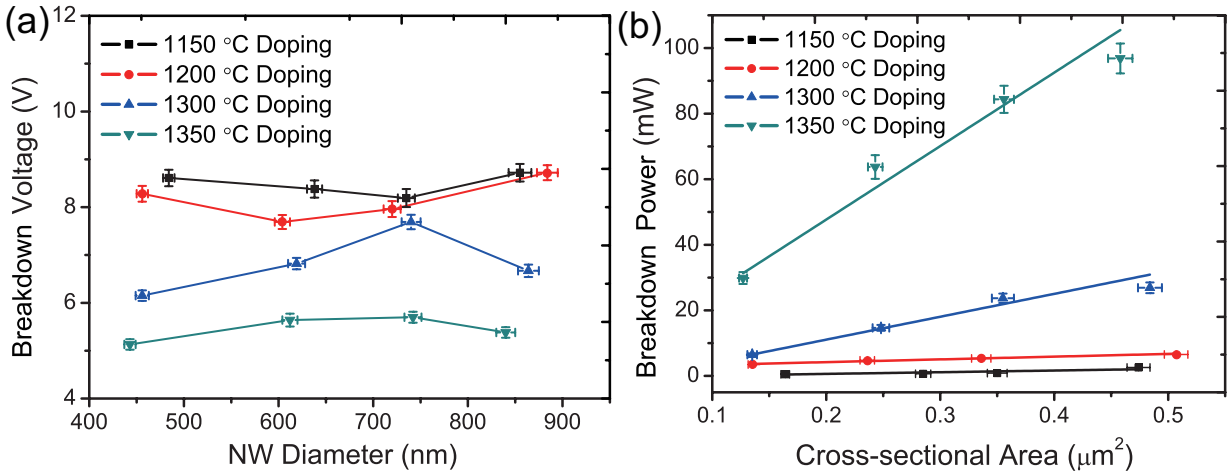

Figure 5–5: (a) Doping-dependent breakdown voltage as a function of NW diameter. (b) Doping-dependent NW breakdown power as a function of NW cross-sectional area (calculated as regular hexagonal).

Fig. 5–5(b) shows the dependence of the NW breakdown power P (the product of the breakdown voltage and current) on the NW diameter and the n^+ doping level. One can observe that for each Si-doping concentration, the NW breakdown power is linearly proportional to the NW cross-sectional area. For the same cross-sectional area, the NW breakdown power increases with the doping concentration.

Fitting $R = l/\sigma A$ and the power equation $P = U^2/R$ into Eq. 5.1 yields:

$$T_{max} = T_0 \exp(\frac{\alpha P l}{8A}) \tag{5.2}$$

From Eq. (5.2), we can find that the breakdown power (the P value required to drive T_{max} on the NW to reach its melting temperature) is linearly proportional to the NW cross-sectional area (A).

With the same NW cross-sectional area, the higher the Si-doping concentration (thus α) becomes, the higher the breakdown power is. Based on Fig. 5–5(b), the maximum DC power in a single GaN NW (diameter: 840 nm; Si-doping temperature: 1350 °C) is 96.84 mW, which is comparable to the result reported in [4].

In addition, the dependence of NW breakdown current density on the NW diameter is presented in the Fig. 5–6(a), showing a slight increase in the value of breakdown current density with decreased NW diameter at certain Si-doping temperature, this observation is reasonable since the NW surface-to-volume ratio increases when the NW diameter decreases, and a thinner NW dissipates heat more efficiently to the surrounding polyimide and can thus tolerate a larger current density [31]. Such relationship between the current density and the NW diameter has also been reported previously for Cu, Au and Bi NWs [31, 32, 33]. For NWs with the same diameter, the breakdown current density increases with the Si-doping level, also illustrating the significant effect of the Si-doping level on the NW breakdown properties.

Also it was observed that at fixed NW diameter, breakdown current density increases with the increased Si-doping temperature, as further interpretation, as shown in Fig. 5–6(b), the NW breakdown current density increases exponentially with the Si-doping temperature. This is primarily due to the fact that the contact resistance between the top electrode and the n^+-GaN

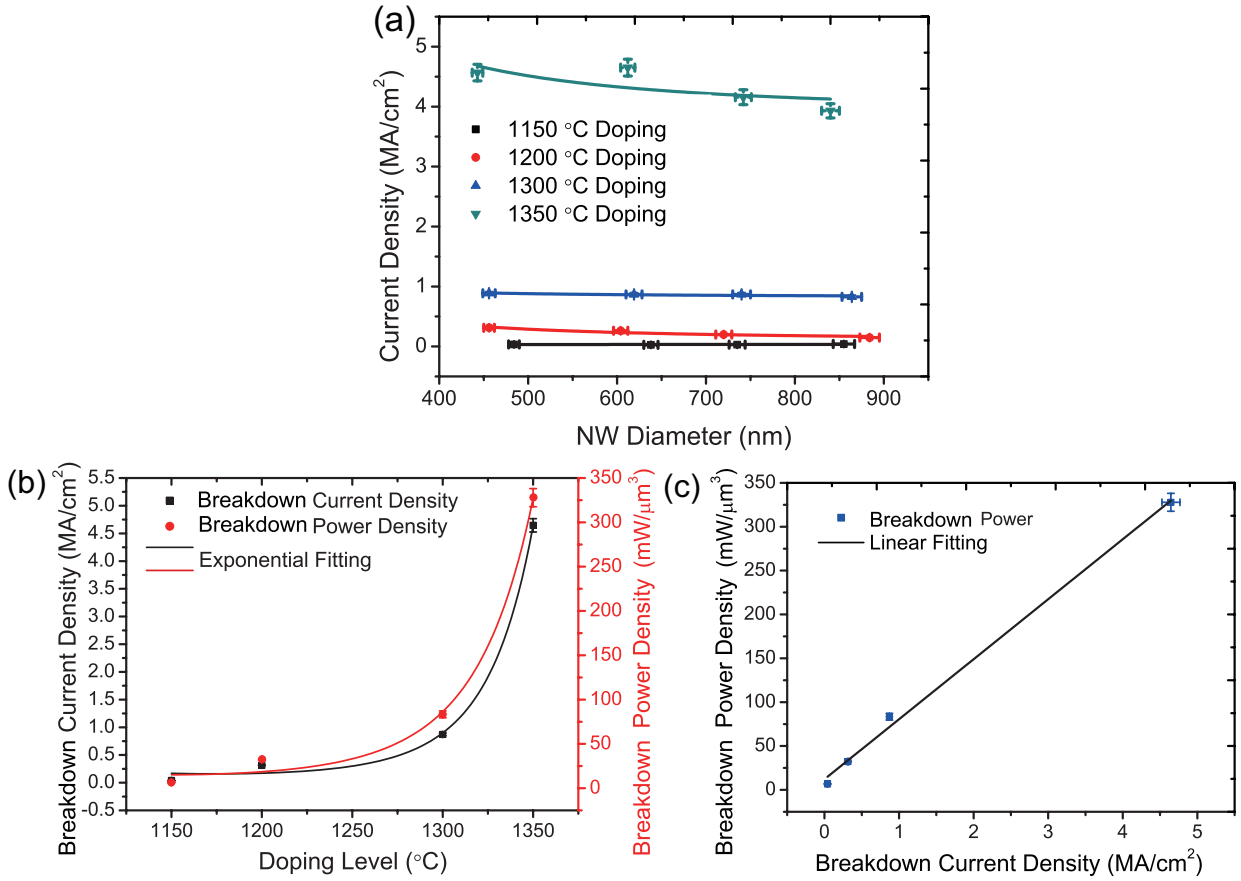

Figure 5–6: (a) Doping-dependent current density as a function of NW diameter. (b) NW breakdown current density and breakdown power density (red line) as a function of doping temperature (the four data points correspond to the highest current density and power density within four doping temperature from 1150 °C to 1350 °C). (c) NW breakdown power density as a function of NW current density. n=3 for all the data.

segment decreases with the Si-doping concentration [34], and that the Si-doping concentration is in an exponential relationship with the Si-doping temperature [34, 35]. The maximum current density we have achieved was 4.65 MA/cm^2 (current: 11.3 mA, NW diameter: 612 nm, and Si-doping temperature: 1350 °C), which is over 76 times higher than that (0.06 MA/cm^2) of GaN NWs (current: 244 μA, and diameter: 800 nm) reported in [4]. Due to the relatively constant breakdown voltages shown in Fig. 5–5(a) for the same n^+ Si-doping concentration, the corresponding NW breakdown power density (red line) also increases exponentially with the Si-doping temperature, the maximum power density we have achieved was 327.84 mW/um^3 (power: 63.73 mW, NW diameter: 612 nm,

and Si-doping temperature: 1350 °C). As shown in Fig. 5–6(c), the NW breakdown power density is linearly proportional to the breakdown current density.

The attained ultrahigh NW breakdown power and current density data demonstrate the merits of the unique n-i-n-n^+ heterostructure of the GaN NW and the effectiveness of Si-doping approach (for the top n^+ segment) to reduce the contact resistance of the NW top surface. One can dramatically increase the breakdown current density and the breakdown power of an n-i-n-n^+ GaN NW by increasing the Si-doping level of the n^+ segment. This illustrates an easy experimental approach for tuning these important electrical parameters of GaN NWs, to improve the performance of GaN-NW-based electronic devices. Note that heat sinks at the top and bottom of a GaN NW also significantly affect its electrical breakdown properties. In a practical (opto)electronic device involving vertically-grown GaN NWs, the heat transfer efficiency at the top and bottom of a NW can be significantly improved by adopting a bottom substrate and a top packaging material both with high thermal conductivity, which will further extend the electrical breakdown limit of the GaN NWs. Moreover, for wire interconnects in modern integrated circuit (ICs), the contact resistance problem also exist [36, 37], and the high contact resistance can cause substantial heating in a high-current IC device. The n^+-segment doping method we demonstrated could potentially mitigate the contact resistance issue in wire interconnects of modern ICs, improving device performance in high-current-density operations [38, 39].

5.6 Conclusion

In conclusion, the electrical properties of single n-i-n-n^+ GaN NWs grown on Si substrates were investigated through *in-situ* two-point nanoprobing inside an SEM. The NW's electrical breakdown parameters (i.e., the breakdown voltage, power and current density) were quantified, and their dependence on the NW diameter and the nanoprobing contact resistance (determined by the Si-doping level of the top n^+-GaN segment) was examined. By tuning the Si-doping concentration of the n^+-GaN segment, we achieved a NW breakdown current density of 4.65 MA/cm^2 and a breakdown power of 96.84 mW, both the highest among the previously reported results from GaN

NWs. The results provide an experimental guideline on how to improve the electrical properties of GaN NWs grown on Si substrates for constructing high-performance electronics.

5.7 Acknowledgment

The authors acknowledge financial supports from the Natural Sciences and Engineering Research Council of Canada (NSERC) (grant numbers: STPGP-2014-463182, RGPIN-2017-06374, and EQPEQ-2015-72835) and the Canada Research Chairs Program (grant no. 237293), the Fonds de recherche du Qubec C Nature et technologies (FRQNT) (through a Merit Scholarship to J. Qu), and the CMC Microsystems (through the Micro-Nano Technologies Financial Assistance Program). The authors also thank Mr. S. Vanka and Dr. Y.H. Ra for their assistance in the MBE growth of GaN NWs.

References

[1] Y. Huang, X. Duan, Y. Cui, and C. M. Lieber, "Gallium nitride nanowire nanodevices," *Nano Lett.*, vol. 2(2), no. 2, pp. 101–104, 2002.

[2] R. K. Debnath, R. Meijers, T. Richter, T. Stoica, R. Calarco, and H. Luth, "Mechanism of molecular beam epitaxy growth of gan nanowires on si(111)," *Appl. Phys. Lett.*, vol. 90(12), no. 12, p. 123 117, 2007.

[3] D. Y. Jeon, K. H. Kim, S. J. Park, J. H. Huh, H. Y. Kim, C. Y. Yim, and G. T. Kim, "Enhanced voltage-current characteristics of gan nanowires treated by a selective reactive ion etching," *Appl. Phys. Lett.*, vol. 89(2), no. 2, p. 023 108, 2006.

[4] T. Westover, R. Jones, J. Y. Huang, G. Wang, E. Lai, and A. A. Talin, "Photoluminescence, thermal transport, and breakdown in joule-heated gan nanowires," *Nano Lett.*, vol. 9(1), no. 1, pp. 257–263, 2009.

[5] J. Zhao, H. Sun, S. Dai, Y. Wang, and J. Zhu, "Electrical breakdown of nanowires," *Nano Lett.*, vol. 11(11), no. 11, pp. 4647–4651, 2011.

[6] D. Li, Y. Wu, P. Kim, L. Shi, P. Yang, and A. Majumdar, "Thermal conductivity of individual silicon nanowires," *Appl. Phys. Lett.*, vol. 83(14), no. 14, pp. 2934–2936, 2003.

[7] L. H. Liang and B. Li, "Size-dependent thermal conductivity of nanoscale semiconducting systems," *Phys. Rev. B*, vol. 73, p. 153 303, 2006.

[8] A. Avramescu, T. Lermer, J. Mller, C. Eichler, G. Bruederl, M. Sabathil, S. Lutgen, and U. Strauss, "True green laser diodes at 524 nm with 50 mw continuous wave output power on c -plane gan," *Appl. Phys. Expr.*, vol. 3(8), no. 6, p. 061 003, 2010.

[9] K. Okamoto, J. Kashiwagi, T. Tanaka, and M. Kubota, "Nonpolar m-plane ingan multiple quantum well laser diodes with a lasing wavelength of 499.8 nm," *Appl. Phys. Lett.*, vol. 94(7), no. 7, p. 071 105, 2009.

[10] K. KATAYAMA, N. SAGA, M. UENO, T. IKEGAMI, and T. NAKAMURA, "High-power true green laser diodes on semipolar gan substrates," *Electron. Comm. Jpn.*, vol. 98(5), no. 5, pp. 9–14,

[11] S. Jahangir, T. Frost, A. Hazari, L. Yan, E. Stark, T. LaMountain, J. M. Millunchick, B. S. Ooi, and P. Bhattacharya, "Small signal modulation characteristics of red-emitting (= 610nm) iii-nitride nanowire array lasers on (001) silicon," *Appl. Phys. Lett.*, vol. 106(7), no. 7, p. 071 108, 2015.

[12] K. Kishino, H. Sekiguchi, and A. Kikuchi, "Improved ti-mask selective-area growth (sag) by rf-plasma-assisted molecular beam epitaxy demonstrating extremely uniform gan nanocolumn arrays," *J. Cryst. Growth*, vol. 311(7), no. 7, pp. 2063 –2068, 2009.

[13] A. Bengoechea-Encabo, F. Barbagini, S. Fernandez-Garrido, J. Grandal, J. Ristic, M. Sanchez-Garcia, E. Calleja, U. Jahn, E. Luna, and A. Trampert, "Understanding the selective area growth of gan nanocolumns by mbe using ti nanomasks," *J. Cryst. Growth*, vol. 325(1), no. 1, pp. 89 –92, 2011.

[14] H. Sekiguchi, K. Kishino, and A. Kikuchi, "Ti-mask selective-area growth of gan by rf-plasma-assisted molecular-beam epitaxy for fabricating regularly arranged ingan/gan nanocolumns," *Appl. Phys. Expr.*, vol. 1(12), no. 12, p. 124 002, 2008.

[15] K. K. Hiroto Sekiguchi and A. Kikuchi, "Emission color control from blue to red with nanocolumn diameter of ingan/gan nanocolumn arrays grown on same substrate," *Applied Physics Letters*, vol. 96, no. 23, p. 231 104, 2010.

[16] K. Kishino, K. Nagashima, and K. Yamano, "Monolithic integration of ingan-based nanocolumn light-emitting diodes with different emission colors," *Appl. Phys. Expr.*, vol. 6(1), no. 1, p. 012 101, 2013.

[17] Y.-H. Ra, R. Wang, S. Y. Woo, M. Djavid, S. M. Sadaf, J. Lee, G. A. Botton, and Z. Mi, "Full-color single nanowire pixels for projection displays," *Nano Lett.*, vol. 16(7), no. 7, pp. 4608–4615, 2016.

[18] K. A. Bertness, A. W. Sanders, D. M. Rourke, T. E. Harvey, A. Roshko, J. B. Schlager, and N. A. Sanford, "Controlled nucleation of gan nanowires grown with molecular beam epitaxy," *Adv. Funct. Mater.*, vol. 20(17), no. 17, pp. 2911–2915, 2010.

[19] T. Gotschke, T. Schumann, F. Limbach, T. Stoica, and R. Calarco, "Influence of the adatom diffusion on selective growth of gan nanowire regular arrays," *Appl. Phys. Lett.*, vol. 98(10), no. 10, p. 103 102, 2011.

[20] K. Kishino, T. Hoshino, S. Ishizawa, and A. Kikuchi, "Selective-area growth of gan nanocolumns on titanium-mask-patterned silicon (111) substrates by rf-plasma-assisted molecular-beam epitaxy," *Electron. Lett.*, vol. 44(13), 819–821(2), 2008.

[21] R. Wang, Y.-H. Ra, Y. Wu, S. Zhao, H. P. T. Nguyen, I. Shih, and Z. Mi, "Tunable, full-color nanowire light emitting diode arrays monolithically integrated on si and sapphire," *Proc. SPIE*, vol. 9748, 97481S–97481S9–, 2016.

[22] H. P. T. Nguyen, M. Djavid, S. Y. Woo, X. Liu, A. T. Connie, S. Sadaf, Q. Wang, G. A. Botton, I. Shih, and Z. Mi, "Engineering the carrier dynamics of ingan nanowire white light-emitting diodes by distributed p-algan electron blocking layers," *Sci. Rep.*, vol. 5, no. 7744, p. 1, 2015.

[23] J. Qu, M. Lee, M. Hilke, and X. Liu, "Investigating the impact of sem chamber conditions and imaging parameters on contact resistance of in-situ nanoprobing," *Nanotechnology*, vol. 28(34), p. 345 702, 2017.

[24] A.Vila, F. F.Hernndez-Ramirez, J.Rodrguez, O. Casals, A.Romano-Rodrguez, J. Morante, and M. Abid, "Fabrication of metallic contacts to nanometre-sized materials using a focused ion beam (fib)," *Mater Sci Eng C*, vol. 26(5), no. 5, pp. 1063 –1066, 2006.

[25] G. D. Marzi, D. Iacopino, A. J. Quinn, and G. Redmond, "Probing intrinsic transport properties of single metal nanowires: direct-write contact formation using a focused ion beam," *J. Appl. Phys.*, vol. 96(6), no. 6, pp. 3458–3462, 2004.

[26] P. Mark and W. Helfrich, "Space-charge-limited currents in organic crystals," *J. Appl. Phys.*, vol. 33(1), no. 1, pp. 205–215, 1962.

[27] A. Rose, "Space-charge-limited currents in solids," *Phys. Rev.*, vol. 97(6), pp. 1538–1544, 1955.

[28] S. Sze, "Physics of semiconductor devices. 1969," *Interscience, NY: Wiley*, p. 42,

[29] F. Schwierz, "An electron mobility model for wurtzite gan," *Solid State Electron*, vol. 49(6), no. 6, pp. 889 –895, 2005.

[30] J. Zhao, J.-Q. Huang, F. Wei, and J. Zhu, "Mass transportation mechanism in electric-biased carbon nanotubes," *Nano Lett.*, vol. 10(11), no. 11, pp. 4309–4315, 2010.

[31] S Karim, K Maaz, G Ali, and W Ensinger, "Diameter dependent failure current density of gold nanowires," *Journal of Physics D: Applied Physics*, vol. 42, no. 18, p. 185 403, 2009.

[32] Y. Xia, P. Yang, Y. Sun, Y. Wu, B. Mayers, B. Gates, Y. Yin, F. Kim, and H. Yan, "One-dimensional nanostructures: synthesis, characterization, and applications," *Adv. Mater.*, vol. 15(5), no. 5, pp. 353–389,

[33] N. I. Kovtyukhova and T. E. Mallouk, "Nanowires as building blocks for self-assembling logic and memory circuits," *Chemistry ? A European Journal*, vol. 8, no. 19, pp. 4354–4363,

[34] F. A. Faria, J. Guo, P. Zhao, G. Li, P. K. Kandaswamy, M. Wistey, H. G. Xing, and D. Jena, "Ultra-low resistance ohmic contacts to gan with high si doping concentrations grown by molecular beam epitaxy," *Appl. Phys. Lett.*, vol. 101(3), no. 3, p. 032 109, 2012.

[35] S. I. Lopatin, V. L. Stolyarova, V. G. Sevast'yanov, P. Y. Nosatenko, V. V. Gorskii, D. V. Sevast'yanov, and N. T. Kuznetsov, "Determination of the saturation vapor pressure of silicon by knudsen cell mass spectrometry," *Russ. J Inorg. Chem.*, vol. 57(2), no. 2, pp. 219–225, 2012.

[36] J. V. Mantese and W. V. Alcini, "Platinum wire wedge bonding: a new ic and microsensor interconnect," *J Electron Mater.*, vol. 17(4), no. 4, pp. 285–289, 1988.

[37] K. N. Chen, A. Fan, C. S. Tan, and R. Reif, "Contact resistance measurement of bonded copper interconnects for three-dimensional integration technology," *IEEE Electr Device L*, vol. 25(1), no. 1, pp. 10–12, 2004.

[38] G. E. Moore, "Cramming more components onto integrated circuits, reprinted from electronics, volume 38, number 8, april 19, 1965, pp.114 ff.," *IEEE J. Solid-State Circuits*, vol. 11(3), no. 3, pp. 33–35, 2006.

[39] G. E. Moore, "Progress in digital integrated electronics [technical literaiture, copyright 1975 ieee. reprinted, with permission. technical digest. international electron devices meeting, ieee, 1975, pp. 11-13.]," *IEEE Solid-State Circuits Society Newsletter*, vol. 11, no. 3, pp. 36–37, 2006.

The connection between Chapter 5 and Chapter 6

In Chapter 5, the electrical properties of single n-i-n-n^+ GaN NWs grown on Si substrates were investigated through the developed SEM-based *in-situ* two-point electrical nanoprobing system. By tuning the Si-doping concentration of the n^+-GaN segment, we have achieved a NW breakdown current density of 4.65 MA/cm^2 and a breakdown power of 96.84 mW, both the highest among the previously reported results from GaN NWs.

In Chapter 6, in order to enable opto-electro-mechanical characterization in SEM, we extend the SEM-based *in-situ* two-point electrical nanoprobing system presented in Chapter 4 and 5, and develop the first multi-physical nanomaterial characterization system in SEM. Using this system, we will conduct optical photoluminescence (PL) and optoelectronic electroluminescence (EL) characterization of single InGaN/GaN nanowires (NWs). Besides, we will quantify, for the first-time, the effect of mechanical stress/strain on the EL property of single InGaN/GaN NWs. This will allow better understanding of the complex coupling-field properties of the single InGaN/GaN NWs for nanoelectronic and optoelectronic applications.

CHAPTER 6
Multi-physical Characterization of Single InGaN/GaN NWs in SEM

Multi-physical Characterization of Single InGaN/GaN NWs in SEM

Juntian Qu[1,2], Renjie Wang[3], Peng Pan[1,2], Yu Sun[1], Ishiang Shih[3], Zetian Mi[3,4*] and Xinyu Liu[1,2*]

[1]*Department of Mechanical and Industrial Engineering, University of Toronto, Toronto, ON, Canada, M5S 3G8*

[2]*Department of Mechanical Engineering, McGill University, Montreal, QC, Canada, H3A 0C3*

[3]*Department of Electrical and Computer Engineering, McGill University, Montreal, QC, Canada, H3A 0E9*

[4]*Department of Electrical Engineering and Computer Science, University of Michigan, Ann Arbor, MI, United States, 48109*

*Corresponding author: xyliu@mie.utoronto.ca.

To be submitted.

ABSTRACT: With the rapid advance of optical and optoelectronic nanodevices, the optical and optoelectronic characterization of nanostructures is becoming more and more popular, for the purpose of both devices performance improvement and revealing complicated underlying coupling-field properties. InGaN NWs have been widely used for optoelectronic applications such as ultrahigh-speed nanoscale lasers, photodetectors, and high-efficiency white light-emitting diodes (LEDs). These device applications usually require accurate optoelectronic characterization of InGaN nanowires (NWs). However, as an important characterization technique, optoelectronic characterization of one-dimensional nanomaterials inside a scanning electron microscope (SEM) is still underexplored, which is partially due to the technical challenge of integrating optical components inside the space-limited SEM chamber and achieving high-efficient optical excitation and measurement in the SEM environment. In this work, the first SEM-based multi-physical characterization system is developed. Using this system, the opto-electro-mechanical characterization

of single InGaN/GaN NWs is carried out, and the effect of mechanical strain/stress on the EL property of single InGaN/GaN nanowires is investigated for the first time.

Index Terms - Multi-physical characterization, scanning electron microscopy (SEM), Photoluminescence (PL), Electroluminescence (EL), and single InGaN/GaN nanowires.

6.1 Introduction

The last two decades have witnessed extensive research on nanomaterials because of their exceptional promise in science and technology. Due to their superior physical/chemical properties and unique nanoscale morphologies, one-dimensional (1D) nanostructures such as nanowires and nanotubes have been widely used for a variety of applications such as next-generation electronics [1], sustainable energy [2], and biosensing [3]. The mechanical, electrical, and optical properties of these nanomaterials play critical roles in their practical device applications, and the experimental determination of these properties is important from the perspective of both nanomaterial synthesis and application.

With the rapid advance of optical and optoelectronic nanodevices, the optical and optoelectronic characterization of nanostructures is becoming more and more popular, for the purposes of both foundational understanding of material properties and performance improvement of nanostructure-based devices. For instance, InGaN NWs have been widely used for optoelectronic applications such as ultrahigh-speed nanoscale lasers [4], photodetectors [5], and high-efficiency white light-emitting diodes (LEDs) [6]. These applications usually require accurate optoelectronic characterization of InGaN NWs. However, as an important characterization technique, optoelectronic characterization of one-dimensional nanomaterials inside a scanning electron microscope (SEM) is still underexplored. For optical characterization, only a few studies on cathodoluminescence (CL) characterization of nanomaterials [7, 8, 9, 10] were carried out in SEM. While for field-coupling optoelectronic characterization, SEM was only utilized for focused ion beam (FIB)-assisted metal contact deposition [11], the major characterization processes were still performed in ambient environment. The lack of SEM-based optical characterization is mainly attributed to the limited space of SEM chamber, which leads to the challenge of integrating optical components such as sizeable paraboloidal mirror for effective light collection [12].

To perform optical characterization in SEM, efficient light collection and detection are necessary. A sizeable paraboloidal mirror was employed in an SEM setup [12] for light collection in a CL test; however, due to the limited space of the SEM chamber, the mirror blocked most other

detectors and did not allow electrical nanoprobe integration, thus hindering the simultaneous measurement of electrical and optical properties of nanomaterials. To address this issue, space-saving optical microfibers [10] were integrated into the SEM chamber for *in-situ* optical characterization of individual semiconductor nanostructures, but the experimental setup does not have force sensing to quantify the contact forces applied to the nanostructures for investigating the mechanical effect on the material's optoelectronic properties.

Besides, electrical contacts are usually established prior to the optoelectronic characterization of nanomaterials, either by means of electrodes patterning or *in-situ* nanoprobing. The contact resistance between an electrode/nanoprobe and a nanometer-sized sample could significantly affect the measured optoelectronic properties; therefore, it is highly desired to minimize the contact resistance during optoelectronic characterization of nanomaterials. Besides, conventional nanolithography methods for patterning electrodes on a sample involves chemical treatment of the sample that may alter its optoelectronic properties [13, 14]. In a previous study, we have reported the systematic investigation on effect of experimental conditions of SEM-based, two-point nanoprobing on the probe-sample contact resistance, and demonstrated how to experimentally reduce the contact resistance for in-situ nanomaterial probing without requiring metal electrode patterning [15].

This work aims at developing a SEM-based nanomanipulation system for multi-physical characterization of 1D nanomaterials. To my best knowledge, this will be the first SEM-based nanomanipulation system capable of opto-electro-mechanical characterization of nanomaterials. Using this system, we characterize the photoluminescence (PL) and electroluminescence (EL) properties of single InGaN/GaN nanowires (NWs), and also examine, for the first-time, the effect of mechanical stress/strain on the EL property of single InGaN/GaN nanowires. The developed nanomanipulation system will greatly facilitate the experimental characterization of multi-physical properties of semiconductor nanomaterials and nanostructures, and potentially lead to (opto)electronic devices with improved performance.

6.2 Development of the SEM-based Multi-physical Characterization System

As schematically shown in Figure 6–1(a), the developed SEM-based nanomanipulation system includes a field-effect SEM (SU3500, Hitachi) and a nanomanipulator (LF-2000, Toronto Nanoinstrumentation Inc.) with four nanopositioners mounted inside the SEM. One Pt-coating tungsten conductive nanoprobe (ST-20-0.5, GGB Industries), one Pt-coating conductive atomic force microscope (AFM) cantilever probe with a protruding tip (ATEC-FM, NanoAndMore Corp.), and two optical micro-fibers (Accu-Glass Products Inc.) are mounted on the four nanopositioners, respectively, with the nanoprobe and AFM cantilever probe arranged along one diagonal direction and the two optical micor-fibers facing along the other diagonal direction.

The developed nanomanipulation system contains necessary components for operation in three individual single-field characterization modules: (i) the electrical characterization module, (ii) the optical characterization module, and (iii) the mechanical characterization module. With the seamless integration of these components and the development of the corresponding techniques, the system is also capable of executing coupled-field nanomaterial characterization tasks including electroluminescence (EL) and opto-electro-mechanical characterization.

The Pt-coating tungsten conductive nanoprobe and protruding AFM cantilever probe can be used for *in-situ* electrical nanoprobing of nanomaterials such as the as-grown single NWs. Owing to its visible tip from the SEM top view, the pure top-view SEM vision can guide the protruding AFM cantilever probe to contact with the top surface of a single NW, without requiring the SEM sample stage to be tilted for side view of the probe and sample. For applying an electrical voltage/current to a NW sample, our system adopts *in-situ* two-point electrical nanoprobing rather than the conventional EBL-patterned electrode contacts, which avoids any chemical treatment of the NW sample during EBL [13, 14]. Through SEM vision guidance, the two optical micro-fibers can be precisely positioned to the proximity of a single NW for optical excitation and emission measurement, just like the classical photoluminescence (PL) measurement setup. Besides, the protruding AFM probe can also serve as a high-resolution force sensor for mechanical force measurement during nanoprobing, which, in combination with the SEM-vision-based displacement

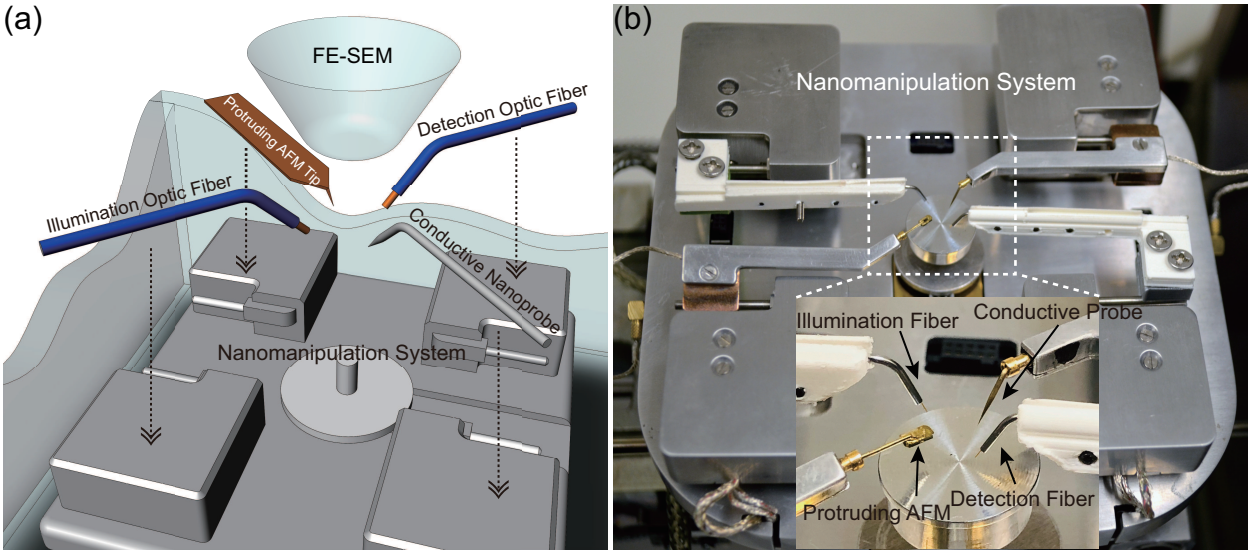

Figure 6–1: Multi-physical characterization system. (a) Schematic figure. (b) Multi-physical end-effectors integration onto nanomanipulation system.

measurement, enables mechanical characterization and stimulation (by applying strain/stress) of single NWs. The force sensing methodology based on the AFM cantilever probe will be presented in Section 6.2.2. Figure 6–1(b) shows the photos of the two conductive probes and two optical micro-fibers mounted on the four nanopositioners.

The major merit of this multi-physical characterization system is the flexibility of combining different types of end-effectors for different tasks: by adopting the two optical micro-fibers, we can perform PL characterization of nanomaterials. By combining both the emission measurement micro-fiber and the two conductive probes, we can perform optoelectronic (i.e., EL) characterization of a single NW, where the injection current can be applied to the NW using the two conductive probes and the resulting optical emission can be simultaneously measured by the optical micro-fiber. Moreover, this system can also be extended to triple-coupled-field characterization (opto-electro-mechanical characterization), in which a single semiconductor NW can be compressed by the AFM probe from the top and the effect of the induced mechanical stress/strain on EL property of the NW quantified by the two conductive probes and the emission measurement optical micro-fiber. In this operation, the conductive AFM probe serves as both the electrical nanoprobe and the force-sensing end-effector.

In the following sections, we will introduce the optical and mechanical characterization modules of the nanomanipulation system and characterize their performance. The electrical characterization module has been described previously during an *in-situ* two-point nanoprobing experiment [15].

6.2.1 Optical Characterization Module

The design of the optical characterization module in SEM takes advantage of space-saving optical micro-fibers instead of sizeable paraboloidal mirror for light excitation and material emission detection. Figure 6–2(a) shows the schematic diagram of the SEM-based optical characterization module. A 405nm collimated diode laser (LRD-0405-PFR-00500-05, Laserglow Technologies) was chosen as the optical excitation source, and the laser beam was guided into SEM chamber through two multimode optical micro-fibers: one 100 μm UV/VIS bare polished fiber (112550, Accu-Glass Products Inc.) inside the SEM vacuum chamber (vacuum side) and another 100 μm UV/VIS PMMA-encapsulated fiber (112552, Accu-Glass Products Inc.) outside the SEM chamber (air side). A customized vacuum feedthrough was mounted on a port of the SEM chamber for connecting the two micro-fibers and coupling the laser beam from outside to inside of the chamber. To protect the fragile thin bare micro-fiber in the SEM chamber, a soft tube of 150 μm inner diameter (ID) was utilized to sheath the vacuum-side bare fiber. Finally, to complete the excitation loop setup, a 405 nm bandpass filter (OD4, Edmund Optics) was set in the path of air-side micro-fiber for purifying the excitation signal.

To detect the optical emission from a nano-sample, two optical micro-fibers of the same type (wavelength range: 200-800 nm) were selected for mounting at both the air and vacuum sides of the SEM. The selection of the visible wavelength range meets the requirement of photo- and electroluminescence measurements of the InGaN/GaN NWs. Another customized vacuum feedthrough was mounted on the same port as the excitation micro-fiber feedthrough for connecting the two emission measurement micro-fibers. The end of air-side micro-fiber was connected with a high-precision spectrometer (Ocean Optics, QE Pro-FL) with a back-thinned, TE-cooled CCD detector for luminescence measurement. To isolate the detected luminescence signal from the 405

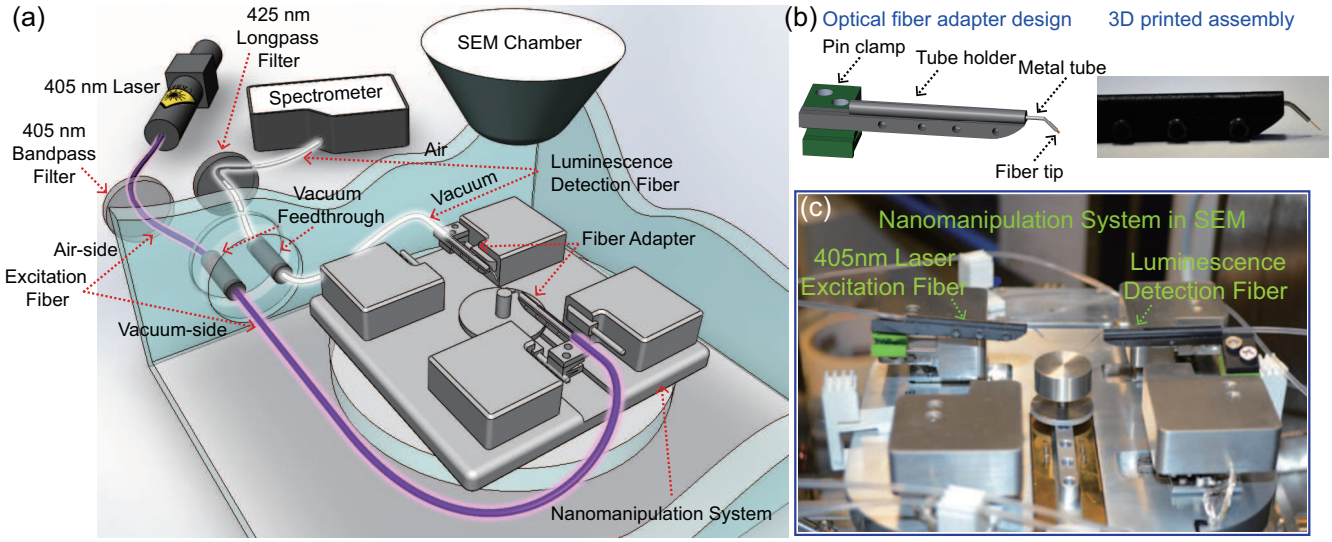

Figure 6–2: SEM-based optical characterization module. (a) Schematic figure. (b) Photograph of optical fiber adapter. (c) Photograph of optical characterization module with integrated dual optical fibers.

nm excitation signal, a 425 nm longpass filter (OD4, Edmund Optics) was placed in the air-side detection path for filtering out any 405 nm signal.

A technical challenge for integration of the optical characterization module is how to mount the two soft flexible bare micro-fiber tips onto the nanopositioner and achieve fixed light excitation and detection angles. As shown in Figure 6–2(b), we designed an optical micro-fiber adapter to stably mount the bare micro-fiber onto the nanopositioner: the soft flexible optical fiber tip was firstly inserted into a customized metal tube with a 45° bending angle, and the metal tube was then inserted into the 150 μm ID protection tube. A 3D-printed tube holder was fabricated to immobilize the protection tube, and a customized pin clamp was finally 3D printed for connecting the tube holder and fixing it onto the metal pin of the nanopositioner with adequate gripping force. This adapter design provides stable mounting of the two micro-fibers onto the two nanopositioners, and also allows the micro-fiber position and bending angle to be readily adjusted by changing the clamp position on the metal pin of the nanopositioner and the bending angle of the metal tube, respectively. Figure 6–2(b) shows the photograph of the assembly of the fiber adapter, and

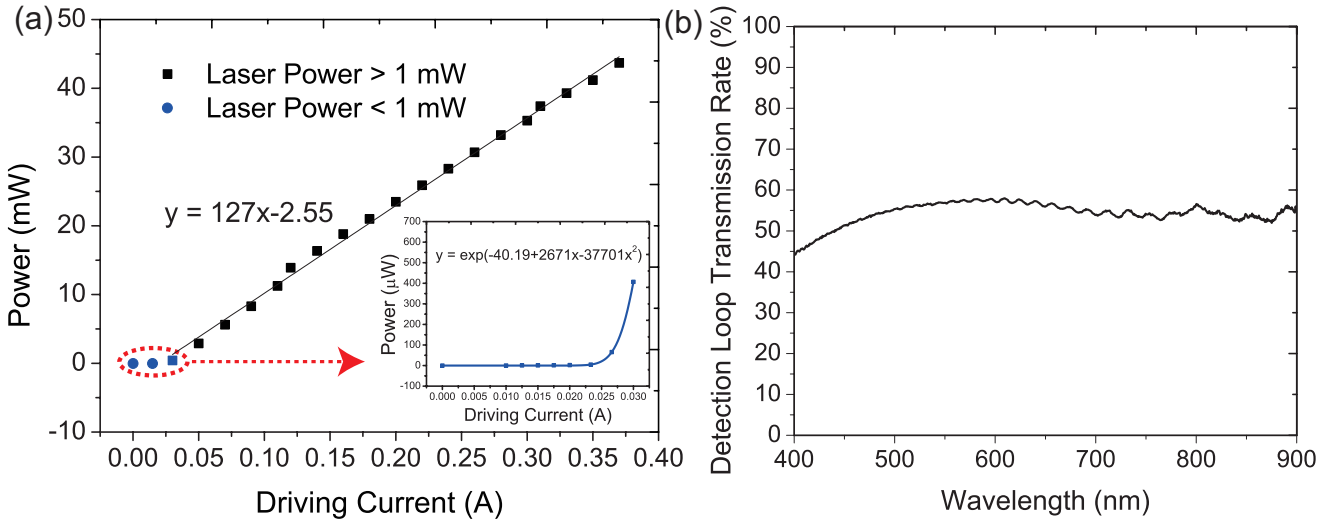

Figure 6–3: Optical characterization module calibrations. (a) Illumination power. (b) Luminescence detection loop transmission rate.

Figure 6–2(c) shows the laser excitation micro-fiber and luminescence detection micro-fiber stably mounted on the nanomanipulation system.

6.2.1.1 Calibrations of Optical Characterization Module

To better quantify the illumination power in the laser excitation loop, we performed calibrations between the driving current of the laser source and the detected total power at the excitation micro-fiber tip, which is the direct input and the output of the excitation loop. A digital optical power meter (PM100D, Thorlabs) with 200-1000 nm photodiode power sensors (S120VC, Thorlabs) was utilized for this task, the sensing probe covered the whole excitation fiber tip to minimize the energy loss during the measurement. The calibration curve of the illumination power is shown in Figure 6–3(a). One can observe a dead zone in the driving current range of less than 0.024 A, beyond which the laser power and driving current have a nonlinear correlation until 0.03 A. For current over 0.03 A, the output laser power is linear proportional to the driving current. The maximum detected laser power is 43.7 mW at the driving current of 0.37 A, which is the highest achievable excitation power of the optical characterization module. The excitation power calibration result can provide guideline data for studies such as illumination power-dependent PL characterization of nanomaterials.

In the luminescence detection loop, there is transmission loss existing in the coupling processes between air-side/vacuum-side optical fibers and the vacuum feedthrough, to derive the original luminescence intensity at the detection fiber tip inside SEM chamber, we performed a calibration for detection loop transmission rate using a broad range tungsten halogen source (HL-2000, Ocean Optics) and the QE-Pro spectrometer, where light is coupled into the detection optical fiber (inside SEM chamber) and the transmitted remaining light is detected at the other end outside chamber, the transmission rate in the wavelength range of 400-900 nm is plotted in Figure 6–3(b), we can see the rate is over 50% in the wavelength range of 450-900 nm, considering multi-components and light coupling processes (also fiber bending will leads to transmission loss), the derived transmission rate for detection loop is acceptable. To note that, in some characterization, normalized PL and EL spectrums are usually required, so people are not caring about the relative luminescence intensity between different spectrums, but in some scenarios where relative luminescence intensity is compared between different spectrums, the calibration result in Figure 6–3(b) may provide important look-up information to calculate the original luminescence intensity in SEM chamber.

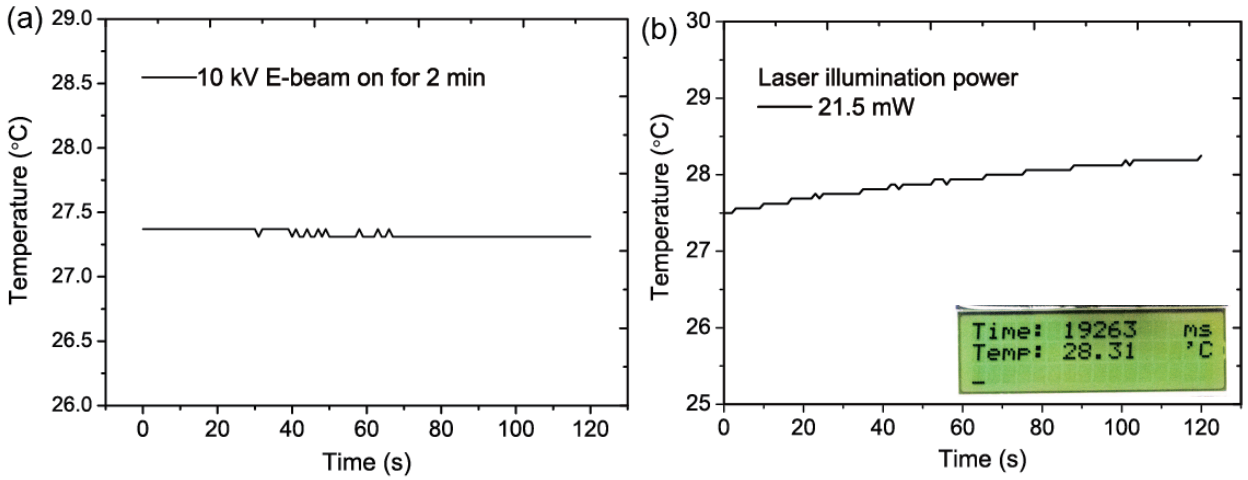

Figure 6–4: Temperature calibrations. (a) E-beam irradiation impact. (b) Laser illumination impact. Inset: LED display of real-time temperature monitering.

As temperature is a crucial factor for the optoelectronic properties of some nanomaterials, we have also calibrated the temperature change induced by electron-beam and laser illumination in the inclosed SEM vacuum chamber, by integrating an digital temperature sensor (TMP 102,

Sparkfun Electronics) onto the nanomanipulation system. As shown in the Figure 6–4(a), the electron-beam of SEM shows no obvious impact on the vacuum chamber temperature for 2 min continuous irradiation. Figure 6–4(b) presents the temperature status during 2 min continuous laser illumination, due to slower thermal diffusion rate in the inclosed vacuum chamber compared to ambient environment, we can observe around 0.5 °C temperature rise after 2 min continuous laser illumination (with maximum adopted power of 21.5 mW in photoluminescence measurement in Section 6.3.2). As the photoluminescence signal is usually recorded within 1 min, and temperature variation less than 0.5 °C won't affect the accuracy of photoluminescence measurement, so this calibration result has demonstrated neglectable impact on the chamber temperature by the laser illumination. All the following photoluminescence characterization was performed under room temperature.

6.2.2 Mechanical Characterization Module

To investigate the mechanical impact on the optical or optoelectronic property of nanomaterials, the mechanical characterization module should be able to apply different levels of quantified force on nanomaterials, and the optical emission signal should be simultaneously collected by the optical characterization module. In this section, we will describe the mechanical characterization module of the multi-physical characterization system, as well as the force sensing methodology for accurate quantification of applied force on single NWs (for further experiments on single InGaN/GaN NW).

Due to the protruding tip of the conductive AFM probe as shown in Figure 6–1, the tip is visible from the SEM top view (see its top-view photograph in Table 6–1) and the tip-NW contact is much easier for observation (than a conventional AFM tip that hides beneath the cantilever beam) during the force applying process. Thus, it is convenient for verification of stable contact between the tip and the NW top surface. The protruding AFM tip serves as the mechanical end-effector and contact force sensor.

The protruding AFM probe, as shown in Figure 6–1, was integrated to one of the nanopositioner with nanometer-sized positioning resolution in three degree of freedom (DOF). To obtain

the force on single NWs applied by the AFM tip, the cantilever beam deflection needs to be detected. However, from the SEM top view, the cantilever beam deflection cannot be visualized. In order to visually measure the cantilever beam deflection, we mounted the NW sample onto a 90° tilt holder. For better visualizing the probe tip-NW contact, the SEM stage was tilted at 10°. Equivalently, the NWs sample was tilted at 80° relative to the original horizontal plane. With the tilt setup, a customized protocol was developed to calculate the applied force on the top surface of a single NW, which includes three steps: (i) vision-based tracking of cantilever beam deflection, (ii) stiffness tilt correction, and (iii) longitudinal torque correction.

6.2.2.1 Vision-based Tracking of Cantilever Beam Deflection

During nanoprobing of a NW, the AFM cantilever beam deflection is defined as the displacement difference between AFM tip and the root of cantilever beam. As the cantilever root is firmly connected with the nanopositioner, its displacement can be read out as the displacement of the nanopositioner, Z. Therefore, we only need to track the AFM tip displacement in order to obtain the AFM beam deflection. At the tilt angle of 80°, we can track the AFM tip motion using an image processing algorithm as shown in Figure 6–5(b), and the detected tip displacement is denoted as z_0. We denote the tip displacement normal to the cantilever beam axis as $z_0^{'}$; thus, $z_0^{'} = z_0/\sin 80°$. Then the cantilever beam deflection Δz can be calculated as $\Delta z = Z - z_0^{'}$. The whole flow of deriving cantilever beam deflection is depicted in Figure 6–5(a).

6.2.2.2 Stiffness Tilt Correction

After deriving the cantilever beam deflection, in order to accurately quantify the force of AFM tip, it is necessary to accurately calibrate the stiffness of the cantilever. In the mechanical characterization module, the AFM cantilever was inclined at 13° to allow its tip to access the sample top surface without letting the cantilever holder contact the sample substrate. Since the tilt of the cantilever will affect the effective stiffness of the cantilever in the AFM, the AFM cantilever stiffness in the tilt setup should be determined accurately [16].

The relationship between cantilever effective stiffness and the inclined angle (denoted as θ) has been experimentally verified in a previous study using a microfabricated AFM cantilever [16].

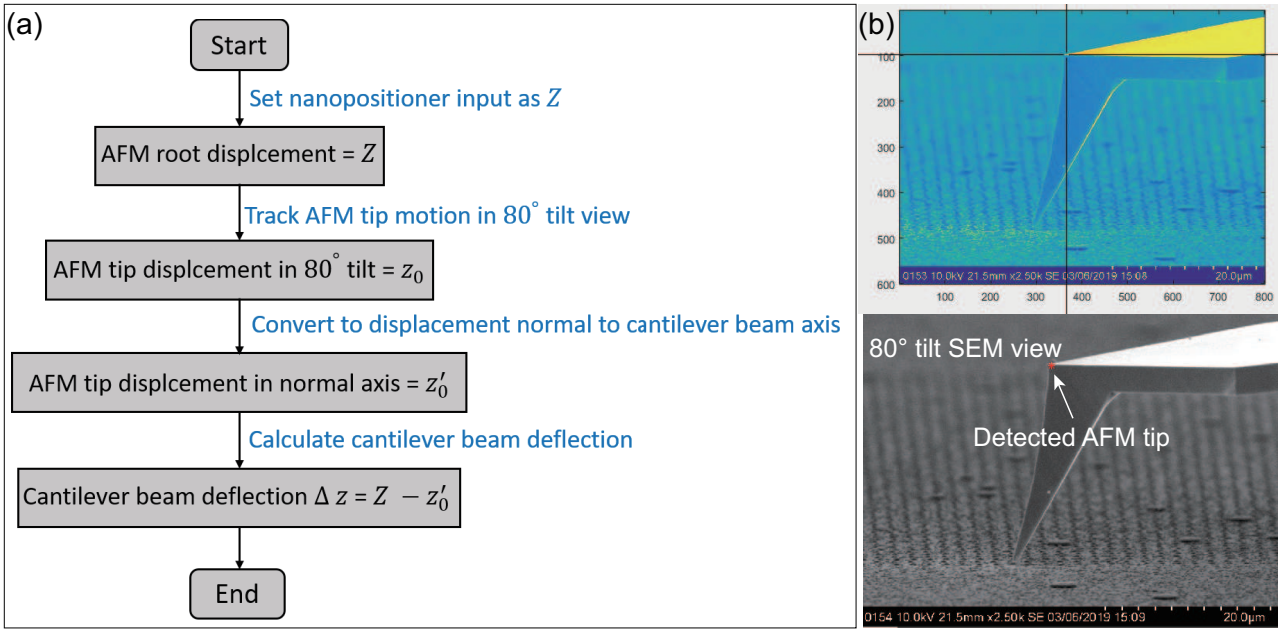

Figure 6–5: Vision-based Tracking of Cantilever Beam Deflection. (a) Flow diagram. (b) Vision tracking of AFM tip motion in 80 ° tilting plane.

The effective stiffness was determined to be $k_z = k_c / \cos^2\theta$, where k_c is the intrinsic stiffness perpendicular to the long axis of the cantilever. Detailed illustrations can be referred to Table 6–1, which shows the geometry of standard AFM tip and adopted protruding AFM tip.

To calibrate the intrinsic stiffness k_c, the thermal tune method, based on measuring thermal noise, provides an automated and quick determination of cantilever spring constant. Firstly, the cantilever deflection sensitivity was calibrated as 41.67 nm/V using a commercial AFM (Bioscope Resolve, Bruker), as shown in Figure 6–6(a). A power spectral density (PSD) plot of the cantilever response to ambient conditions is displayed in Figure 6–6(b). The data were fitted using the Lorentzian (Air) model to derive the intrinsic stiffness of the AFM cantilever to be 2.4178 N/m. The effective stiffness of protruding AFM cantilever was finally calculated to be 2.546 N/m based on the obtained intrinsic stiffness value, as shown in the "Stiffness Correction" column of Table 6–1.

Table 6–1: Illustration Table for Stiffness Tilt and Longitudinal Torque Corrections.

	AFM Cantilever Geometry	Stiffness Correction	Torque Correction
Standard AFM Tip	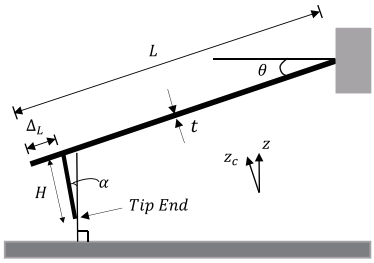 • **L**: Cantilever length • **t**: Cantilever beam thickness • Δ_L: Position of tip attachment point • **θ**: Angle between cantilever axis and sample surface • **α**: Angle between tip-cantilever line and the direction perpendicular to sample surface • **H**: Tip length • ***z*-axis:** Perpendicular to sample surface • z_c***-axis:*** Normal to cantilever	• F_z: Force applied to single NW • Δ_z: Cantilever beam deflection • k_c: Intrinsic spring constant, fundamental stiffness perpendicular to the long axis of the cantilever • k_z: Effective cantilever stiffness perpendicular to the horizontal sample surface. ⇩ $k_z = \frac{k_c}{cos^2\theta}$	• T_z: Torque correction perpendicular to sample • k_c : Intrinsic stiffness of cantilever $k_c = \frac{Ewt^3}{4L^3}$ • $k_{z\theta}$: Spring constant relating to longitudinal torque $k_{z\theta} = \frac{Ewt^3}{6L^3}$ ⇩ $T_z = (1\text{-}H\frac{k_c}{k_{z\theta}}\frac{\sin\alpha}{\cos\theta})^{-1}$
Protruding AFM Tip	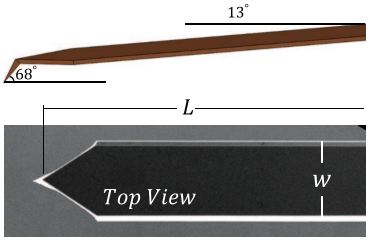 • $L = 240\ \mu m$ • $w = 35\ \mu m$ • $\theta = 13^\circ$ • $t = 3\ \mu m$ • $\Delta_L = 0$ • $\alpha = 22^\circ$ • $H = 10.8\ \mu m$	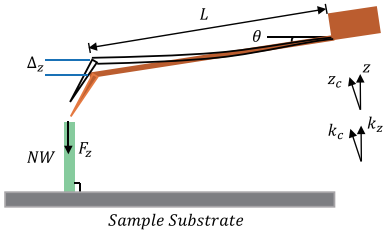 $k_z = \frac{k_c}{cos^2\theta} = \frac{2.4178}{cos^2 13^\circ} = 2.546$ N/m	$\frac{k_c}{k_{z\theta}} = \frac{3}{2L}$ $\frac{\sin\alpha}{\cos\theta} = 0.3844$ $T_z = 1.027$

6.2.2.3 Torque Correction

According to a general theoretical model [17], we can derive the applied AFM tip force (F_z in Table 6–1) normal to the sample surface to be $F_z = k_z \Delta z T_z$, where k_z is the effective cantilever stiffness normal to the sample surface, Δz the obtained cantilever deflection, T_z the induced AFM tip torque correction factor in the presence of cantilever tilt [17]. Detailed expression of T_z can be referred to the "Torque Correction" column of Table 6–1. Specifically, for our adopted protruding AFM tip, the torque correction T_z was calculated to be 1.027.

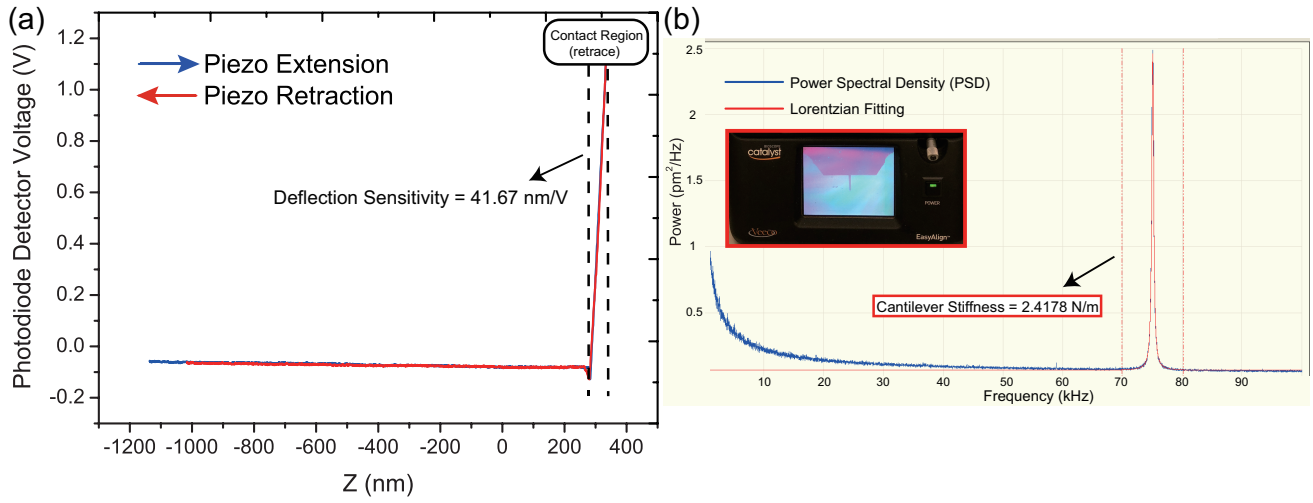

Figure 6–6: Thermal tune determination of intrinsic stiffness. (a) Determination of deflection sensitivity. (b) The power spectral density (PSD) plot of the cantilever response to ambient conditions.

6.3 Optical Characterization of Single InGaN/GaN NWs

As a contactless and nondestructive method of probing the electronic structure of nanomaterials, photoluminescence (PL) characterization has been an indispensable method in optical characterization of nanomaterials such as the InGaN/GaN NWs. In this section, we apply the optical characterization module to PL characterization of single InGaN/GaN NWs to demonstrate its effectiveness.

6.3.1 Epitaxial Growth of Nanowires

We have fabricated single InGaN/GaN quantum dot (QD) NWs with diameters from 220 nm to 280 nm on a Si substrate by selective area epitaxy (SAE) using a radio frequency plasma-assisted molecular beam epitaxy system (PA-MBE). The epitaxy took place on an arsenic doped n-type Si substrate with a 10 nm Ti layer as the growth mask [18, 19]. Opening sizes in the range of 220 nm to 280 nm were created on the Ti mask using EBL and reactive ion etching, and the opening size precisely controlled the NW diameter.

As schematically shown in Figure 6–7(a), each NW consists of $\sim$ 0.45 μm n-type Si-doped GaN segment, six vertically aligned InGaN/GaN (4 nm/4 nm) quantum dots and $\sim$ 0.15 μm p-type Mg-doped GaN segment. These NWs were grown using a Veeco GENxplor MBE system.

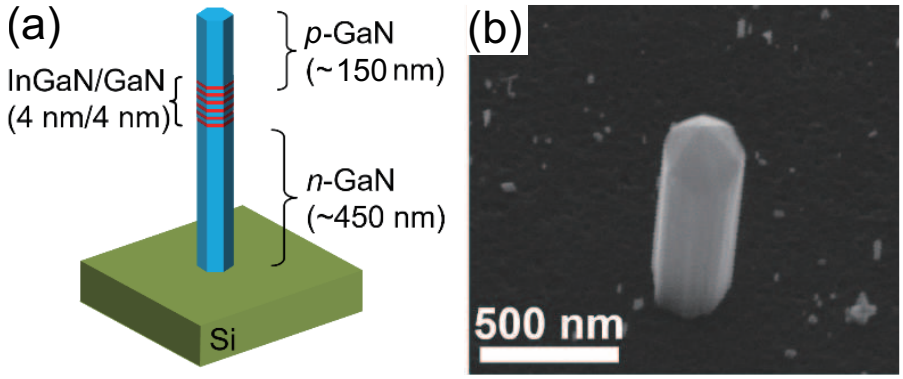

Figure 6–7: Sample for PL test. (a) Schematic of a single InGaN/GaN quantum-dot-nanowire structure grown on GaN template on Si substrate. (b) 45° tilt SEM image of single InGaN/GaN nanowires with diameter of 251 nm.

Figure 6–7(b) shows the field-emission scanning electron microscopy (SEM) image (45° tilt view) of the single nanowire structures grown with diameter of 251 nm. The nanowires exhibit hexagonal morphology and possess Ga-polarity based on the terminating facets.

6.3.2 Photoluminescence (PL) Characterization of Single InGaN/GaN NWs

Figure 6–8(a) shows the SEM photograph of the two micro-fibers pointing to a single InGaN/GaN NW for PL measurement. The PL emission from the InGaN/GaN NW was measured using the developed optical characterization module at room temperature. The illumination micro-fiber was connected with a 405 nm laser source, and the other micro-fiber connected with spectrometer was employed for detecting luminescence and was positioned to the proximity of single NWs covering the whole external surface of NWs. As shown in the inset of Figure 6–8(a), single InGaN/GaN NWs grown between two straight-slot-shape markers on Si substrate was used for PL measurement. The large gap between two adjacent NWs ensured the PL measurement from a single NW and avoids any optical crosstalk between NWs.

The PL emission spectra for four single NWs with different diameters are shown in Figure 6–8(b). NWs in each group were grown on the same Si substrate with identical epitaxy conditions, except that their lateral sizes (also referred to as diameters in the subsequent text) were varied in the range of 220 nm to 280 nm. It is seen that the optical emission shows a consistent blueshift

with increasing NW diameter under identical epitaxy conditions, the emission wavelength continuously varied from 645 to 627 nm by increasing the nanowire diameters from 220 nm to 271 nm. This phenomenon of size-dependent optical emission from single NWs can be well explained by a previously reported mechanism [20]. It was found that the In incorporation decreased from lateral diffusion with the increased NW diameter, leading to shorter emission wavelengths accordingly.

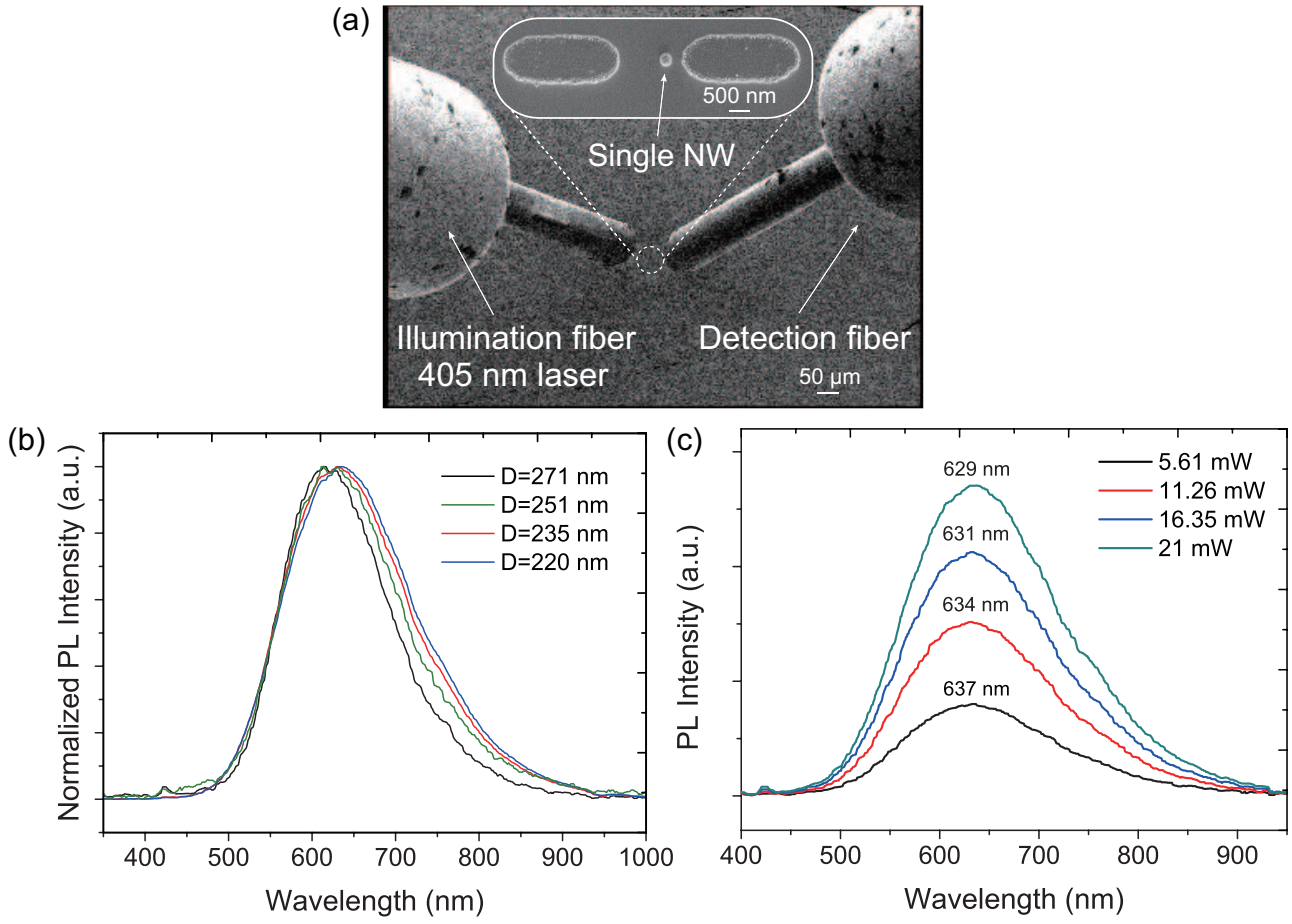

Figure 6–8: PL characterization of single InGaN/GaN NWs. (a) SEM picture of experimental setup. (b) PL emission spectra as a function of NWs diameter. Top Inset: magnified view of single InGaN/GaN NWs grown on Si substrate between two straight-slot-shape markers. (c) PL emission spectra as a function of illumination power, for single NW with diameter of 220 nm.

The PL emission spectra as a function of illumination power is shown in Figure 6–8(c), for a specific single NWs with diameter of 220 nm, the illumination power was calculated based on the calibration result shown in Figure 6–3(a). The spectral peak shows a blueshift from 637 nm to 629 nm with increasing illumination power from 5.61 mW to 21 mW, due to the state filling effect.

6.4 Optoelectronic Characterization of Single InGaN/GaN NWs

In this section, we performed EL characterization of single InGaN/GaN NWs. This can be achieved by combining the electrical and optical characterization modules. The protruding AFM cantilever probe and conductive nanoprobe were utilized for two-point electrical probing of single InGaN/GaN NWs and injection of electric current into it. In the meanwhile, the emission measurement micro-fiber was employed for detecting the EL emission from single NWs.

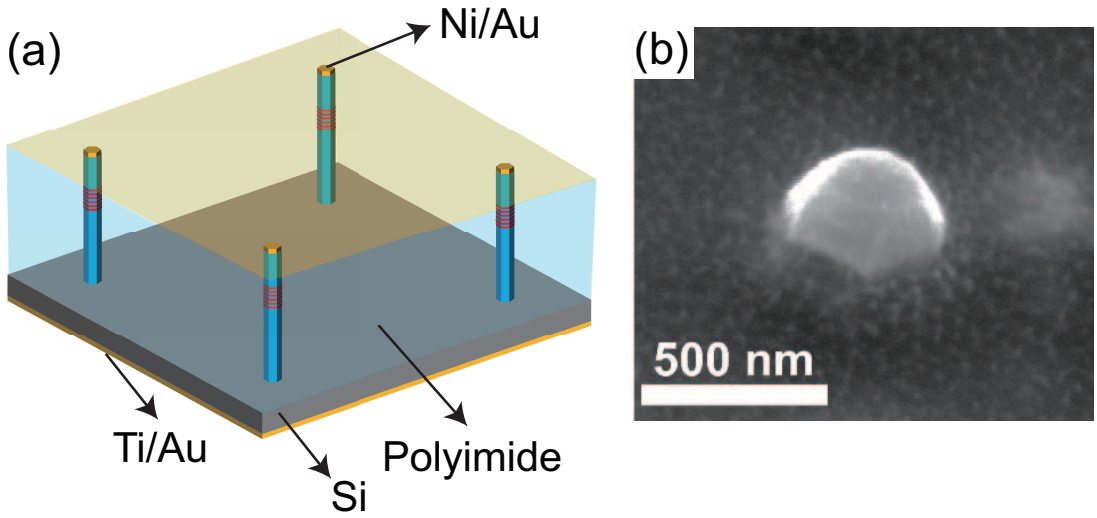

Figure 6–9: Sample for EL test. (a) Schematic of a single InGaN/GaN NW LEDs on Si substrate. (b) Top-view SEM image of the exposed p-GaN nanowire top-surface after polyimide passivation and dry etching.

6.4.1 Electrical Device Fabrication

To realize characterizing different diameters single InGaN/GaN NWs integrated on the same Si chip, we have designed single nanowire LED arrays consisting with varying diameters. The single NW LED consists of $\sim$ 0.45 μm n-GaN, six InGaN/GaN quantum dots, and $\sim$ 0.15 μm p-GaN. These samples were grown in a Veeco MBE system. Under the optimum growth conditions in the same Veeco MBE system, emission wavelengths across nearly the entire visible spectral range can be realized on Si substrate for NWs with diameters varying from $\sim$ 200 nm to $\sim$ 600 nm. The NWs have an average height $\sim$ 650 nm, with near-perfect hexagonal morphology and smooth lateral surface. This contributes to the enhanced light emission from the NW top surface.

As schematically shown in Figure 6–9(a), single InGaN/GaN NW LEDs were fabricated on a single chip. First, a Ti (20 nm)/Au (100 nm) n-metal contact was deposited at the backside of Si substrate and then annealed at $\sim$ 500 °C for 1 min in nitrogen ambient. A polyimide resist layer was spin-coated to fully cover the nanowires, followed by oxygen plasma etching to reveal the top surface of nanowires, as shown in Figure 6–9(b). Metal electrodes consisting of Ni (10 nm)/Au (10 nm) metal layers were then deposited on the p-GaN top surface of single NWs using e-beam evaporation and then annealed at $\sim$ 500 °C for 1 min in nitrogen ambient.

6.4.2 Electroluminescence (EL) Characterization of Single InGaN/GaN NWs

6.4.2.1 Current-Voltage Characterization

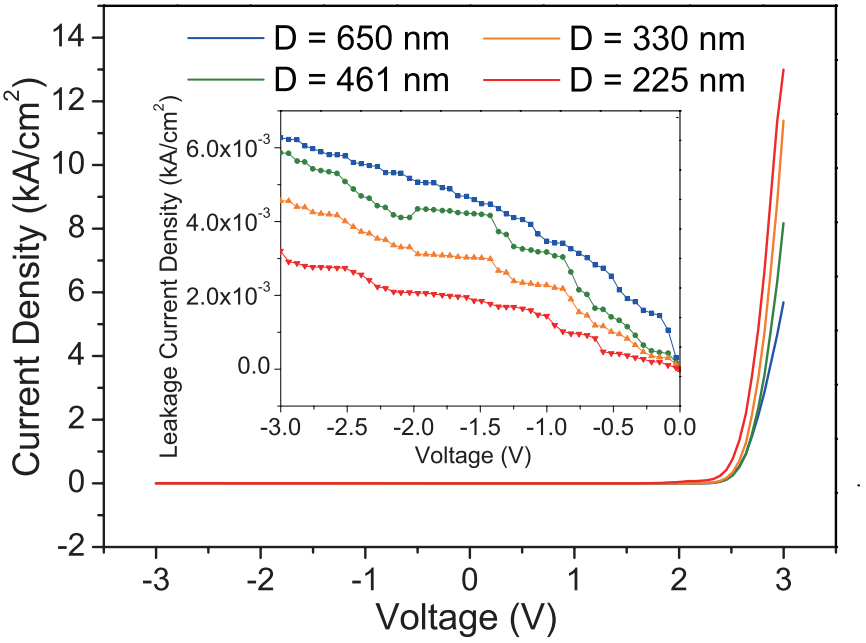

Figure 6–10: Current-voltage characteristics of single InGaN/GaN NWs with different diameters. Inset: leakage current density vs voltage.

Before performing EL characterization, electrical current-voltage properties of single InGaN/GaN NWs was characterized using developed SEM-based electrical characterization module, to obtain the allowable current injection range for single InGaN/GaN NWs and evaluate the current leakage level of single NWs under reverse bias.

The I-V characteristics of single InGaN/GaN NWs were measured under sweeping voltage signal from -3V to 3V with a step increment of 0.06 V and a ramp rate of 100 V/s at room temperature. During the measurement, the e-beam radiation from the SEM was switched off using a beam blanker to avoid any electrical noise induced by the incident electrons. In addition, before each measurement, the protruding AFM probe connecting the top surface of InGaN/GaN NWs was first grounded to eliminate any charge built-up on the sample due to SEM imaging.

Figure 6–10 shows representative I-V curves of single InGaN/GaN NWs emitting devices with four varied diameters, which exhibit excellent current-voltage (I-V) characteristics. The nanowire LEDs have turn-on voltages $\sim$ 2.5 V, which is better than previously reported values (3-3.5 V) in ensemble nanowire LEDs [21] and GaN-based planar devices [22].

Current densities as high as 12.99 kA/cm^2 (D $\sim$ 225 nm) were measured at $\sim$ 3 V, which is higher than the reported 6.15 kA/cm^2 [20] for single NWs on sapphire substrate, possibly due to the higher conductivity and thermal conductivity of Si substrate than GaN/sapphire substrate. From Figure 6–11 we can conclude that to our best knowledge, in recent eight years' reported works [23, 24, 25, 26, 20, 27, 28] regarding current density of single GaN-based NWs, our derived current density (12.99 kA/cm^2) is the highest value. Also, from the I-V characteristics, it is noticed that NWs with smaller diameter can sustain higher current density than NWs with lager diameters (12.99 kA/cm^2 for D $\sim$ 225 nm, 11.39 kA/cm^2 for D $\sim$ 330 nm, 8.17 kA/cm^2 for D $\sim$ 461 nm, 6.50 kA/cm^2 for D $\sim$ 650 nm, measured at $\sim$ 3 V), which is attributed to enhanced dopant incorporation in smaller diameter NWs [20] and the resulting efficient current conduction [29, 30], as well as the more efficient heat dissipation [21].

As shown in the inset of Figure 6–10, it can be noticed that the leakage current under reverse bias is relatively small but increases with increasing nanowire diameter (3.21×10^{-3} kA/cm^2 for D $\sim$ 225nm, 4.56×10^{-3} kA/cm^2 for D $\sim$ 330nm, 5.86×10^{-3} kA/cm^2 for D $\sim$ 461nm, 6.27×10^{-3} kA/cm^2 for D $\sim$ 650nm), which is likely due to the presence of defects in large diameter NWs and the resulting current leakage. Better leakage current level (3.21×10^{-3} kA/cm^2 to 6.27×10^{-3} kA/cm^2) has been achieved compared with previous studies (slightly over 10^{-2} kA/cm^2) [20].

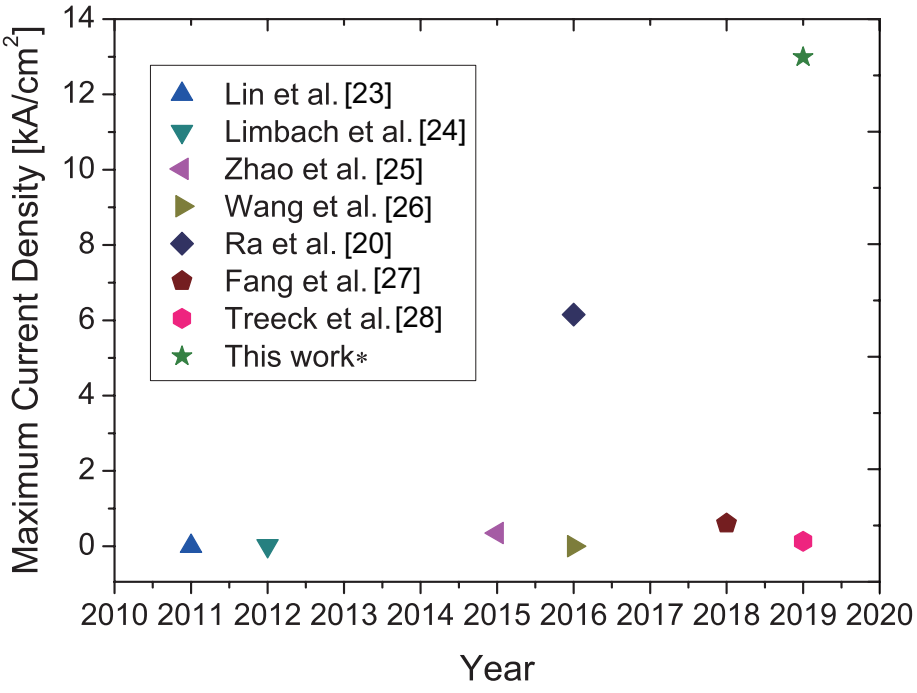

Figure 6–11: Comparison of maximum current density of single GaN-based NWs in recent eight years [23, 24, 25, 26, 20, 27, 28].

6.4.2.2 EL Characterization

Single InGaN/GaN NWs LEDs can also exhibit excellent light emission characteristics. Figure 6–12(a) shows the SEM picture of EL characterization experimental setup. The conductive protruding AFM tip was employed for injecting current into single InGaN/GaN NWs with four various diameters as shown in the top magnified picture, the EL emission was collected using an optical micro-fiber coupled to a high-sensitivity spectrometer (Ocean Optics, QE Pro-FL) and detected by a back-thinned, TE-cooled CCD detector.

Shown in Figure 6–12(b) are the EL emission spectra of single InGaN/GaN NWs LED with diameters of $\sim$ 225, $\sim$ 330, $\sim$ 461, and $\sim$ 650 nm. The measured EL spectra exhibit peak emission wavelengths of 686, 625, 536, and 486 nm, and the corresponding full width at half maximum (FWHM) of each EL spectrum is 74, 32, 24 and 14 nm, respectively. The FWHM reduces with the increase of NW diameter, corresponding to a shorter emission wavelength. This is because the inhomogeneous In distribution (with enhanced In incorporation) increases with the reduced NW diameter. The spectra were taken at an injection current of approximately 7 μA. The four EL

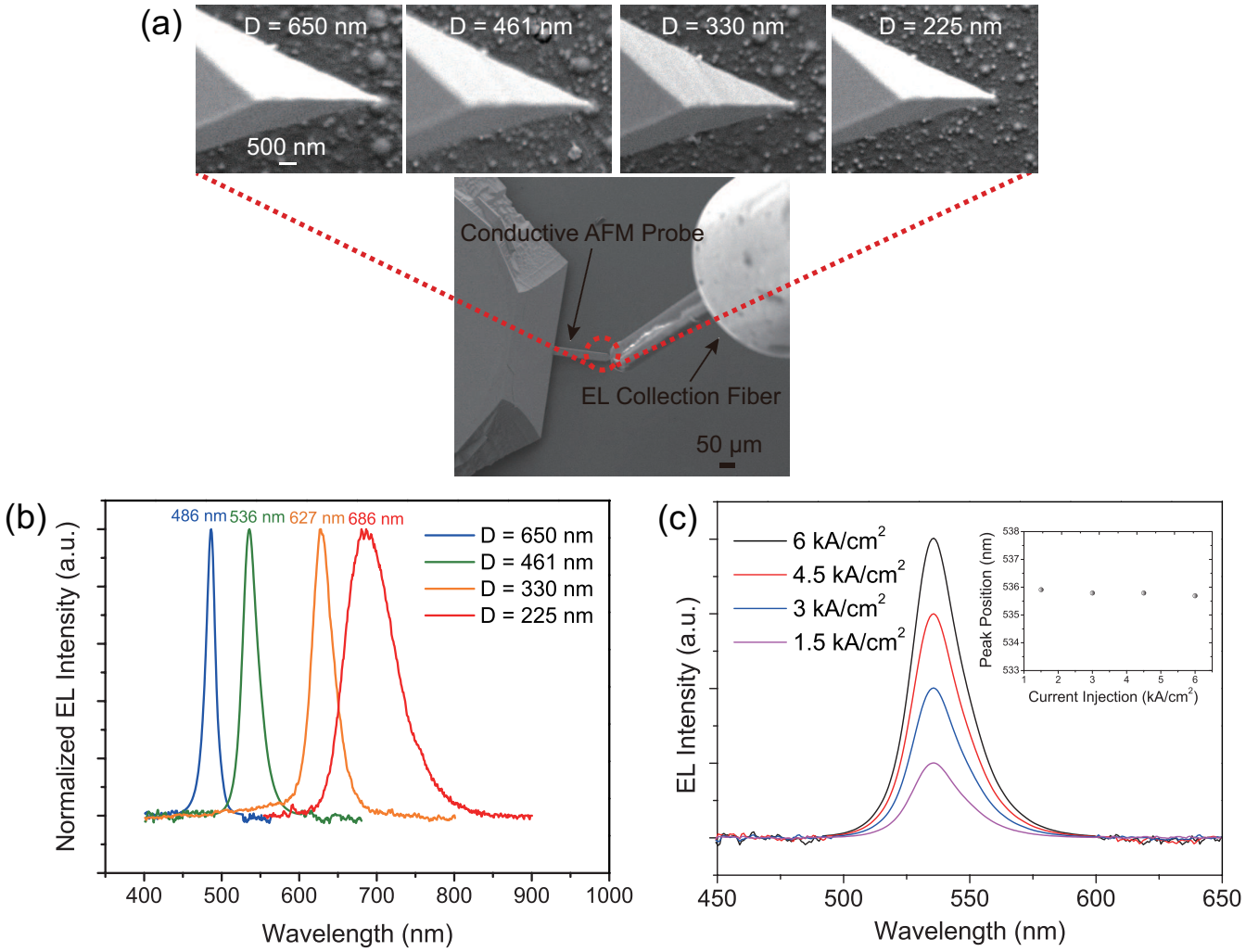

Figure 6–12: EL characterization of single InGaN/GaN NWs. (a) SEM picture of experimental setup. (b) EL emission spectra as a function of NWs diameter. (c) EL emission spectra as a function of injection current, for single NWs with D $\sim$ 461 nm.

emission spectrums have demonstrated the achievement of red (peak $\sim$ 686 nm), orange (peak $\sim$ 627 nm), green (peak $\sim$ 536 nm), and blue (peak $\sim$ 486 nm) single NWs LED on the same Si chip.

Figure 6–12(c) illustrates the EL emission spectra as a function of injection current for a representative single NWs with diameter of 461 nm, it is seen that the EL intensity increases near-linearly with varied injection current for different NW LEDs, and the inset of Figure 6–12(c) has indicated no significant shift in the EL emission peak position with increasing injection current, suggesting a small level of quantum-confined Stark-effect (QCSE), due to the highly efficient strain relaxation of nanowire structures [20].

6.5 Investigation of Mechanical Impact on EL Characterization of Single InGaN/GaN NWs

Using the nanomanipulation system, we have performed optical and electrical characterization of InGaN/GaN NWs. To demonstrate coupled-field nanomaterial characterization, we investigated the mechanical force impact on the EL properties of single InGaN/GaN NWs with various diameters, representing the first opto-electro-mechanical characterization of single semiconductor NWs. The EL spectra will be characterized for single InGaN/GaN NWs under different forces applied by the conductive protruding AFM tip.

6.5.1 Force Calibration on Single NWs

Single InGaN/GaN NWs with four different diameters were selected for the investigation. In order to apply different levels of force onto single InGaN/GaN NWs, prior to injecting current into single NWs and performing EL characterization, we firstly characterized the quantified force applied on single NWs using the developed force sensing method.

As shown in Figure 6–13, by controlling the nanomanipulator displacement input (there is implemented displacement encoder in nanopositioner with closed-loop control resolution of 1 nm) and calculating the AFM tip force, we derived the force-displacement input curves for single NWs with four various diameters of 645 nm, 470 nm, 325 nm, and 223 nm, respectively. From the results we can observe consistent relations between the applied displacement input and the sensed AFM tip force, which has verified that the uniformity of the developed mechanical characterization module for single NWs with varied dimensions. The derived calibration results will be used as look-up tables for applying quantified force to single InGaN/GaN NWs during EL characterization.

6.5.2 Force-dependent EL Characterization on Single InGaN/GaN NWs

To reveal the piezoelectric characteristics of single InGaN/GaN NWs with different Indium incorporation, four levels of force (0 N, 3 μN, 4 μN, 5 μN) were applied on single InGaN/GaN NWs according to the calibration results shown in Figure 6–13(b), and the EL signals were simultaneously measured by the detection optical micro-fiber. The force-dependent EL spectra of single InGaN/GaN NWs on the same Si substrate are summarized in Figure 6–14. Current of 7

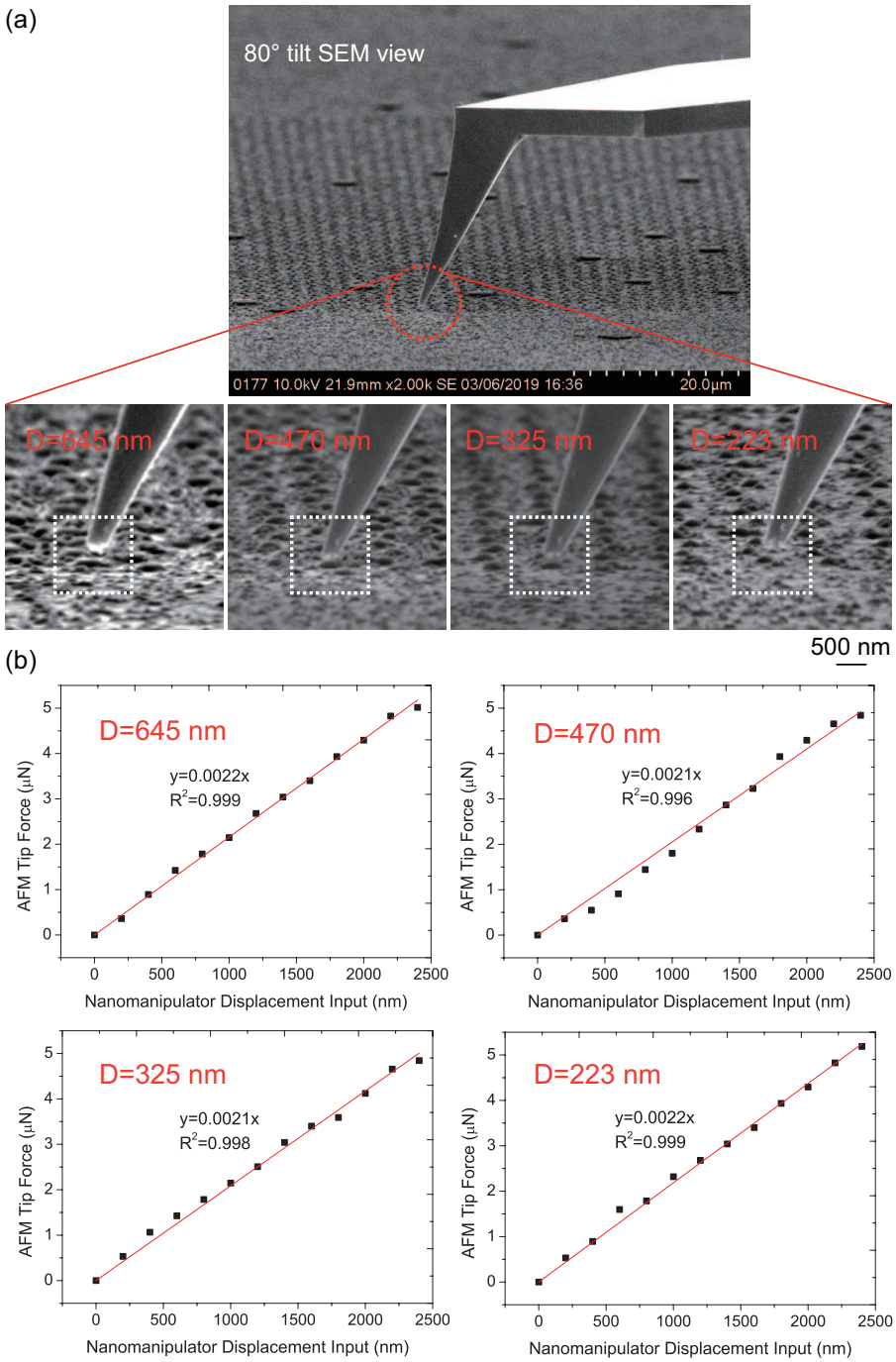

Figure 6–13: Force calibrations on single InGaN/GaN NWs with various diameters. (a) SEM picture of the force calibration experimental setup (80 ° tilt). (b) The force calibration results for single NWs with diameters of 645 nm, 470 nm, 325 nm and 223 nm.

μA was injected to single NW with the diameter of 645 nm, 470 nm, 325 nm respectively and

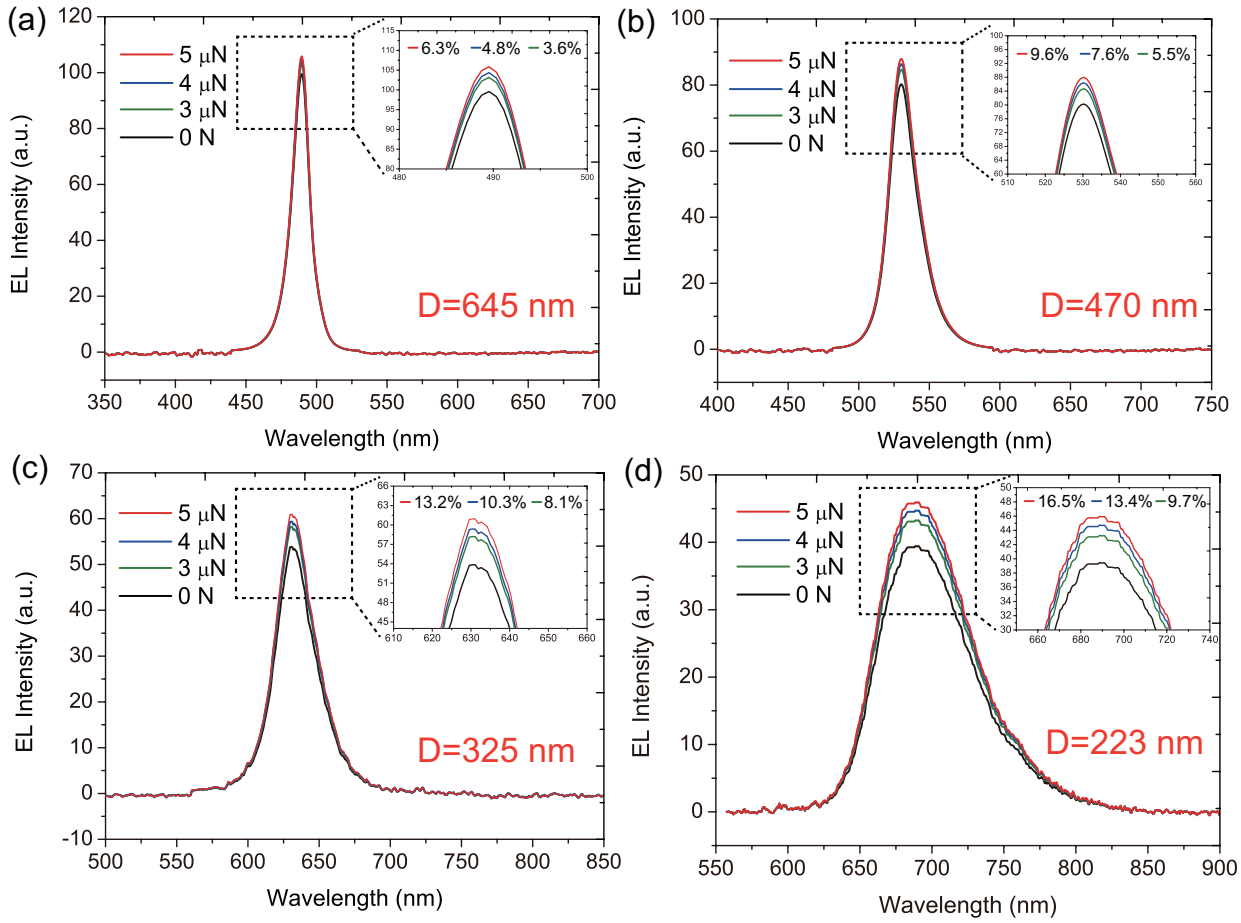

Figure 6–14: Force-dependent EL characterization on single InGaN/GaN NWs with various diameters. (a) D = 645 nm. (b) D = 470 nm. (c) D = 325 nm. (d) D = 325 nm. Inset: zoom-in view of the EL enhancement percentage.

4.2 μA injected to 223 nm NW. Those InGaN/GaN single NWs exhibit different InGaN composition corresponding to the EL emission peak at $\sim$ 490 nm, $\sim$ 530 nm, $\sim$ 630 nm and $\sim$ 689 nm, respectively.

InGaN-based planar LEDs and laser diodes (LDs) generally suffer from the quantum-confined Stark effect (QCSE) which can degrade the emission efficiency, especially in the deep-green, orange and red spectral ranges. To weaken the band tilt due to QCSE, there have been several approaches developed for InGaN/GaN planar structures with the emissions in the blue or green spectral range. However, there are very few reports on the experimental approaches for weakening QCSE for single InGaN/GaN NWs, which requires the high-resolution nanomanipulation for complex coupled-field

opto-electro-mechanical characterization. This work reports the achievement on improving the light output of full-color NW LEDs monolithically integrated on the same Si substrate by reducing the piezoelectric polarization Δ_{pz} in InGaN/GaN single NWs.

Induced from the applied nanoprobe force, external compressive stress was applied along the growth direction of Ga-polar single NWs to induce the external strains along c-direction and basal plane of the InGaN/GaN wurtzite crystal structure. Using the polarization-related constants reported by the literature [31, 32, 33], the reduction of piezoelectric polarization (Δ_{pz}) in this study is estimated to be 0.0058 C/m^2, 0.0078 C/m^2, 0.0118 C/m^2, and 0.0158 C/m^2 with 5 μN applied to the single NWs with diameter of 645 nm, 470 nm, 325 nm and 223 nm respectively. As piezoelectric polarization is the crucial parameter for the evaluation of QCSE, the reduction of piezoelectric polarization will facilitate the enhancement of EL peak intensity, and larger degree of EL peak intensity enhancement was thereby observed for single NWs with smaller diameters (with bigger piezoelectric polarization reduction), as shown in Figure 6–14.

For single NWs with a specific diameter, larger applied force (corresponding to larger external compressive stress) may induce larger external strain to the basal plane of the InGaN/GaN, as a result, as shown in the insets of Figure 6–14(a)(b)(c)(d), the EL peak intensity increases with the increasing applied force/external compressive stress to each single NWs, due to decreasing piezoelectric polarization.

Generally, for emitters fabricated by using InGaN/GaN planar structures, the QCSE in blue-emitting LEDs is much smaller or even negligible, compared to those with longer emission wavelength, such as green, orange and red-emitting LEDs. However, in this work, the QCSE is not negligible for the blue-emitting NW which exhibits the largest diameter ($\sim$ 645 nm) compared to the ones with green, orange and red emission colors.

6.6 Conclusion

This paper reported the development of the first SEM-based nanomanipulation system for opto-electro-mechanical characterization of 1D nanomaterials. Using this system, we have characterized and obtained superior optical (PL) and optoelectronic (EL) properties of single InGaN/GaN

NWs grown on Si substrates. Moveover, we have carried out the first investigation of the mechanical impact on the EL property of single InGaN/GaN NWs, and have observed EL peak intensity enhancements for all the single InGaN/GaN NWs emitting blue, green, orange and red lights. This study demonstrated a potential approach for reducing the QCSE of LED NWs by *in-situ* electrical nanoprobing in SEM, and illustrated a new method for improvement of NWs-based nanoelectronics and optoelectronics.

References

[1] S. Choi, H. Lee, R. Ghaffari, T. Hyeon, and D.-H. Kim, "Recent advances in flexible and stretchable bio-electronic devices integrated with nanomaterials," *Advanced Materials*, vol. 28, no. 22, pp. 4203–4218, 2016.

[2] M. Casini, *Smart buildings: Advanced materials and nanotechnology to improve energy-efficiency and environmental performance*. Woodhead Publishing, 2016.

[3] M. You, Z. Li, P. Zhang, D. Bai, M. Lin, and F. Xu, "Nanomaterial- and micromaterial-based immunoassays," in *Handbook of Immunoassay Technologies*, S. K. Vashist and J. H. Luong, Eds., Academic Press, 2018, pp. 273 –304.

[4] C. Li, J. B. Wright, S. Liu, P. Lu, J. J. Figiel, B. Leung, W. W. Chow, I. Brener, D. D. Koleske, T.-S. Luk, et al., "Nonpolar ingan/gan core–shell single nanowire lasers," *Nano letters*, vol. 17, no. 2, pp. 1049–1055, 2017.

[5] A. D. L. Bugallo, L. Rigutti, G. Jacopin, F. H. Julien, C. Durand, X. J. Chen, D. Salomon, J. Eymery, and M. Tchernycheva, "Single-wire photodetectors based on ingan/gan radial quantum wells in gan wires grown by catalyst-free metal-organic vapor phase epitaxy," *Applied Physics Letters*, vol. 98, no. 23, p. 233 107, 2011.

[6] W. Guo, M. Zhang, A. Banerjee, and P. Bhattacharya, "Catalyst-free ingan/gan nanowire light emitting diodes grown on (001) silicon by molecular beam epitaxy," *Nano Letters*, vol. 10, no. 9, pp. 3355–3359, 2010.

[7] L. J. Brillson, "Nanoscale luminescence spectroscopy of defects at buried interfaces and ultrathin films," *Journal of Vacuum Science & Technology B: Microelectronics and Nanometer Structures Processing, Measurement, and Phenomena*, vol. 19, no. 5, pp. 1762–1768, 2001.

[8] J. H. Choi, H. Y. Ahn, Y. S. Lee, K. Park, T.-H. Kim, K. S. Cho, C. W. Baik, S. I. Kim, H. Yoo, E. H. Lee, B. L. Choi, S.-D. Kim, Y.-W. Kim, M. Kim, and S. Hwang, "Gan light-emitting diodes on glass substrates with enhanced electroluminescence," *J. Mater. Chem.*, vol. 22, pp. 22 942–22 948, 2012.

[9] J. B. Baxter, F. Wu, and E. S. Aydil, "Growth mechanism and characterization of zinc oxide hexagonal columns," *Applied Physics Letters*, vol. 83, no. 18, pp. 3797–3799, 2003.

[10] C. Li, M. Gao, C. Ding, X. Zhang, L. Zhang, Q. Chen, and L.-M. Peng, "In situ comprehensive characterization of optoelectronic nanomaterials for device purposes," *Nanotechnology*, vol. 20, no. 17, p. 175 703, 2009.

[11] J. H. He, P. H. Chang, C. Y. Chen, and K. T. Tsai, "Electrical and optoelectronic characterization of a zno nanowire contacted by focused-ion-beam-deposited pt," *Nanotechnology*, vol. 20, no. 13, p. 135 701, 2009.

[12] B. G. Yacobi and D. B. Holt, "Cathodoluminescence scanning electron microscopy of semiconductors," *Journal of Applied Physics*, vol. 59, no. 4, R1–R24, 1986.

[13] A.Vila, F. F.Hernndez-Ramirez, J.Rodrguez, O. Casals, A.Romano-Rodrguez, J. Morante, and M. Abid, "Fabrication of metallic contacts to nanometre-sized materials using a focused ion beam (fib)," *Mater Sci Eng C*, vol. 26(5), no. 5, pp. 1063 –1066, 2006.

[14] G. D. Marzi, D. Iacopino, A. J. Quinn, and G. Redmond, "Probing intrinsic transport properties of single metal nanowires: direct-write contact formation using a focused ion beam," *J. Appl. Phys.*, vol. 96(6), no. 6, pp. 3458–3462, 2004.

[15] J. Qu, M. Lee, M. Hilke, and X. Liu, "Investigating the impact of sem chamber conditions and imaging parameters on contact resistance of in-situ nanoprobing," *Nanotechnology*, vol. 28(34), p. 345 702, 2017.

[16] R. S. Gates, "Experimental confirmation of the atomic force microscope cantilever stiffness tilt correction," *Review of Scientific Instruments*, vol. 88, no. 12, p. 123 710, 2017.

[17] S. A. Edwards, W. A. Ducker, and J. E. Sader, "Influence of atomic force microscope cantilever tilt and induced torque on force measurements," *Journal of Applied Physics*, vol. 103, no. 6, p. 064 513, 2008.

[18] K. Kishino, H. Sekiguchi, and A. Kikuchi, "Improved ti-mask selective-area growth (sag) by rf-plasma-assisted molecular beam epitaxy demonstrating extremely uniform gan nanocolumn arrays," *J. Cryst. Growth*, vol. 311(7), no. 7, pp. 2063 –2068, 2009.

[19] A. Bengoechea-Encabo, F. Barbagini, S. Fernandez-Garrido, J. Grandal, J. Ristic, M. Sanchez-Garcia, E. Calleja, U. Jahn, E. Luna, and A. Trampert, "Understanding the selective area growth of gan nanocolumns by mbe using ti nanomasks," *J. Cryst. Growth*, vol. 325(1), no. 1, pp. 89 –92, 2011.

[20] Y.-H. Ra, R. Wang, S. Y. Woo, M. Djavid, S. M. Sadaf, J. Lee, G. A. Botton, and Z. Mi, "Full-color single nanowire pixels for projection displays," *Nano Lett.*, vol. 16(7), no. 7, pp. 4608–4615, 2016.

[21] Z. Gong, S. Jin, Y. Chen, J. McKendry, D. Massoubre, I. M. Watson, E. Gu, and M. D. Dawson, "Size-dependent light output, spectral shift, and self-heating of 400 nm ingan light-emitting diodes," *Journal of Applied Physics*, vol. 107, no. 1, p. 013 103, 2010.

[22] R. Wang, X. Liu, I. Shih, and Z. Mi, "High efficiency, full-color alingan quaternary nanowire light emitting diodes with spontaneous core-shell structures on si," *Applied Physics Letters*, vol. 106, no. 26, p. 261 104, 2015.

[23] L. Lin, C.-H. Lai, Y. Hu, Y. Zhang, X. Wang, C. Xu, R. L. Snyder, L.-J. Chen, and Z. L. Wang, "High output nanogenerator based on assembly of GaN nanowires," *Nanotechnology*, vol. 22, no. 47, p. 475 401, 2011.

[24] F Limbach, C Hauswald, J Lhnemann, M Wlz, O Brandt, A Trampert, M Hanke, U Jahn, R Calarco, L Geelhaar, and H Riechert, "Current path in light emitting diodes based on nanowire ensembles," *Nanotechnology*, vol. 23, no. 46, p. 465 301, 2012.

[25] C. Zhao, T. K. Ng, A. Prabaswara, M. Conroy, S. Jahangir, T. Frost, J. O'Connell, J. D. Holmes, P. J. Parbrook, P. Bhattacharya, and B. S. Ooi, "An enhanced surface passivation effect in ingan/gan disk-in-nanowire light emitting diodes for mitigating shockleyreadhall recombination," *Nanoscale*, vol. 7, pp. 16 658–16 665, 2015.

[26] S. Wang, C. Sun, Y. Shao, Y. Wu, L. Zhang, and X. Hao, "Self-supporting gan nanowires/graphite paper: novel high-performance flexible supercapacitor electrodes," *Small*, vol. 13, no. 8, p. 1 603 330, 2017.

[27] Z. Fang, F. Donatini, B. Daudin, and J. Pernot, "Axial p–n junction and space charge limited current in single GaN nanowire," *Nanotechnology*, vol. 29, no. 1, 01LT01, 2017.

[28] D. van Treeck, J. Ledig, G. Scholz, Jonas, M. Musolino, A. Tahraoui, O. Brandt, A. Waag, H. Riechert, and L. Geelhaar, "Electroluminescence and current-voltage measurements of single-(in,ga)n/gan-nanowire light-emitting diodes in a nanowire ensemble," *Beilstein Journal of Nanotechnology*, vol. 10, pp. 1177–1187, 2019.

[29] M. Kibria, S Zhao, F. Chowdhury, Q Wang, H. Nguyen, M. Trudeau, H Guo, and Z Mi, "Tuning the surface fermi level on p-type gallium nitride nanowires for efficient overall water splitting," *Nature communications*, vol. 5, p. 3825, 2014.

[30] S Zhao, A. Connie, M. Dastjerdi, X. Kong, Q Wang, M Djavid, S Sadaf, X. Liu, I Shih, H Guo, et al., "Aluminum nitride nanowire light emitting diodes: breaking the fundamental bottleneck of deep ultraviolet light sources," *Scientific reports*, vol. 5, p. 8332, 2015.

[31] F. Bernardini, V. Fiorentini, and D. Vanderbilt, "Accurate calculation of polarization-related quantities in semiconductors," *Phys. Rev. B*, vol. 63, p. 193 201, 19 2001.

[32] H. Qin, X. Luan, C. Feng, D. Yang, and G. Zhang, "Mechanical, thermodynamic and electronic properties of wurtzite and zinc-blende gan crystals," *Materials*, vol. 10, no. 12, p. 1419, 2017.

[33] A. Polian, M. Grimsditch, and I. Grzegory, "Elastic constants of gallium nitride," *Journal of Applied Physics*, vol. 79, no. 6, pp. 3343–3344, 1996.

CHAPTER 7
Conclusion and Future Work

7.1 Summary of Accomplishments and Contributions

The multi-physical characterization of functional micro- and nanomaterials have significant impact on a variety of scientific and engineering problems from the perspective of both material synthesis and device application. Some MEMS-based and SEM-based platforms have been reported for mechanical and electrical characterization of micro- and nanomaterials, but given the limitations of one-axis actuation/sensing in MEMS-based platforms and few optical-related characterization platforms in SEM, the objectives of achieving dual-axis actuation/sensing in MEMS-based platforms and opto-electro-mechanical characterization in SEM have not been completed.

This thesis contributes to the field of multi-physical nanomaterial characterization by devoting efforts in four aspects. First of all, a MEMS-based microgripper that integrates two-axis actuators and force sensors for microscale elastic and viscoelastic characterization of soft materials in both compressive and shear directions was developed for the first time. Secondly, the contact resistance level during SEM *in-situ* electrical nanoprobing has been reduced significantly through a systematic investigation for the effect of SEM chamber conditions and imaging parameters on the contact resistance. Thirdly, superior electrical breakdown properties (the highest reported breakdown current density and breakdown power) of single n-i-n-n$^+$GaN NWs has been obtained through a systematic electrical characterization of single n-i-n-n$^+$GaN NWs using the developed SEM *in-situ* electrical nanoprobing system. Last but not least, the first-time developed multi-physical characterization system in SEM has enabled the first demonstration of opto-electro-mechanical characterization of single InGaN/GaN NWs, for better understanding its complex coupled-field properties.

The contributions of this thesis work are summarized as fellow.

- For the first time, two V-beam electrothermal actuators and two tri-plate differential capacitive sensors was integrated onto a MEMS-based microgripper, achieving on-chip microscale compressive and shear testing of soft materials simultaneously, with nanonewton force sensing resolution (compressive force resolution: 7.7 nN, and shear force resolution: 57.5 nN). The developed platform can facilitate various synthesis and/or characterization studies of microscale soft materials.
- Through the experimental investigation of the impact of SEM chamber conditions and imaging parameters on the contact resistance value using developed two-point nanoprobing system, the probe-sample contact resistance was significantly reduced from the mega-ohm level to the kilo-ohm level. The experimental results can serve as a guideline to evaluate electrical contacts of nanoprobing and instruct how to reduce the contact resistance in SEM-based, two-point nanoprobing.
- In the electrical characterization single n-i-n-n^+ GaN NW, benefiting from the flexibility of *in-situ* nanoprobing technique and the low NW-nanoprobe contact resistance, a breakdown current density of up to 4.65 MA/cm^2 and a breakdown power of up to 96.84 mW were achieved, both the highest among the previously reported breakdown parameters of single GaN NWs. The results can provide useful guidelines for experimentally improving the breakdown performance of single GaN NWs with precisely-controlled geometries on Si substrates, and thus enable applications of these GaN NWs in high-power nanoelectronics.
- An SEM-based multi-physical characterization system for characterizing the mechanical, electrical, optical, and multi-coupled-field properties of nanomaterials. To my best knowledge, this is the first SEM-based nanomanipulation system capable of opto-electro-mechanical characterization of nanomaterials. The system will greatly facilitate the reveal of complex underlying coupling-field properties of single nanomaterials and nanostructures, for potential device applications in nanoelectronics and optoelectronics.

- The first opto-electro-mechanical characterization have been performed for single InGaN/GaN NWs. Optical (photoluminescence) properties, optoelectronic (electroluminescence) properties, and opto-electro-mechanical properties (mechanical force impact on the EL property) have been characterized on single InGaN/GaN NWs respectively. The experimental results provided crucial insights for better understanding of the complex coupling-field properties of single LED NWs, and introduced a novel approach for reducing the QCSE of LED NWs by *in-situ* electrical nanoprobing in SEM.

7.2 Future Work

During the course of the presented research, existing challenging issues such as one-axis actuation/sensing for MEMS-baed mechanical characterization platforms and large electrical contact resistance during electrical characterization in SEM were improved, also new system for multi-physical characterization was developed. These efforts contribute to the multi-physical characterization of micro- and nanomaterials. Along the these direction, further investigations can be pursued to achieve more exiting results.

- The current MEMS microgripper was fabricated through the SOIMUMPs process, and the device has electrical connections among the two electrothermal actuators and the left active gripping arm. Although we have experimentally confirmed the negligible crosstalk between the two electrochemical actuators, their actuation leads to a nonzero electric potential on the left gripping arm. Therefore, a customized SOI microfabrication process can be further developed for electrical isolation between gripping arms and actuators.
- The *in-situ* electrical nanoprobing system still has room to improve. An automated nanoprobing system can be developed for single nanostructure electrical characterization, image processing technique can be employed for sensing the real-time position of the target tested object, and the nanoprobe connected with the nanopositioner can be moved to the target position. The automated nanoprobing may increase the testing efficiency of *in-situ* nanoprobing.

- As the force sensing end-effector in the developed mechanical characterization module in SEM, the protruding AFM tip can apply quantified force to the target object. However, due to the nature of cantilever-based AFM probe which owns relatively small beam stiffness, the applied force is usually limited to the micron-newton level. In the future, mechanical end-effectors with larger stiffness can be integrated into the multi-physical characterization system, for applying larger force onto nanostructures for investigation of coupled-field properties of nanomaterials in a wider range.